LASER COOLING, TRAPPING, AND RYDBERG SPECTROSCOPY OF NEUTRAL HOLMIUM ATOMS

by

James Allen Hostetter

A dissertation submitted in partial fulfillment of
the requirements for the degree of

Doctor of Philosophy

(Physics)

at the

UNIVERSITY OF WISCONSIN–MADISON

2016

Date of final oral examination: 5/5/2016

The dissertation is approved by the following members of the Final Oral Committee:

Mark Saffman, Professor, Physics
Thad Walker, Professor, Physics
James Lawler, Professor, Physics
Deniz Yavuz, Professor, Physics
John Wright, Professor, Chemistry

To my parents.

ACKNOWLEDGMENTS

The number of people I need to thank seems to diverge as $t \rightarrow$Ph.D. but I'll do my best to get everyone.

First and foremost, I would like to thank my adviser, Mark Saffman, for his support, patience, and mentoring over the years. He gave me an incredible project to work on that has challenged me to become a much better scientist than I was when I entered his lab.

I wouldn't be here without my parents and the support they have given me for my entire life. Together, they started me on my first steps towards science and showed me what having true passion for your field means. Thank you to them and the rest of my family for the love and reliability they have always shown me. You guys are the rock I know I can fall back on even when things seem entirely out of control.

Of course, I must acknowledge everyone past and present in the Saffman Lab. Every single one has uniquely contributed something that made me a better scientist. Jinlu Miao laid the entire foundation for this thesis and taught me all of the basics of AMO physics. Jon Pritchard and Larry Isenhower both taught me so, so much about the right way to do experimental physics and gave so much advice when my work was stalled. I'm extremely grateful to Donald Booth, Chris Yip, and Will Milner. I wish you the most success in continuing this work long after I'm gone. Josh Isaacs lightened the mood with his jams and was always a great source of conversation both scientific and not.

My teachers throughout my life have clearly all had a profound impact on my life, but there are three that I'd like to explicitly thank for putting me on the path towards my physics Ph.D. Mr. Landry, my seventh grade math teacher who convinced me that maybe I would like math better if I took notes or studied, helped me discover a love of math that laid the most basic foundation for my career in physics. I owe Mrs. Hodge, my high school physics teacher, for introducing me to formal physics and showing me how much better physics is than chemistry (even if she might disagree). Finally, I'd like to thank Dr. Mette Gaarde, my undergraduate thesis adviser. She not only taught me modern physics in as comprehensible a form as it comes, but she gave me real AMO work to cut my teeth on. I would not have ended up in this field without the opportunities and advice she gave me.

I can't name all of the friends that I've had in Madison that have commiserated with me and/or shown me that there is life outside of the lab but if you're reading this, this sentence is for you. Thank you in particular to a certain few for putting up with my thesis-fueled disappearing act for the last several months and still being the best on the few occasions when I braved the burn of the Daystar and actually left the library.

Lighthouse Photonics, your Sprout laser taught me so much about everything that can go wrong with lasers and was, in truth, the spark that made my write the first page of this thesis.

Oh, and I cannot forget to thank my cat Sampi, who is currently very vocally reminding me of his contributions over the last several years. Without him, I would not have nearly the visceral understanding of uncertainty, randomness, and cats-in-boxes that I do today, all of which are critical in the field of quantum information.

TABLE OF CONTENTS

Appendix

Page

APPENDICES

LIST OF TABLES

Appendix
Table Page

Appendix
Table

Appendix
Table Page

LIST OF FIGURES

Appendix
Figure Page

Appendix
Figure Page

Figure Page

Appendix
Figure

Abstract

Laser Cooling, Trapping, and Rydberg Spectroscopy of Neutral Holmium Atoms

James A. Hostetter

Under the supervision of Associate Professor Mark Saffman

At the University of Wisconsin - Madison

This thesis focuses on progress towards using ensembles of neutral holmium for use in quantum computing operations. We are particularly interested in using a switchable interaction between neutral atoms, the Rydberg blockade, to implement a universal set of quantum gates in a collective encoding scheme that presents many benefits over quantum computing schemes which rely on physically distinct qubits. We show that holmium is uniquely suited for operations in a collective encoding basis because it has 128 ground hyperfine states, the largest number of any stable, neutral atom. Holmium is a rare earth atom that is very poorly described for our purposes as it has never been cooled and trapped, its spectrum is largely unknown, and it presents several unique experimental challenges related to its complicated atomic structure and short wavelength transitions.

We demonstrate important progress towards overcoming these challenges. We produce the first laser cooling and trapping of holmium into a MOT. Because we use a broad cooling transition, our cooling technique does not require the use of a Zeeman slower. Using MOT depletion spectroscopy, we provide precise measurements of holmium's Rydberg states and its ionization potential. Our work continues towards cooling holmium into a dipole trap by calculating holmium's AC polarizability and demonstrating the results of early attempts at an optical dipole trap. We provide details of future upgrades to the experimental apparatus and discuss interesting potential for using holmium in quantum computing using single atoms in a magnetically trapped lattice. This thesis shows several promising indicators for continued work in this field.

Chapter 1

Introduction

1.1 Quantum Computing

Moore's Law predicts that every two years, the density of transistors on an integrated chip will double. As of 2016, the size of a transistor on such a chip is on the order of 10 nm. Within a few years, the size of these transistors will reach the molecular scale and Moore's law will be forced to slow or halt without a fundamental shift in computing technologies. Partially as an answer to this question, quantum computing has been proposed as a new computing paradigm with great potential for speed-ups for certain problems.

In a classical computer, the bits that make up its 0's and 1's are simply the open and closed states of a transistor. On the other hand, a quantum computer assigns these values to two-level quantum systems called qubits, denoted by $|0\rangle$ and $|1\rangle$. These qubits are quite a bit more powerful than classical bits. Whereas a classical bit can be either 0 or 1, a qubit can be some superposition of $|0\rangle$ and $|1\rangle$. This gives qubits an amplitude and a phase and allows us to encode exponentially more information on a single qubit than on a bit.

There is great potential in exploiting this dense information encoding. Quantum computers would provide ways to efficiently model complex quantum systems, speed up many classically hard calculations using algorithms like Shor's factoring algorithm or Grover's quantum search algorithm, and make possible many powerful techniques in information defense applications[4].

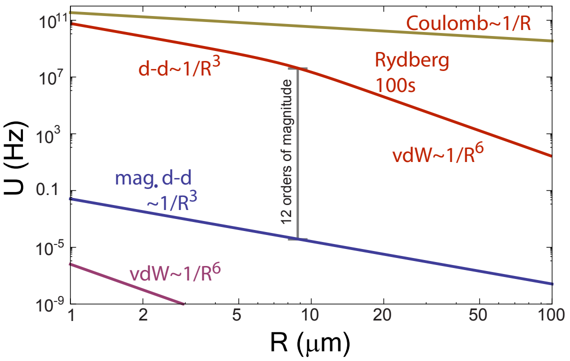

Figure 1.1 A comparison of interaction strengths in multiple scenarios. (Brown) The strong Coulomb 1/R interaction in ions. (Red) The dipole-dipole Rydberg interaction, 12 orders of magnitude greater than the dipole-dipole interaction of ground state atoms (blue). (Purple) The short-range van der Waals interaction. Reproduced from [2].

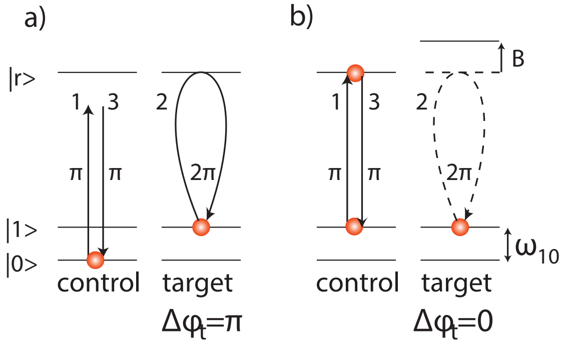

Figure 1.2 A two-qubit controlled Z (CZ) gate mediated by a Rydberg blockade. A resonant $|1\rangle \rightarrow |r\rangle$ π pulse is applied to the control qubit, followed by a 2π pulse on the target qubit. a) If the control qubit is in $|0\rangle$, the control does not excite to a Rydberg state and the target accumulates a π phase shift. b) If the control is in $|1\rangle$, the target is blockaded and accumulates no phase. Reproduced from [2].

In the last twenty years, much work has been done to find the most robust and scalable mediums with which to create a qubit. Because a qubit is by definition a quantum mechanical two-level system, many different implementations have been proposed. The most commonly noted candidates for large-scale quantum computing are photons[5], quantum dot spins[6], superconductors[7], ions[8], NV-centers[9], and neutral atoms[2]. As research progresses and the strengths and weakness of each implementation are uncovered, combinations of these are proposed to overcome the drawbacks of each individual type of qubit.

1.2 Quantum Computing with Single Neutral Atoms

The work in this thesis is aimed towards making progress in a collective neutral atom implementation. Neutral atoms are an interesting qubit candidate in part because they have a switchable interaction strength (Fig. 1.1) [2]. A ground state neutral atom has a very small, negligible Van der Waals interaction with the environment or other qubits. Quantum states $|0\rangle$ and $|1\rangle$ that are mapped onto the atom's ground hyperfine states possess long coherence times relative to gate times, a necessary trait in any qubit. When a large interaction strength is required for performing a two-qubit quantum gate, neutral atoms can be excited to a Rydberg state by a well-controlled laser pulse. The Rydberg state creates a large dipole potential and Stark shifts nearby atoms' energy levels. This shift prevents neighboring atoms from being excited by an identical laser pulse. This effect is called a *Rydberg blockade*. The entanglement that results in this case allows for the implementation of neutral atom quantum gates (Fig. 1.2)[10].

Previous work has used this effect to create fast phase gates at MHz rates[11], controlled-Z (CZ) gates and controlled-NOT (CNOT) gates[12, 13]. CNOT gates are a particularly important achievement because they are a universal quantum gate. These gates have been primarily performed mainly between single alkali atoms and notably there have been efforts to scale these results up by individually addressing qubits in single-atom arrays [14, 15]. These arrays select two magnetically insensitive $m_F = 0$ hyperfine ground states as their qubit bases. Neutral atoms are pumped into these states and loaded into a large, single-atom array. Qubit operations can then be carried out by applying precise, spatially addressed laser pulses to each qubit individually in its respective trap site. The number of qubits is only limited by the size and filling fraction of the single atom array. A K-qubit array using such a scheme is shown graphically in Fig. 1.3(a).

1.3 Quantum Computing with Neutral Atoms Ensembles

This work deviates from the single-atom array paradigm of neutral atom quantum computing. Instead of individually addressing neutral atoms, we aim to perform quantum operations on an ensemble of atoms. In this scheme, qubits are encoded across singly-occupied hyperfine states inside an ensemble instead of directly onto a specific atom. This is a significant departure from most schemes of quantum computing, which define their qubits on a physically distinct two-level system. There are two ways in which to do this kind of encoding. The first way is demonstrated in Fig. 1.3(b). We pick an atom with $K + 1$ hyperfine states. One hyperfine state is designated the "reservoir state" $|0\rangle$ and is typically easily optically pumped. The rest of the states are labeled as qubits $|1, ..., K\rangle$. If a qubit i has no population, it is defined to be in the state $|0_i\rangle$. Conversely,

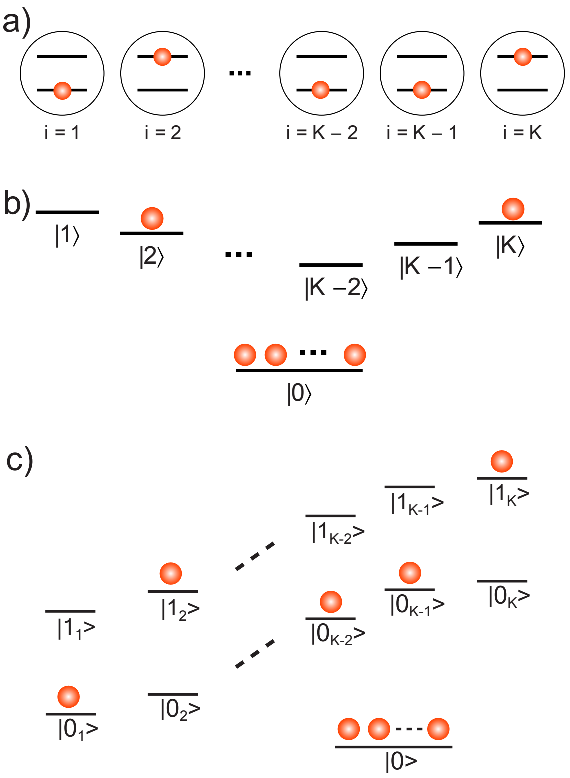

Figure 1.3 Three methods of encoding $|010...01\rangle$. a) In an array of single qubits. b) In an ensemble, maximizing the use of the ensemble's internal states. c) In an ensemble, pairing the internal states for greater stability. Reproduced from [2].

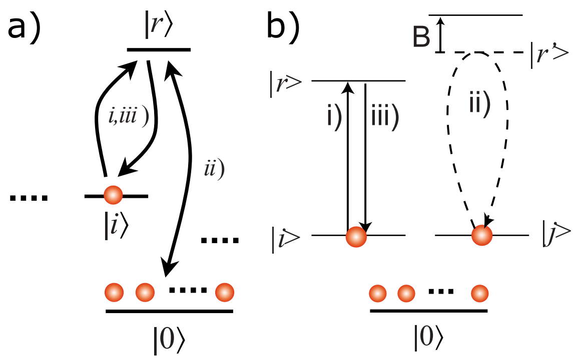

Figure 1.4 Single and two-qubit ensemble gates. a) A three-pulse gate rotates $|i\rangle$ between $|0_i\rangle$ and $|1_i\rangle$. b) A controlled phase gate performed in an ensemble, similar to that described in Fig. 1.2. Reproduced from [2].

if it has unity population it is defined to be in the state $|1_i\rangle$. In this manner, we create a quantum register with $K = (\sum_{F=F_{min}}^{F_{max}} 2F + 1) - 1$ qubits.

We can imagine initializing such a scheme by creating a cold ensemble of such an atom with a population $N \geq K$ and following the procedure outlined in Fig. 1.4(a). After pumping the ensemble into $|0\rangle$, we apply a Rydberg pulse to the ensemble. Because of the Rydberg blockade, only one atom in the ensemble is excited to the Rydberg state $|r\rangle$. A magnetic field is applied, breaking the degeneracy of the ground hyperfine states. We then apply a second pulse resonant between $|r\rangle$ and $|i\rangle$. This method is then repeated until the quantum register has been initialized to its desired state. Because the pulses act on the entire ensemble simultaneously, the register is a symmetric state representing a multiply-excited ensemble. To demonstrate this, consider an ensemble with $K = 3$ hyperfine states and $N = 4$ atoms in the ensemble. We will for this example label the logical register as $|\Psi\rangle_k$ and the wavefunctions of the physical qubits as $|\Psi\rangle_N$. We then write out examples of the states $|000\rangle_K$, $|100\rangle_K$, $|010\rangle_K$, $|001\rangle_K$, and $|101_K\rangle$.

$$|000\rangle_K = |0000\rangle_N \tag{1.1}$$

$$|100\rangle_K = \frac{1}{\sqrt{4}}(|1_1000\rangle_N + |01_100\rangle_N + |001_10\rangle_N + |0001_1\rangle_N) \tag{1.2}$$

$$|010\rangle_K = \frac{1}{\sqrt{4}}(|1_2000\rangle_N + |01_200\rangle_N + |001_20\rangle_N + |0001_2\rangle_N) \tag{1.3}$$

$$|001\rangle_K = \frac{1}{\sqrt{4}}(|1_3000\rangle_N + |01_300\rangle_N + |001_30\rangle_N + |0001_3\rangle_N) \tag{1.4}$$

$$\begin{aligned} |101\rangle_K = \frac{1}{\sqrt{12}}(&|1_11_300\rangle_N + |1_101_30\rangle_N + |1_1001_3\rangle_N + |1_31_100\rangle_N + |01_11_30\rangle_N \\ &+ |01_101_3\rangle_N + |1_301_10\rangle_N + |01_31_10\rangle_N + |001_11_3\rangle_N + |1_3001_1\rangle_N + |01_301_1\rangle_N + |001_31_1\rangle_N) \end{aligned} \tag{1.5}$$

The states can be read out by cycling an atom to a read-out state. Fluorescence of $|1_i\rangle$ (or lack thereof in the case of $|0_i\rangle$) constitutes a measurement of that W-state.

One major drawback of this scheme is that it is not robust against atom loss errors. If the atom in state $|1_i\rangle$ is lost, the W-state is read as $|0_i\rangle$ instead of an error and is thus difficult to correct. One way to protect our register from such an error is to use the scheme demonstrated in Fig. 1.3(c). We imagine an ensemble of $N \geq K$ atoms with $2K$+1 hyperfine states. We again create a reservoir state $|0\rangle$. In this scheme, we pair up our hyperfine states. Each state represents one half of a qubit $|0_i\rangle$ or $|1_i\rangle$ and its partner represents its complement. In a manner similar to the previous scheme, we can populate the qubits one at a time to initialize the state. Also as with the previous method no qubit should have larger than unity population, but unlike the previous method each qubit should always have exactly unity population. This scheme generates a substantially more complicated logical state vector because every qubit must be initialized, whereas in the previous method only $|1_i\rangle$ was initialized. For simplicity, we will provide an example of an ensemble with only $K = 2$ hyperfine states and $N = 3$ atoms in the ensemble, following the same conventions as before.

$$|00\rangle_K = \frac{1}{\sqrt{6}}(|0_1 0_2 0\rangle_N + |0_1 0 0_2\rangle_N + |0 0_1 0_2\rangle_N + |0_2 0_1 0\rangle_N + |0 0_2 0_1\rangle_N + |0_2 0 0_1\rangle_N) \tag{1.6}$$

$$|01\rangle_K = \frac{1}{\sqrt{6}}(|0_1 1_2 0\rangle_N + |0_1 0 1_2\rangle_N + |0 0_1 1_2\rangle_N + |1_2 0_1 0\rangle_N + |0 1_2 0_1\rangle_N + |1_2 0 0_1\rangle_N) \tag{1.7}$$

$$|10\rangle_K = \frac{1}{\sqrt{6}}(|1_1 0_2 0\rangle_N + |1_1 0 0_2\rangle_N + |0 1_1 0_2\rangle_N + |0_2 1_1 0\rangle_N + |0 0_2 1_1\rangle_N + |0_2 0 1_1\rangle_N) \tag{1.8}$$

$$|11\rangle_K = \frac{1}{\sqrt{6}}(|1_1 1_2 0\rangle_N + |1_1 0 1_2\rangle_N + |0 1_1 1_2\rangle_N + |1_2 1_1 0\rangle_N + |0 1_2 1_1\rangle_N + |1_2 0 1_1\rangle_N) \tag{1.9}$$

This scheme is more robust against error; because each pair allows one and only one atom it is theoretically a simple matter to distinguish between a valid qubit and an error due to incorrect qubit population. We produce a quantum register substantially smaller than the one shown in Fig. 1.3(b) with only $K = (\sum_{F=F_{min}}^{F_{max}} \frac{2F+1}{2}) - 1$ in the optimal case.

Gates in collective quantum computing are performed in a slightly different manner to those performed with single atoms (Fig. 1.4). For the maximal qubit method shown in Fig. 1.3(b), single qubit rotations must be performed via a 3-pulse technique through a Rydberg state rather than by a Raman process. A resonant pulse transfers some fraction of qubit $|i\rangle$'s wavefunction to the Rydberg state. While in this state, all other atoms in the ensemble are blockaded. A second pulse couples the reservoir state to the Rydberg state. A third pulse returns any population in the Rydberg state to $|i\rangle$. $|i\rangle$ has then been rotated. Two-qubit gates and single-qubit gates in the paired qubit scheme are performed very similarly to those for single-atom gates.

The initialization of both techniques and the implementation of their gates requires the ability to blockade all atoms in an ensemble. This has been recently demonstrated along with single qubit rotations into a W-state[16].

1.4 Advantages and Disadvantages of Ensemble Quantum Computing

1.4.1 Advantages of Ensemble Quantum Computing

Quantum computing with mesoscopic ensembles possesses several advantages over techniques that rely on manipulation of physically distinct single qubits. When the idea was first proposed with neutral atoms, it was noted that creating an optical trap containing a large number of atoms is experimentally much easier than creating a similar trap for a single atom[17]. This only becomes a stronger argument when discussing arrays of ensembles, which can be used individually as qubits themselves or as part of a larger conglomeration of multi-qubit, internally encoded ensembles. In the case of using internally encoded ensembles, one ensemble can contain a number of qubits equal to one less than the number of hyperfine levels in the ground state of its constituent atoms. For example, holmium has the largest number of ground hyperfine states of any stable atom with 128. An ensemble of such an atom could theoretically create a 127-qubit quantum register. A comparable single-atom array is very difficult to achieve and compares even more poorly if an array of ensembles is proposed. By using the Rydberg blockade to entangle arrays of internally encoded ensembles, it has been estimated that a 1000-qubit quantum computer could be achievable[18]. Scalability therefore appears easier to achieve with ensembles assuming that the basic units of the array can be built.

Ensembles also allow multiple qubits to be addressed by tuning the frequency of the lasers used for qubit rotation rather than by spatially addressing individual single atom traps, which is by itself a technical difficulty. Complex experimental structures with devices such as microelectromechanical systems (MEMS) or with acousto-optic modulators (AOMs) are needed to achieve such spatial addressing[19]. Both of these solutions are not only expensive, but they can be difficult to implement with uniform efficiency across a large array. The challenge also increases if the filling fraction of the array is low, randomizing the experiment-to-experiment position of addressable qubits. With the ensemble method, the entire register is addressed at the same time and does not depend strongly on the storage of individual atoms, in principle allowing for consistent use of the entire set of qubits and ensuring their presence in the register.

There are further benefits in single-qubit rotations. In a single-atom array, rotations on a single-qubit are done with Raman processes. Because all of the qubits are prepared in the same set of hyperfine states, focusing of the Raman beams is a trade-off between a tight focus (to reduce crosstalk between qubits) and a loose focus (to allow for the beams to be more easily aligned). Crosstalk in particular has proven to be a significant barrier in such implementations[20]. The same rotation done in an ensemble basis must instead utilize the Rydberg blockade (Fig. 1.4(a)).

A laser resonant with $|1_i\rangle \rightarrow |r\rangle$ is applied, rotating any atoms in $|1_i\rangle$ to the Rydberg state and blockading its neighbors. A second pulse couples $|r\rangle \rightarrow |0\rangle$, transferring population between the two states. Any remaining fraction of the wavefunction in $|r\rangle$ is rotated back to $|1_i\rangle$ by a third pulse. Because only one atom is allowed in the Rydberg state at a time and all of the qubits are assigned to different hyperfine levels, the crosstalk problem is greatly reduced. In addition, the ensemble Rabi frequency Ω_N of a transition from $|\bar{g}_N\rangle$ to $|\bar{r}_N\rangle$ such that

$$|\bar{g}_N\rangle = |g_1 g_2 ... g_N\rangle \tag{1.10}$$

$$|\bar{r}_N\rangle = \frac{1}{\sqrt{N}}(|r_1 g_2 g_3 ... g_N\rangle + |g_1 r_2 g_3 ... g_N\rangle + ... + |g_1 g_2 g_3 ... r_N\rangle) = \frac{1}{\sqrt{N}} \sum_{i=1}^{N} |r_i\rangle \tag{1.11}$$

is proportional to the dipole matrix element.

$$\Omega_N \propto \langle \bar{r}_N | \mathbf{r} | \bar{g}_N \rangle = \frac{1}{\sqrt{N}} \sum_{i=1}^{N} \langle r_i | \mathbf{r} | \bar{g}_N \rangle = \frac{1}{\sqrt{N}} (N \times \langle r | \mathbf{r} | g \rangle) = \sqrt{N} \langle r | \mathbf{r} | g \rangle \tag{1.12}$$

Therefore, ensemble encoding can provide much stronger coupling to the qubits in the case of single-atom rotations. We note that this advantage disappears in the case of two-qubit gates such as in 1.3a. The $\sqrt{N}$ enhancement exists because of the large number of atoms in $|0\rangle$ available for the transition. Because there is only one atom in the each register state, there is no similar enhancement.

Further benefits in error correction are derived from the indistinguishability of the atoms in the trap. Because of this indistinguishability, every atom in the ensemble participates in each computation. The error rate thus scales favorably because the quantum information is distributed among many atoms. This form of entanglement has been shown to be maximally insensitive towards atom loss[21]. As an example, let us consider an example single qubit encoded to be $|0\rangle$ on an ensemble of N atoms.

$$|0_N\rangle = \frac{1}{\sqrt{N}}(|0_1 g_2 g_3 ... g_N\rangle + |g_1 0_2 g_3 ... g_N\rangle + ... + |g_1 g_2 g_3 ... 0_N\rangle \tag{1.13}$$

We can easily rewrite this to emphasize a single atom in the ensemble. For simplicity, we will do this to the first atom in the ensemble. This is an arbitrary distinction because the state is symmetric and we can relabel it how we like.

$$|0_N\rangle = \frac{1}{\sqrt{N}}(|0\rangle \otimes |\bar{g}_{N-1}\rangle + \sqrt{\frac{N-1}{N}}(|g\rangle \otimes |0_{N-1}\rangle) \qquad (1.14)$$

If this first atom is lost, the wave function reduces to

$$|0_N\rangle = \frac{1}{\sqrt{N}}\,|\bar{g}_{N-1}\rangle + \sqrt{\frac{N-1}{N}}\,|0_{N-1}\rangle \qquad (1.15)$$

At large N, this function is dominated by the second term and is exactly the correct state with one fewer atom. The error caused by any individual atom loss is therefore characterized by the first term. This is the same error for any K-qubit state and we can therefore see that the error from loss of a single particle scales as K/N. This error can be accepted or, if the particle loss is detected and the erroneous qubit states discovered, the error can be corrected by applying error correction algorithms discussed in [22]. For $N \gg K$, we see a very favorable comparison of error rates due to single-atom loss compared to a lattice of single atoms, where the loss of any one atom is catastrophic and must be corrected.

1.4.2 Disadvantages of ensemble quantum computing

There are, however, many challenges associated with this scheme of quantum computing. Because ensemble encoding collectively and symmetrically addresses all atoms in an ensemble, systematic errors are likely to affect all qubits in the ensemble instead of potentially only affecting a few physically isolated qubits. There is also the possibility of multiple excitations causing meaningless populations to appear in a qubit. In the pair-wise qubit scheme, this can be dealt with by monitoring the qubit populations to ensure unity population and applying corrective measures if an error occurs. A corrective measure would feature emptying a qubit (unless the error is already that there are no atoms in the qubit) and resetting it with atoms from the reservoir. This of course destroys the information encoded, but if redundant qubits are employed this information can be recovered by placing the replacement qubit in the $|1_i\rangle$ state and performing a CNOT gate using the redundant qubit as the control and the replacement qubit as the target.

Another concern is collisional losses within the ensemble. These losses can lead to large decoherences in the ensemble. Of highest concern is hyperfine changing collisions, which can lead to rapid atom/information loss by emitting a photon of energy equal to the hyperfine splitting of the atom[18]. This is typically several GHz, which is one or two orders of magnitude greater than the potential of most ODTs. Collisions can also cause changes of $\Delta m_F = \pm 1$[23], which are not energetically large enough to cause trap losses (in the absence of a magnetic field, these states are degenerate and changes do not induce any heating) but they can lead to logical errors in qubit states for two qubits simultaneously. Therefore, it would be necessary to superimpose an optical lattice with a very short period. Individual atoms would then be confined to their own individual lattice site, suppressing collisions. Given reasonable trap and lattice site densities, the occupation fraction of single atoms in the lattice should be approximately 40% [18].

Noise in local magnetic fields are also a problem in ensemble encoding. The interaction energy between hyperfine levels and external magnetic fields is given by

$$-\overrightarrow{\boldsymbol{\mu}} \cdot \overrightarrow{\mathbf{B}} = \mu_B g_F m_F |B|. \tag{1.16}$$

Arrays of single-atom traps use the magnetically-insensitive $m_F = 0$ states for their quantum logic. Ensemble encoding does not have this option as it requires the use of many different hyperfine states that are much more sensitive to fluctuations in magnetic fields. To address each qubit, an additional bias field must be applied to lift the degeneracy of the hyperfine levels. When a field is applied to interact with a qubit, it also Zeeman shifts every other qubit in the ensemble and induces dephasing. In holmium, there is a large range of g_F factors in the hyperfine manifold (Fig. 1.5). While it only requires a modest field to split the $F = 4$ levels, it requires a field 2.5 times as large to split the $F = 11$ levels. Using the $F = 11$ qubits is therefore very disturbing to the $F = 4$ qubits. Applied magnetic fields will have to be both fast and low-noise, which can be a difficult combination to achieve.

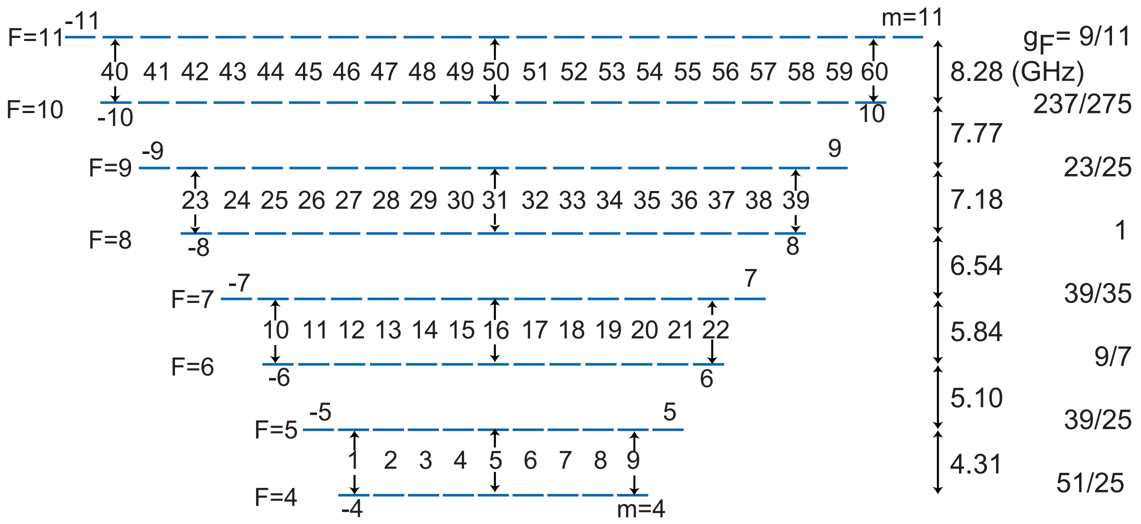

Figure 1.5 A diagram of holmium's 128 ground $4f^{11}6s^2$ hyperfine states showing the energy spacing between adjacent hyperfine levels. This demonstrates a possible encoding scheme using the method described in Fig. 1.3(c) to define 60 qubits for one ensemble. Reproduced from [2].

1.5 Holmium and the Rare Earths

We propose to implement this ensemble scheme with the element holmium. Holmium is an atom in the rare earth family. Rare earths are recognized for having a closed $6s$ subshell usually shielding a lower energy $4d$ or $4f$ subshell. This electronic configuration is strongly non-hydrogenic and thus rare earths usually have very complex level structures. Holmium's extreme properties in particular are desirable when building an ensemble-based quantum register. In the ensemble scheme, it is clear that a large hyperfine manifold is beneficial as it provides a larger number of qubits. $^{165}\mathrm{Ho}_{67}$ possesses a large nuclear angular momentum $I = 7/2$ and a large electronic angular momentum $J = 15/2$, producing a ground state hyperfine manifold $F = 4...11$ with 128 hyperfine states, the most of any stable ground state atom (Fig. 1.5). With this number of hyperfine states we can potentially create a quantum register with 127 qubits using the maximal-encoding scheme shown in Fig. 1.3(b) or 63 qubits using the pair-wise scheme shown in Fig. 1.3(c). In addition, holmium's single isotope, large magnetic moment, large cooling linewidth, and excited state hyperfine splittings create favorable conditions for single-atom arrays in magnetic traps and for single-atom imaging in general (Table 1.1). These applications are discussed in detail in chapter 7.

Element Name	Isotopes	Ground State	I	J	F	HF States
Dysprosium	$^{156}_{66}$Dy	$4f^{10}6s^2$	0	8	8	17
	$^{158}_{66}$Dy					
	$^{160}_{66}$Dy					
	$^{162}_{66}$Dy					
	$^{164}_{66}$Dy					
	$^{161}_{66}$Dy		5/2		11/2-21/2	102
	$^{163}_{66}$Dy		5/2		11/2-21/2	102
Holmium	$^{165}_{67}$Ho	$4f^{11}6s^2$	7/2	15/2	4-11	128
Erbium	$^{162}_{68}$Er	$4f^{12}6s^2$	0	6	6	13
	$^{164}_{68}$Er					
	$^{166}_{68}$Er					
	$^{168}_{68}$Er					
	$^{170}_{68}$Er					
	$^{167}_{68}$Er		7/2		5/2-19/2	104
Thulium	$^{169}_{69}$Tm	$4f^{13}6s^2$	1/2	7/2	3-4	16
Ytterbium	$^{168}_{70}$Yb	$4f^{14}6s^2$	0	0	0	1
	$^{170}_{70}$Yb					
	$^{172}_{70}$Yb					
	$^{174}_{70}$Yb					
	$^{176}_{70}$Yb					
	$^{171}_{70}$Yb		1/2		1/2	2
	$^{173}_{70}$Yb		5/2		5/2	6

Table 1.1 A comparison of the hyperfine manifolds of the rare earths that have been trapped in a MOT. Holmium possesses the largest manifold.

Because their structure precludes the existence of a strong, entirely closed transition on which to cycle cooling photons, laser cooling and trapping of these atoms was achieved long after the first MOTs were made with alkali atoms [24], starting with the trapping of ytterbium [25]. Since then, MOTs have been achieved in erbium[26], dysprosium[27], thulium[28], and holmium[29]. These have mostly been cooled with a broad, blue transition(Table 1.2). Despite the fact that these transitions are technically open and therefore ”leaky”, it has been found that they are very nearly entirely closed. This can be exploited to allow laser cooling with or without repumpers. In addition to the negligible slow leak, these successes have been attributed to the large magnetic moments of the rare earths contributing to the trap lifetime through interactions with a large magnetic quadrupole field. Rare earths also include the most magnetic elements of the periodic table. Dy and Ho are the most magnetic elements with magnetic moments of $10.65\mu_B$ and $10.6\mu_B$ respectively. Er and Tm have magnetic moments of $7\mu_B$ and $4\mu_B$ respectively. The achievement of creating MOTs with rare earths has provided a stepping stone to the recent achievement of creating a molecular MOT with an even more complicated structure. [30, 31].

The broad lines used limit the achievable MOT temperatures. Doppler temperatures are much higher than the temperatures that are regularly achieved in alkalis (Table 1.2), although it has been shown that sub-Doppler cooling can cool the rare earth atoms into the 10’s of μK[27, 29, 32]. It is important for our quantum computing goals to consistently achieve these sub-Doppler temperatures because higher temperatures prevent the loading of large ensembles in an ODT and enhance the dipolar collision rates, leading to hyperfine changing collisions and trap/information loss. Recently, there have been successes in creating rare earth MOTs with entirely closed, narrow line cooling transitions (Table 1.3). MOT temperatures have been achieved that are in the range of single μK and BECs have been made that are nK [33].

Others have used the extremely magnetic properties to create nK MOTs, as is the case in [38]. A common problem in extremely narrow-line MOTs is that the radiation pressure cannot compete with gravitational and magnetic forces. This limitation was circumvented by using beams that were blue-detuned from a narrow-line transition to create a MOT at a non-zero magnitude point of the quadrupole magnetic field. The magnetic trapping provides a counter-force to gravity and also

Element	Cooling Line	λ (nm)	$\frac{A}{2\pi}$ (MHz)	$\mathrm{T_D}(\mu\mathrm{K})$	$\Delta E_{F\vert e\rangle}$ (GHz)	Δ K(cm^{-1})
^{85}Rb	$5s_{1/2} \to 5p_{3/2}$	780	6.1	146	0.12[34]	8050
^{87}Rb	$5s_{1/2} \to 5p_{3/2}$	780	6.1	146	0.27[35]	8050
Cs	$6s_{1/2} \to 6p_{1/2}$	895	4.6	118	1.2[36]	9060
^{161}Dy	$4f^{10}6s^2 \to 4f^{10}6s6p$	421	31.9	765	0.33[27]	394
Ho	$4f^{11}6s^2 \to 4f^{11}6s6p$	410	32.5	780	7.67 [29]	-155
^{167}Er	$4f^{12}6s^2 \to 4f^{12}6s6p(^1P_1)$	401	35.6	854	2.04 [32]	-613
Tm	$4f^{13}6s^2 \to 4f^{13}6s6p$	411	10	240	1.86 [28]	1218
^{173}Yb	$6s^2 \to 6s6p$	399	28	672	0.21[37]	413

Table 1.2 A list of typical, broad cooling lines in the rare earths and their corresponding Doppler temperatures. Column 6 includes the hyperfine splittings of cycling transitions of the excited states that are used for cooling. Column 7 indicates the energy mismatch between the cooling photon and a second, ionizing photon to give some idea of the Doppler broadening of a two-photon transition to a Rydberg state. Frequently trapped alkalis are included for comparison.

Element	Excited State	λ (nm)	$\frac{A}{2\pi}$ (MHz)	$\mathrm{T_D}(\mu\mathrm{K})$	$\Delta E_{F\vert e\rangle}$ (GHz)	ΔK(cm^{-1})	Dem.
^{161}Dy	$4f^9 5d6s^2$	741	0.0018	0.04	0.278,0.314 [38]	20909	✓[33]
Ho	$4f^{10}5d_{5/2}6s^2$	608	0.038	0.91	9.2 [39]	15671	
Ho	$4f^{11}6s6p(^3P_1)$	599	0.15	3.5	11.7 [39]	15177	
Ho	$4f^{11}6s6p(^3P_2)$	426	1.59	38	13.5 [40]	1618	
Ho	$4f^{10}5d^2 6s$	412	2.3	780	?? [41]	22	
^{167}Er	$4f^{12}6s6p(^3P_1)$	583	0.19	4.5	3.25 [32]	14957	✓[42]
Tm	$4f^{12}5d_{3/2}6s^2$	531	0.35	8.4	1.9 [43]	15574	✓[43]
^{173}Yb	$6s6p(^3P_1)$	556	0.182	4.4	4.7[44, 45]	14472	✓[44]

Table 1.3 A list of narrow cooling lines in the rare earths and their corresponding Doppler temperatures. Column 6 includes the hyperfine splittings of cycling transitions of the excited states that are used for cooling. Column 7 indicates the energy mismatch between the cooling photon and a second, ionizing photon to give some idea of the Doppler broadening of a two-photon transition to a Rydberg state. Column 8 indicates whether a MOT with these lines has been experimentally demonstrated.

Zeeman-shifts the hyperfine levels to the point that the blue-detuned MOT beams are energetically lower than the shifted cooling transitions[46].

These rare earth MOTs open up several avenues of interesting research. They have been used to study fundamental properties of collisions in cold gases, searches for EDM [47], suitability for quantum memory, searching for fine-structure constant variation[28], long-range anisotropic dipole-dipole interactions that can induce phases beyond those described by the nearest-neighbor Hubbard model[27], orbital effects in cold-atom collisions, BECs with dipolar gases[26], and deterministic single-atom generation[48].

Despite the experimental gains made in the last 15 years, a quantum register encoded on a large ensemble still poses several challenges. A major barrier is the unexplored nature of holmium. Many transitions from the ground state are still unknown, though they are probably weak. Couplings between excited states are almost entirely unmeasured; the excited state of our cooling light $4f^{11}6s6p$ has only one known transition (back to the ground state) and in section 4.2.5 we discuss the measurement of a previously unknown line that acts as a repumper for our MOT that was discovered serendipitously. Both the Rydberg spectrum and the related C_6 dipole-dipole interaction coefficient were also poorly known before this work and they are both critical to our gate operations. While we have produced the first holmium MOT, no long-lived optical trapping has been performed on holmium before. There is therefore a vast experimental space to explore before a register can be initialized and gate operations can proceed. In this thesis, we present the results of several experiments and calculations to progress us towards that goal.

Chapter 2 provides a detailed discussion of the experimental setup developed and built for these experiments. It includes layouts and measurements of our laser and vacuum systems.

Chapter 3 describes the creation of the Ho MOT. It provides experimental parameters on several MOTs that we have made, calculations on the feasibility of MOTs cooling on lines that require large repumper powers, and discussions of narrow-line MOTs.

Chapter 4 contains the results of an experiment that performed Rydberg spectroscopy via MOT depletion in holmium. This work resulted in a large database of previously unmeasured Rydberg states, an improved measurement of the ionization potential of holmium, and a previously unknown MOT repumping transition.

Chapter 5 discusses progress towards the first Ho optical dipole trap. It contains information on the theoretical basis of the ODT, experimental setup, measurements and discussion of the lifetime of the trap, and several proposals to extend that lifetime.

Chapter 6 presents the design of an upgrade to the experimental system. This upgrade should increase the flux of holmium atoms, improve vacuum pressure, improve the functioning of the magnetic gradient field, and allow for optical dipole trap transport of holmium atoms into a glass cell without any moving parts

Chapter 7 includes exploration of the relevance of this work to other fields. These fields consist of single-atom imaging using rare earths, magic magnetic fields for single qubits, and blackbody radiation calculations.

Chapter 8 concludes the work. It discusses the current status of the project. We also briefly discuss possible future directions for our research.

Chapter 2

Experimental Setup

2.1 Vacuum System

2.1.1 Holmium Source

In order to conduct our experiments, we need a source of gaseous holmium to cool. Rare earths have a very low vapor pressure compared to alkali atoms, so the only method by which to produce this gas is to prepare an atomic beam in an oven. The vapor pressure for holmium is estimated using the Clausius-Clapeyron equation

$$\log P = -\frac{A}{T} + C \tag{2.1}$$

where the coefficients for holmium are $A = -1.5137 \times 10^4$ K and $C = 8.426$[49]. At room temperature, these numbers give a vapor pressure of $\sim 10^{-42}$ Torr at room temperature for holmium, compared to $\sim 10^{-6}$ Torr for cesium. These were found with a least-squares fit to high temperature data ($>$1000 K) and are most likely misleading at low temperature, but they are reliable at the high temperatures the oven operates in. In conjunction with the numerous other rare earth experiments operating in UHV environments, they also suggest the UHV compatibility of Ho. In addition, it predicts that in the low UHV regime ($\sim 10^{-7} - 10^{-8}$ T) the holmium should begin to vaporize around 900-1000 K, in agreement with qualitative observations.

Our effusion cell is a Createc CU-3504-S1-DC-12A. It consists of a tantalum crucible heated with a tantalum wire. The crucible is surrounded by a jacket that is externally water cooled to 15 °C to insulate the rest of the experiment from the high temperatures the effusion cell is capable of (1400 °C). It is mounted horizontally and a tantalum plug was built to prevent spillage. The plug has a 1.3 mm radius opening. A shutter that can be manually or remotely controlled via TTL exists at the opening of the cell. The crucible can hold 10 cc of material. It is heated to 1160 °C, providing a strong flux of atoms.

The cell is loaded with chunks of solid holmium $\sim$3 mm on a side. Prior to loading, the holmium is washed in Alconox, isopropanol, and acetone to remove contaminants. Using eq. 2.1, one can estimate the pressure inside the crucible at typical run temperature of 1160 °C at 0.34 Torr. The atomic flux Φ from the cell can then be calculated from the equation [50]

$$\Phi = \frac{1}{4} n \bar{v} A \tag{2.2}$$

The aperture A is of course $\pi(1.3\text{mm})^2$. The density n inside the crucible can be estimated as $P/(k_b T)$. The velocity distribution is that of a typical Maxwell-Boltzmann at temperature T, so its mean velocity $\bar{v}$ is $\sqrt{\frac{8k_B T}{\pi m}}$. We therefore calculate that $\Phi = 10^{16}$ atoms/s. At last loading in 2012 (four years ago as of this writing), about 20 g of Ho was added to the crucible. Assuming an experiment running eight hours a day, five days a week, we would expect our atomic source to last a year. We still have enough atoms to easily perform our experiments, so perhaps A should be reduced due to blockage from remaining solid holmium or perhaps contaminants to the bulk holmium prevent the emission of holmium atoms by raising the pressure inside the crucible. In addition, a variety of modifications to our experimental setup and long repair times for our lasers render the assumption of a work-week of high temperature experiments optimistic.

The source produces an atomic beam at 1160 °C. Its velocity distribution is described by the Maxwell-Boltzmann distribution for a beam geometry.

$$f(v) = \frac{2}{\alpha^4} v^3 \mathrm{e}^{\frac{-v^2}{\alpha^2}} \tag{2.3}$$

At $T = 1160$ °C, this distribution predicts only 0.01% of emitted atoms within a reasonable MOT capture velocity of $\sim$50 m/s. In section 2.2.1, we discuss the addition of a red-detuned slowing beam to transform this distribution to include more atoms at slower velocities. This works without a Zeeman slower because our linewidth is so broad (32 MHz) that a large range of velocities are within a Doppler-shifted linewidth of the slowing beam. We can estimate the effects of our

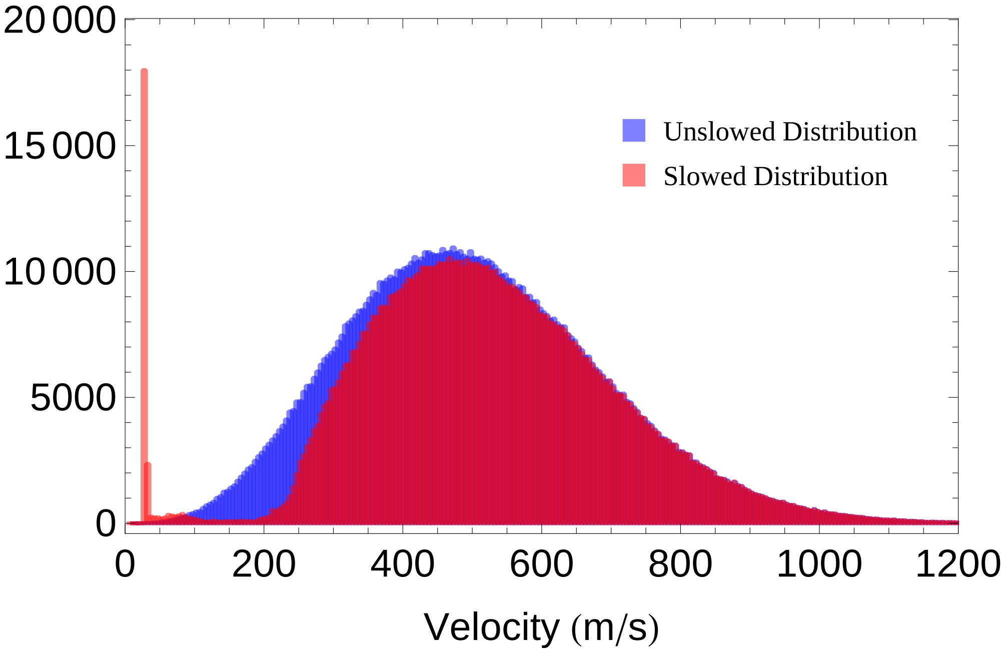

Figure 2.1 Results of a Monte Carlo simulation demonstrating the change in velocity distribution between an unslowed beam of 10^6 atoms at 1160 °C (Blue) and a slowed beam (Purple).

slower with basic atomic physics equations. The force that light at detuning δ of intensity I exerts on an atom with a transition linewidth γ is

$$F = \hbar k \gamma_p \tag{2.4}$$

$$\gamma_p = \frac{\gamma}{2} \frac{I/I_s}{1 + I/I_s + [2(\delta + kv)/\gamma]^2} \tag{2.5}$$

Our slower detuning is about 320 MHz and its power has varied from experiment to experiment, but is generally around 80 mW with a 1 mm waist. We can numerically solve the equations of motion for the velocity of the atoms in the distribution at z=78 cm, the distance from the oven to where our MOT beams cross. We perform a Monte Carlo simulation to find the new velocity distribution by generating a random set of 10^6 atoms with velocity distributions described by eq. 2.3. We apply our numerical solution to each atom in the set to find what its velocity at z=78 cm is. Some of the slower atoms will have already acquired a negative velocity and turned back. Our simulation finds that this is the case for about 10% of the atoms. However, we also find that 2%

of the original atoms have velocities lower than 50 m/s, a increase of about a factor of 200 (Fig. 2.1). This matches reasonably well with the MOT population gain of 1000 that we observe with our slower on and off (Ch. 3).

2.1.2 The Vacuum System

This section details the vacuum system used for a vast majority of the experiments in this thesis (Fig. 2.2). Very early iterations of the vacuum chamber can be found in [51]. An upgraded design is described in a chapter 6.

The chamber is divided into two sections: the source region and the science region.

2.1.2.1 The Source Region

The source region contains the source described in subsection 2.1.1. There is a bellows with three alignment screws attached to the back of the chamber that allow for small changes in output direction of the atomic beam. The motor for an atomic beam shutter is also attached here.

The source feeds directly into a spherical cube with several 2-3/4" viewports available for spectroscopy. The cube is also a connection to two vacuum pumps: a 20 L/s ion pump and a Pfeiffer HiCube 80 Eco turbo pump. The turbo pump can be shut off from the chamber by an all-metal angle valve. The holmium in this region is quite diffuse and fills the entire chamber, making it somewhat useful for spectroscopy experiments. The typical background pressures in this region are $\sim 10^{-7} - 10^{-8}$ T. It has been observed that the presence of holmium decreases the pressure by a factor of 5-10, probably by acting as a getter. This region ends at a Nor-Cal all-metal gate valve. All told, it is 85 cm long from the end of the motor to the gate valve.

2.1.2.2 The Science Region

Directly after the gate valve is a blank copper gasket with a 2.5 mm hole drilled in its center to collimate the atomic beam. Directly after the pinhole, there is a spherical cube with viewports for transverse cooling, spectroscopy, and vacuum connections. It is evacuated by a 35 L/s ion pump and the same Pfeiffer HiCube 80 Eco turbo pump that pumps the source region. It also has

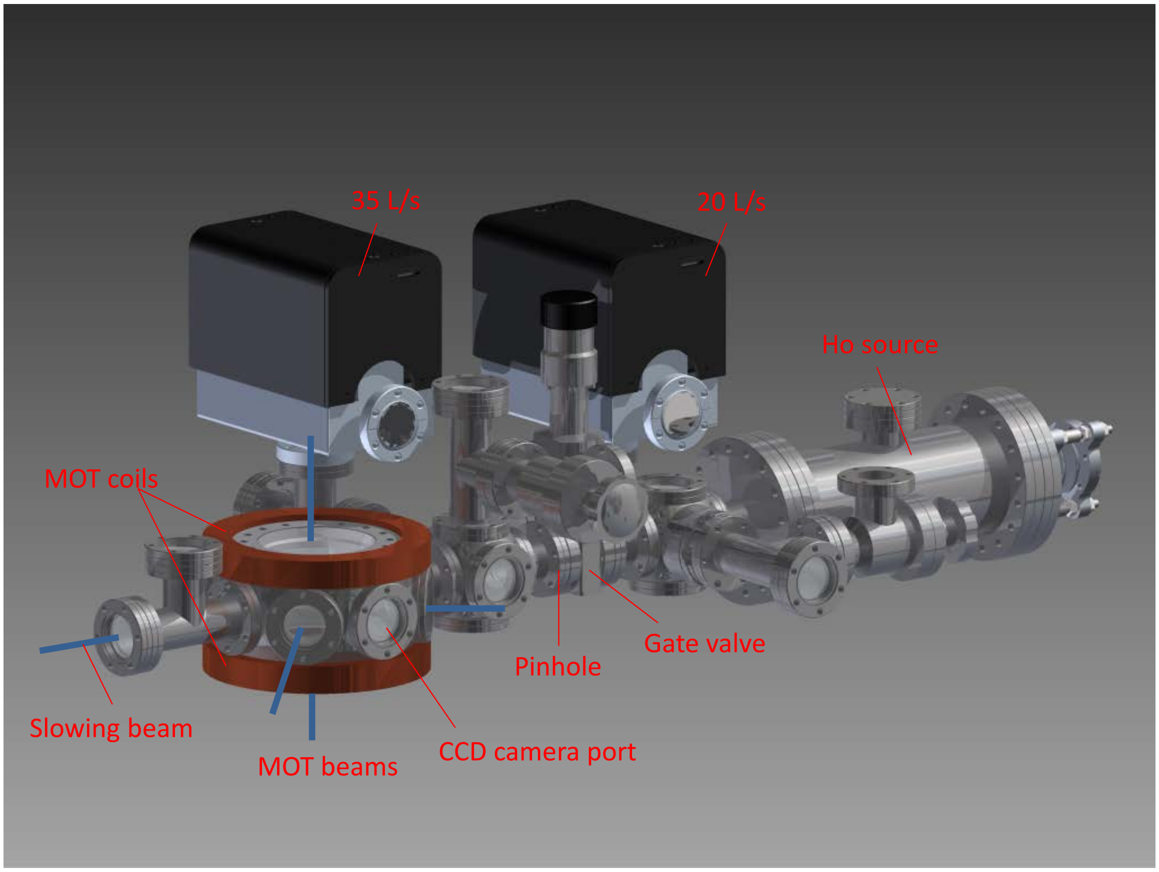

Figure 2.2 The vacuum system used for a majority of the experiments. The system is separated into two sections, the source region and the science region. The holmium source is located at one end. It attaches directly to a chamber with viewports available for spectroscopy and for vacuum connections. There is a gate valve separating the two regions. On the other side of the gate valve is another section available for transverse cooling, spectroscopy, and vacuum connections. The trapping region is inside the spherical octagon. A tee is opposite the source to hold a mirror to support the slowing beam.

an all-metal angle valve to close it off from the turbo pump, and the valves from each region are connected in such a way that the turbo pump can easily be connected to one, both, or neither of the regions.

The spherical cube is attached to a spherical octagon. This octagon has eight 2-3/4” ports around the perimeter and two 6” ports on the faces. One of the 2-3/4” ports is only used as the vacuum connection to the source region. The port directly opposite to the source connection is the entry port for the slower beam. The two 2-3/4” ports whose faces are perpendicular to the propagation of the atomic beam have variously been used for imaging, signal detection, absorption probe beams, and dipole trap beams. The remaining four 2-3/4” ports are spaced at 90°, so they are used for transverse MOT beams at 45° to the atomic beam. The 6” windows are used for the z-axis MOT beam and its retroreflection, the Rydberg excitation beam, a second CCD camera to view the experiment along the vertical axis, and are large enough to allow for a full wavelength of the 4.31 GHz $F = 4$ to $F = 5$ hyperfine splitting to enter the chamber. All of the windows are AR coated for visible light.

The Science region ends in a tee. Within this tee are two OFHC copper plates with 1/2” axial holes in them. These plates have radial set screw through-holes that allow them to be braced against the sides of the tee for positional stability. Tapped holes have been drilled in the to make them compatible with Thorlabs cage mechanics. Within these cage mechanics is a 1/2” visible mirror mounted at 45° to the atomic beam axis. The mirror can then be used to reflect a vertical slowing beam to propagate into the horizontal chamber. If this assembly were not present and if the slowing beam entered the spherical octagon directly, the atomic beam of holmium that is counterpropagating against the slower would coat the window and require regular vacuum breaking to clean the window. With this solution the atomic beam instead coats the mirror, which remains reflective even with holmium deposits on it and requires no further maintenance for operation.

The pressures reached in this region are routinely 10^{-9} T. This is improved when the holmium source is on as its large magnetic moment makes it an effective getter. When the source has been on, pressures in the region are $1 - 2 \times 10^{-10}$ T and sometimes reach 7×10^{-11} T.

2.2 The Laser System

There are three lasers used in our experiments: A titanium-sapphire laser and two diode lasers.

2.2.1 Titanium-Sapphire

The Ti:Sa laser is a commercially bought SolsTiS from M Squared. It is pumped by a 16 W 532 nm Sprout laser from Lighthouse Photonics. The Ti:Sa laser optimally emits a maximum of 5.15 W at 821 nm. The frequency can be tuned using a bi-refringent filter for coarse tuning, an

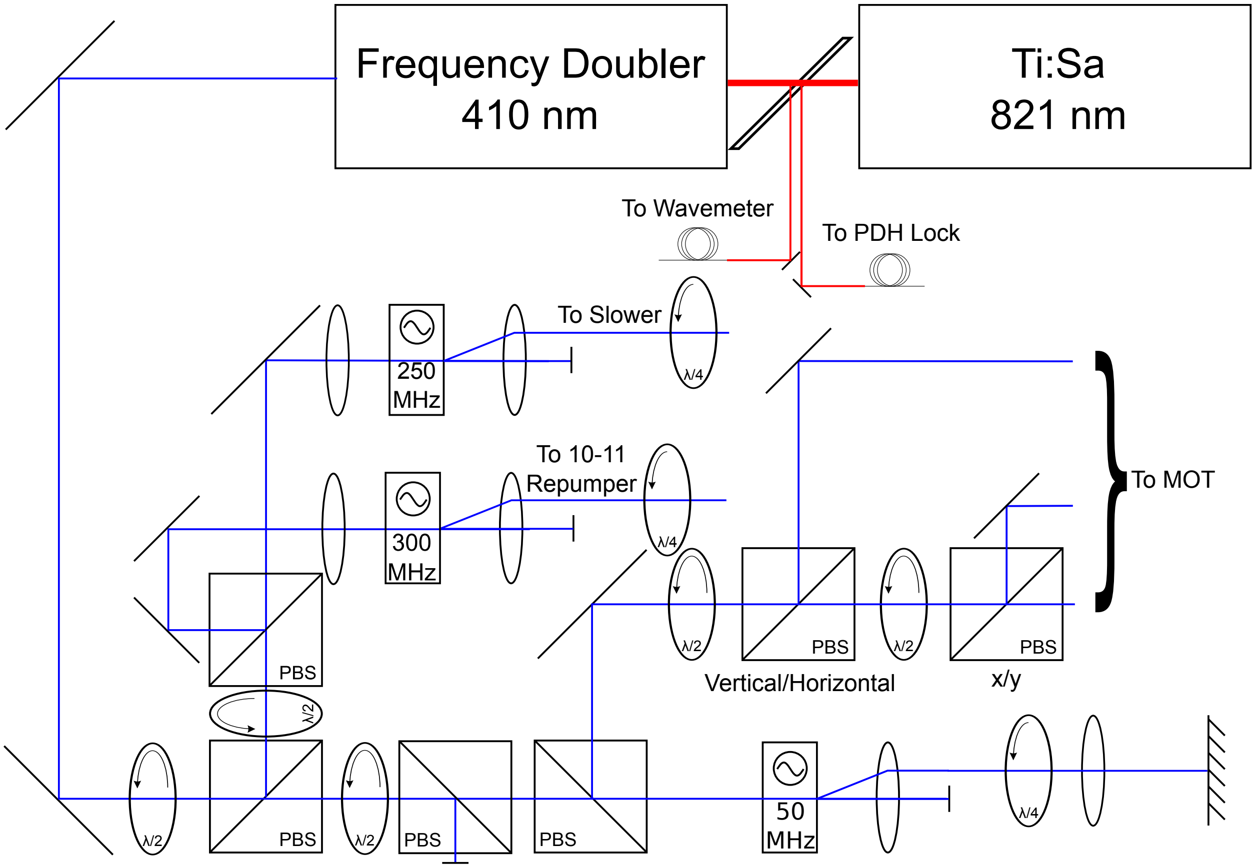

Figure 2.3 The optical setup of the MOT beams for the majority of the experiments in this thesis, excepting the ODT experiment. A frequency doubled Ti:Sa is locked to a ULE cavity and is used to produce slowing, MOT, and imaging light.

etalon for medium-finesse tuning, or by locking to a resonator controlled by a piezo for fine tuning. The resonator lock decreases the linewidth of the laser to 50 kHz. Its length can be changed and stabilized by an external voltage feeding back into an internal piezo. A glass plate picks off two low-level reflections that are used for wavelength monitoring and locking to an external ULE cavity described in appendix A. The Ti:Sa output is coupled into an M Squared external cavity doubler (ECD). It can provide up to 2.2 W of 421 nm light.

We use this laser for many critical functions, including the MOT cooling light, the slowing light, imaging light, and repumping (Fig. 2.3).

Most of the light is used for MOT cooling and imaging (Fig. 2.3). The light is double-passed through a Brimrose 50 MHz AOM with a double-pass efficiency of $\sim 25\%$. This provides us with a beam that can be rapidly tuned over 80 MHz without changing its alignment. Unless otherwise noted, the light is shaped into either 2.3 mm waist beams if we would like small MOT beams, or into 1.15 mm waist beams that are later expanded 10x into 1.15 cm beams for large MOT beams. The beam is split on two polarizing beam splitters (PBS) and each beam is circularly polarized by a $\lambda/4$ waveplate to form the three axes for the MOT beams. The powers in these beams are 40 mW for the small beams and 290 mW for the large. They are retroreflected to double the total incident power and form the MOT. The beams can be switched on and off in 320 ± 20 ns by the 50 MHz AOM.

Before the 50 MHz AOM, some light is picked off by a PBS. A second PBS further splits this into two branches, both containing A&A 250 MHz AOMs. One of these branches is tuned to 212 MHz and is used as the slowing beam with power 180 mW for small beams and 38 mW for large. Before entering the chamber, it is polarization rotated by a $\lambda/4$ waveplate to maximize its cooling power on the $|F, m_F\rangle = |11, 11\rangle \rightarrow |F', m'_F\rangle = |12, 12\rangle$ cycling transition.

The other branch is tuned to the difference between the $F = 10$ and $F = 11$ ground state hyperfine splittings and used as a repumper.

If less total power is required for the experiment, a PBS is placed after the slower pickoff to dump the extra light. This allows us to change the total power without changing AOM RF powers, which could change optical alignments through thermal expansion due to temperature change of the optical medium of the AOMs.

2.2.2 821 nm Diode

The 821 nm diode laser is a SANYO DL-8142-201 centered around 830 nm with an output of 150 mW. The diode is placed in a Littman-Metcalf ECDL configuration (Fig. 2.4). In this configuration, it can be tuned to 826 nm with only minor realignments of the second harmonic generation (SHG) cavity discussed later in this section. At 821 nm the ECDL puts out 60 mW [52].

20 mW of this is used for wavelength measurement and locking. It is locked to an Invar optical cavity with a FSR of 1.5 GHz and finesse $\sim$500. The cavity is contained in a vacuum can at $\sim 10^{-8}$

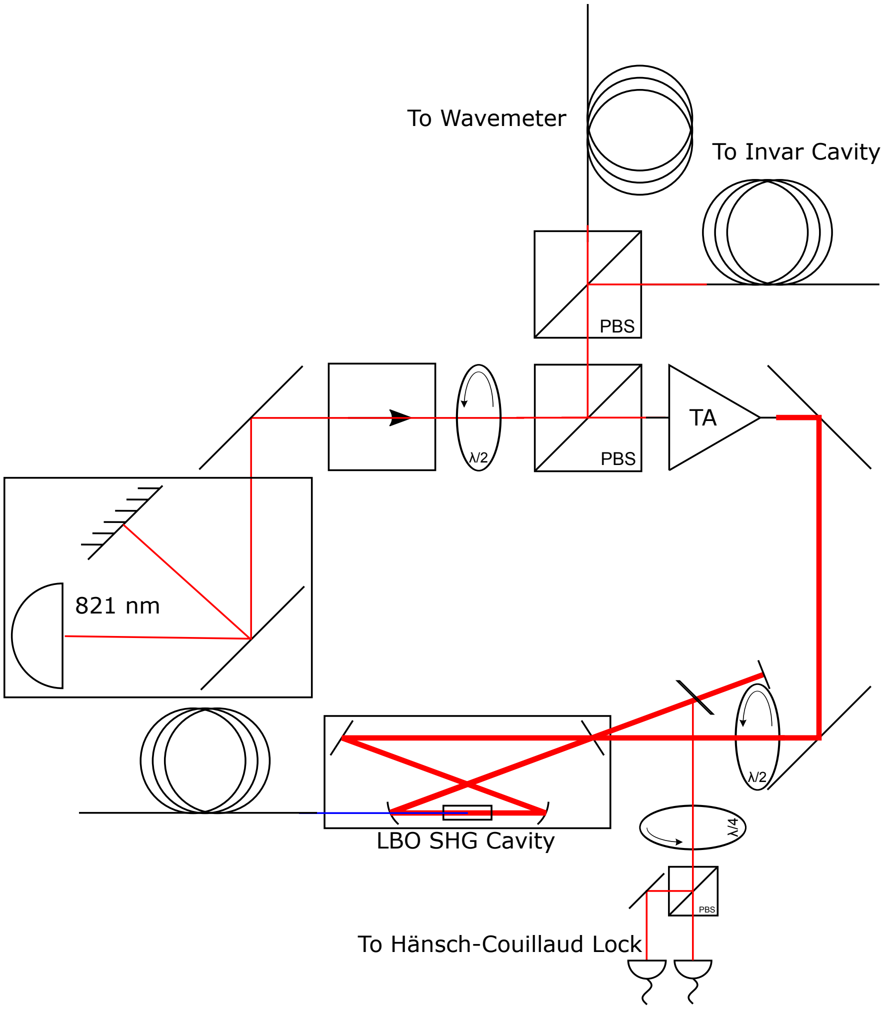

Figure 2.4 Optical layout of the frequency doubled 821 nm diode coupled into a fiber.

T with a pinched off copper seal, supported by to thin stainless steel rails and two Viton o-rings placed at the Airy points $\sim\frac{1}{5}$ of the cavity length from each side to reduce warping of the Invar spacer. The vacuum eliminates any drift from humidity or pressure variations, so the only drift is from thermal expansion or instability in the piezo voltage. The thermal stability $\Delta\nu$ of a cavity is given by the formula

$$\Delta\nu = \alpha\nu\Delta T \tag{2.6}$$

where the coefficient of thermal expansion $\alpha = 1.2 \times 10^{-6}\frac{1}{K}$ for Invar [53] and the laser frequency is typically $\nu = 365.1580$ THz. The vacuum can is temperature controlled by an Arroyo 5240 TECSource stable to ± 0.004 K [54]. This predicts a stability of 1.8 MHz at 821 nm and 3.6 MHz at 410 nm. This is expected to be somewhat better due to the long thermal time constant associated with the Viton o-ring supports, estimated to be on the order of several hours.

The remaining 40 mW of this is coupled into a Toptica TA-0830-1000-4 1 W tapered amplifier. This is coupled into a SHG cavity for 40 mW of 410 nm light. The frequency doubling crystal is LBO and the cavity is in a bow-tie configuration, locked with a Hänsch-Couillaud method. Full details of the doubling cavity can be found in [51]. This light is then coupled into a fiber for use in spectroscopy or for optical pumping on the $|F = 11\rangle \rightarrow |F' = 11\rangle$ transition at 410 nm, or as the second photon in a two-photon Rydberg transition at 413 nm.

When used as a Rydberg laser, the fiber can be oriented slightly off axis (<10°) to the vertical axis of the spherical octagon on the vacuum chamber through the 6" windows. The fiber coupler is mounted on a 6-axis platform, allowing for full control over the positioning and fine alignment of the Rydberg beam.

2.2.3 445 nm Diode Laser

Our dipole trapping laser is an OptLaser B1000 diode package centered at 444 nm. It has a linewidth of 3 nm (Fig. 2.5). Its output power can be controlled via a 5 V analog voltage input from 0 W to 970 mW. Its amplitude noise is about 3.6% with no noticeable spikes in the Fourier transform of the amplitude signal.

Its optics are combined with the imaging optics for the dipole trap as the camera is extremely sensitive and is easily overwhelmed by the trap laser shining directly into it, even when any practical number of filters are used (Fig. 2.6). A series of cylindrical lenses collimates the beam. Another lens focuses the beam and allows the focus to translate. The beam is passed through a 445 nm filter to remove any 410 nm spectral components that may be picked up on the camera. It then joins the beam path of the ODT imaging camera and is focused by the shared optics. This produces a waist of about 12 μm at the same place as the ODT camera is imaging.

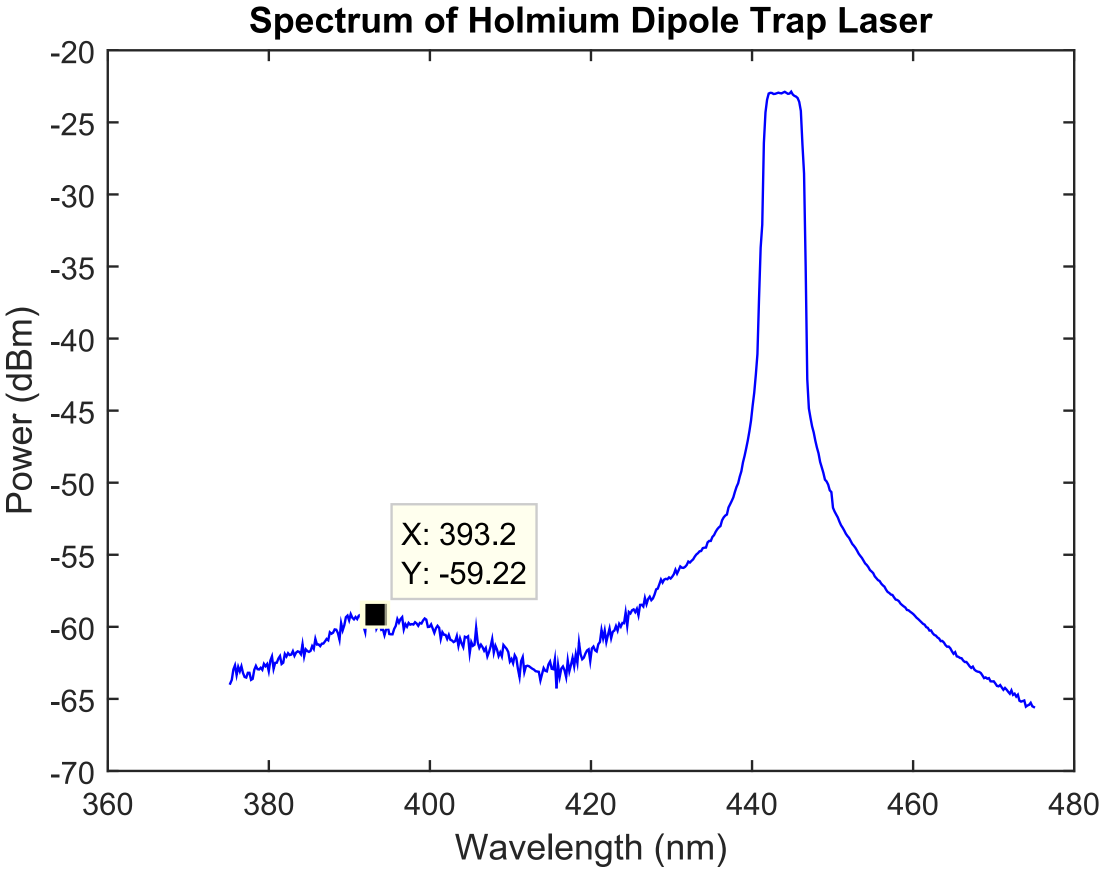

Figure 2.5 Measured spectrum of the 445 nm ODT laser.

2.3 Imaging

We have two cameras observing our experiment. The first is an Andor Technology Luca-R observing from an angle in the vertical direction. The second is a Princeton Instruments ProEM-512+ observing from the side.

2.3.1 Andor Technology Luca-R

The Luca-R EMCCD camera observes our experiments from above. It uses a zoom lens model Navitar Zoom 7000 TV for imaging and a Thorlabs FB410-10-1-v 410 nm filter to image. We use the maximum magnification of the lens, giving it a resolution of 15.7 μm/pixel and a field of view of 15.73x15.73 mm. The transmission through the zoom lens and the filter was 23%.

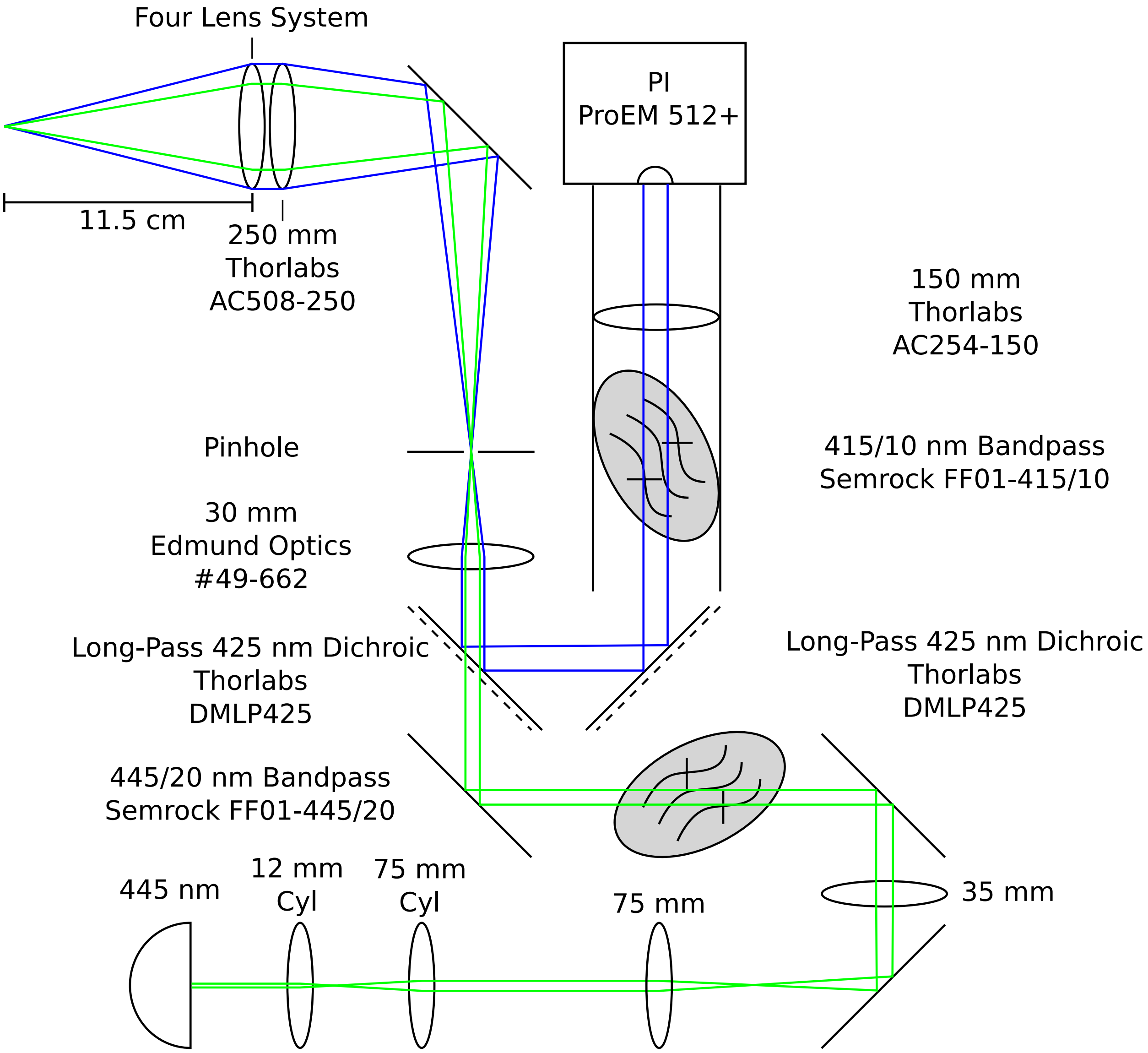

Figure 2.6 The optical setup of the ODT laser and the ODT imaging.

EMCCD cameras work by the photoelectric effect. Photons from a fluorescing camera create photoelectrons on the camera's CCD in a proportion described by the quantum efficiency, which are then multiplied by an EM gain using a cascading effect similar to that found in photomultiplying devices. This signal is then converted to a voltage and read out as *counts* on the camera, where some number of electrons can trigger one count depending on the analog gain of the readout process. It is important to know how many photons will trigger a signal on our camera. The camera's quantum

EM Gain	Counts/γ (w/ optics)	e^-/γ (413 nm, no optics)
Off	0.03	0.14 (QE)
2	0.33	1.58
10	0.75	3.62
20	1.39	6.67
200	16.78	80.67
500	41.11	197.63
1000	72.81	350.09

Table 2.1 Signal/γ of Luca-R camera.

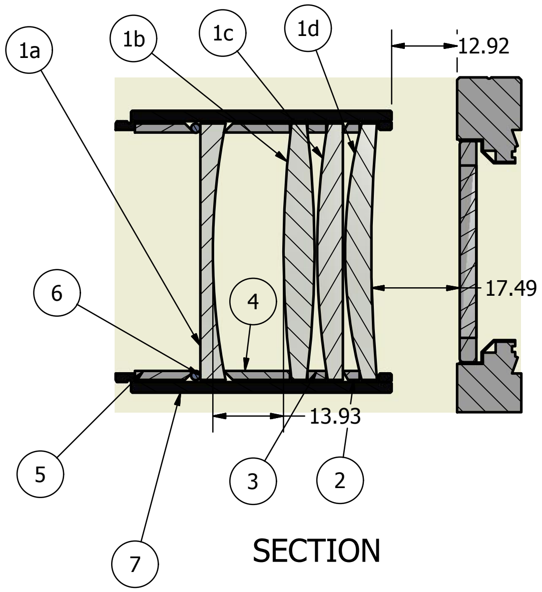

PARTS LIST		
ITEM	QTY	PART NUMBER
1a-d	1	KPC067/LB1199/LA1256/LE1985
2	1	0.13" spacer
3	1	0.145" spacer
4	1	0.515" spacer
5	1	0.460" spacer
6	1	O-Ring
7	1	Thorlabs SM2L02

Figure 2.7 A four-lens system to minimize optical aberrations at large numerical apertures.

efficiency for several gains was measured by imaging a 1 mW 410 nm beam attenuated by several ND filters with measured optical densities. The results are shown in table 2.1 and can be used to count scattered photons from our atomic sample.

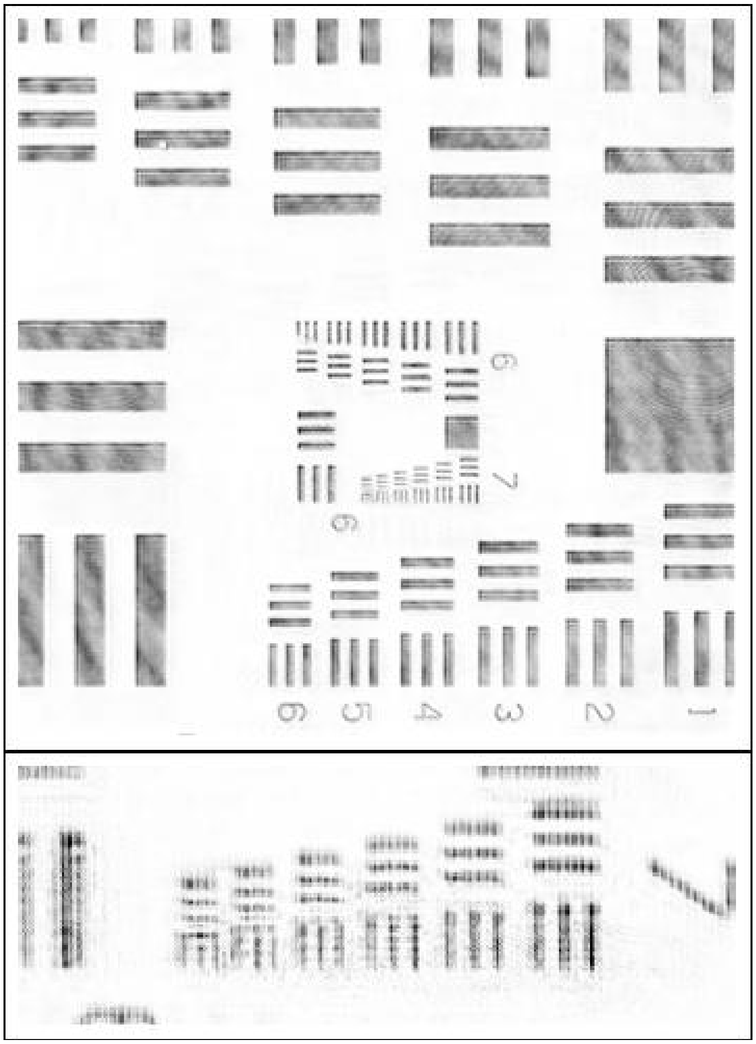

Figure 2.8 Imaging the USAF chart. Features of 2-3 μm are resolvable.

2.3.2 Princeton Instruments ProEM-512+

The ProEM observes the experiment from the side. Its imaging optics (Fig. 2.6) are much more powerful than the zoom lens, giving it a magnification of 10.77. It has a resolution of 1.45 μm/pixel and a field of view of 742 μm, making it extremely useful for detailed images of the MOT or the ODT, but difficult to use for things that require a large field of view such as MOT alignment. These optics consist of a four-lens system that sets their working distance to about 11.5 cm and minimizes optical aberrations (Fig. 2.7). The working distance was chosen to place the light collection optics as close as possible to the center of the vacuum chamber where the experiments

Analog Gain	EM Gain	Counts/γ	Estimated e^{-}/γ (410 nm, no optics)
Low	1	0.017	0.37 (QE)
	2	0.029	0.63
	20	0.196	4.27
	200	1.35	29.5
	1000	5.10	111
Medium	1	0.028	0.38 (QE)
	2	0.050	0.67
	20	0.326	4.37
	200	2.45	32.9
	1000	10.2	136
High	1	0.047	0.26 (QE)
	2	0.098	0.54
	20	0.624	3.42
	200	4.68	25.6
	1000	19.4	106

Table 2.2 Measurements of the signal/γ with the optics described in Fig. 2.6 in place.

happen ($\sim$10 cm) and maximize the numerical aperture of the system at 0.22. Features of about 2-3 μm are resolvable (Fig. 2.8). The camera shares optics with the ODT laser and therefore has two dichroics and a narrow band-pass filter to protect the camera. Taken together, the optical transmission through the system was 48%. The camera has a low, medium, and high analog gain that corresponds to 10.91, 6.71, and 2.74 e^{-}/count at 10 MHz. It also has EM gain up to 1000. The quantum efficiency of the camera in a variety of gain settings with these optics is shown in table 2.2. The ODT laser is always turned off during imaging to prevent background light in the picture and to ensure that the imaged holmium atoms are not AC Stark shifted.

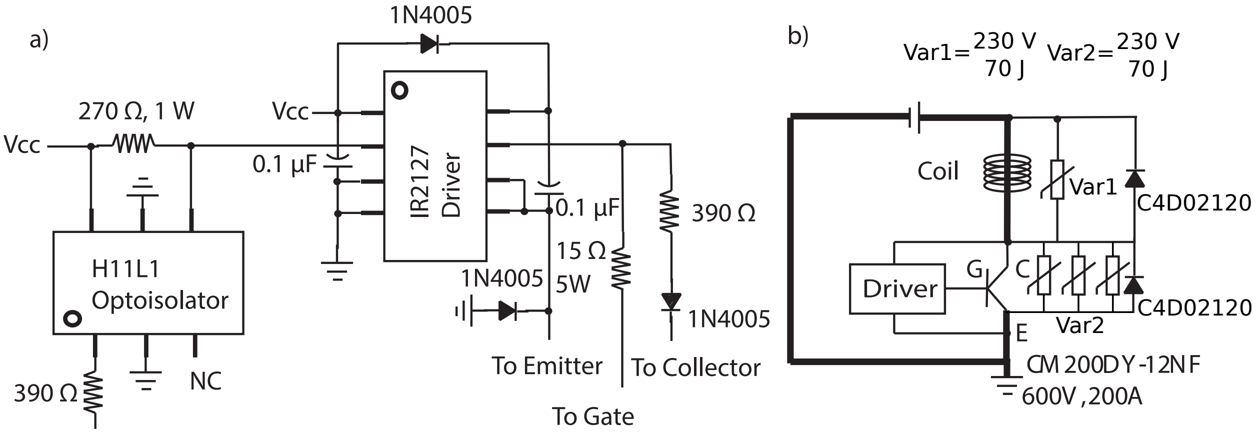

Figure 2.9 a) A schematic of the driver for the IGBT switch. b) The full schematic of the switching circuit.

2.4 Electrical systems

2.4.1 MOT Coils

2.4.1.1 Design

The holmium MOT optimally requires a magnetic field gradient of $\sim$30 G/cm to operate. This gradient is provided by copper magnetic field coils mounted on the 6” faces of the spherical octagon in the science region (Fig. 2.2). The wire has a 0.508 cm square cross-section that is hollow to allow for the option of water cooling and corresponds to a 10 gauge wire. Each coil has a height of 7.6 cm, inner radius of 8.5 cm, and outer radius of 12 cm. There are a 15 wraps vertically and 7 wraps radially, giving 105 total wraps. The coils are separated by 10 cm, giving a gradient of 1.2 G/cm/A. 30 A are used for a total gradient of 35 G/cm. The total inductance of the coils is $\sim$2 mH. The coils are mounted on an aluminum coil form. With the additional conductive cooling due to the mount and the conduction to the chamber, the temperature of the coils is typically 60 °C and requires no additional water cooling.

2.4.1.2 Control

The need for high current and fast switching of the MOT coils prevents the use of many current controllers. The coils are controlled by a homemade circuit using an IGBT switch (Fig. 2.9). This

Axis	Turns	Radius	Coil Separation	G/A	Power Supply
x	40	3.4 cm	20 cm	0.5	10 A Power Supply
y	40	3.4 cm	20 cm	0.5	10 A Power Supply
z	55	7.6 cm	10 cm	5.3	3 A Current Controller

Table 2.3 Technical specifications of the shim coils. The magnetic field in column 5 is for the center of the vacuum chamber.

is a circuit that allows current to pass through our MOT coils when the IGBT is closed. A varistor and diode are in parallel with the coil aligned in such a way as to prevent current from flowing down their respective paths when the current flows counter-clockwise around the circuit. A TTL pulse triggers the driver circuit to open the fast-switching IGBT, stopping the current flow through the MOT coil. Because of this sudden change in current, a back EMF is generated in the coils. At this point, current is free to pass through the varistors and diode, leading to faster power dissipation in the circuit and speeding the decay of the magnetic fields. With this circuit, the 1/e time to shut off the MOT coils is 10 ± 2 ms. Because of the large power draw and inductance of the coils, we find that shutting off any faster produces large voltage spikes on the ground resulting in instabilities that are particularly disruptive to laser locks.

The IGBT is protected by a series of varistors and another diode.

2.4.2 Shim Coils

We have shim coils to cancel out stray magnetic fields and to apply a bias z magnetic field if necessary. The shim coils are placed on the viewports used by the MOT beams. They are wound coils made of 20 G copper wire. Table 2.3 give the relevant specifications for the shims. The power supply for the z shims is a homemade current controller capable of supplying 3 A. It allows rapid control of the coil currents with an analog voltage input.

The shims use 20 gauge wire with 40 turns per coil on the x and y axes, and 55 turns on the z axis. The x and y shims are controlled by a power supply that can supply up to 10 A. The z shim coils are controlled by a current controller capable of supplying 3 A.

2.4.3 Control Hardware

Our experiment primarily controlled via the control software described in [55]. It controls most of the dynamic aspects of the experiment, including TTL pulse timing, analog input and output, imaging, and RF frequencies for a variety of devices.

The TTL pulses are provided by a National Instruments SMB2163 with 32 5 V TTL outputs[56]. Input and output analog signals are controlled with a National Instruments BNC2090A[57]. We have a DDS generator that provides four channels of RF frequencies up to 400 MHz and 0 dBm[58]. Each channel is capable of supporting four profiles for increased flexibility during the experiment. The DDS generates the RF signals for the ULE sideband lock, the 50 MHz MOT AOM, the slower AOM, and the repumper AOM.

2.5 Conclusion

In this chapter, we have described the equipment that we used during our experiments. The details and calibrations found here are used throughout this thesis to discuss our experimental conditions and results.

Chapter 3

Magneto Optical Trapping of Holmium

3.1 Broad-Line Ho MOT

MOTs are a very standard and widely used tool in cold-atom physics. MOTs have been demonstrated for approximately 30 different neutral elements. Open shell lanthanides were not considered good candidates for magneto-optical trapping due to their complex electronic energy structure until Er was trapped in 2006 [26]. Because of the low vapor pressure of the rare earths, the MOTs are usually supplied with atoms via an oven-produced atomic beam that has been slowed with a counterpropagating slowing laser coupled with a Zeeman slower. The Doyle group has recently demonstrated a Ho MOT that avoids the complicated Zeeman slower technique by precooling the atomic beam with a He buffer-gas[30]. We present data on a Ho MOT created with a slowing beam but without Zeeman-shifting the atomic beam and without repumping.

A Grotrian level diagram of Ho is shown in Fig. 3.1. The ground state has J=15/2 and odd parity. There are eight dipole-allowed transitions at wavelengths longer than 410 nm (24361 cm^{-1}) with even parity and J=17/2 labeled 1-8. Since there are no odd-parity levels with $15/2 \leq J \leq 19/2$ in between the ground state and the upper levels of the six transitions labeled 1-6, these transitions are cycling. The 410.5 nm transition to $4f^{11}6s6p(^1P), J = 17/2$ at 24361 cm^{-1} (labeled 9) has available decay channels to odd-parity levels, but closer examination of these levels reveals that almost all of the possible transitions have $|\Delta j|>1$ on a single electron or are forbidden due to intercombination spin changes. The only transition which is allowed for single-electron jumps is to $4f^{11}5d6s(^1D), J = 17/2$ at a transition energy of 475 cm^{-1}. The expression for the radiative linewidth γ is

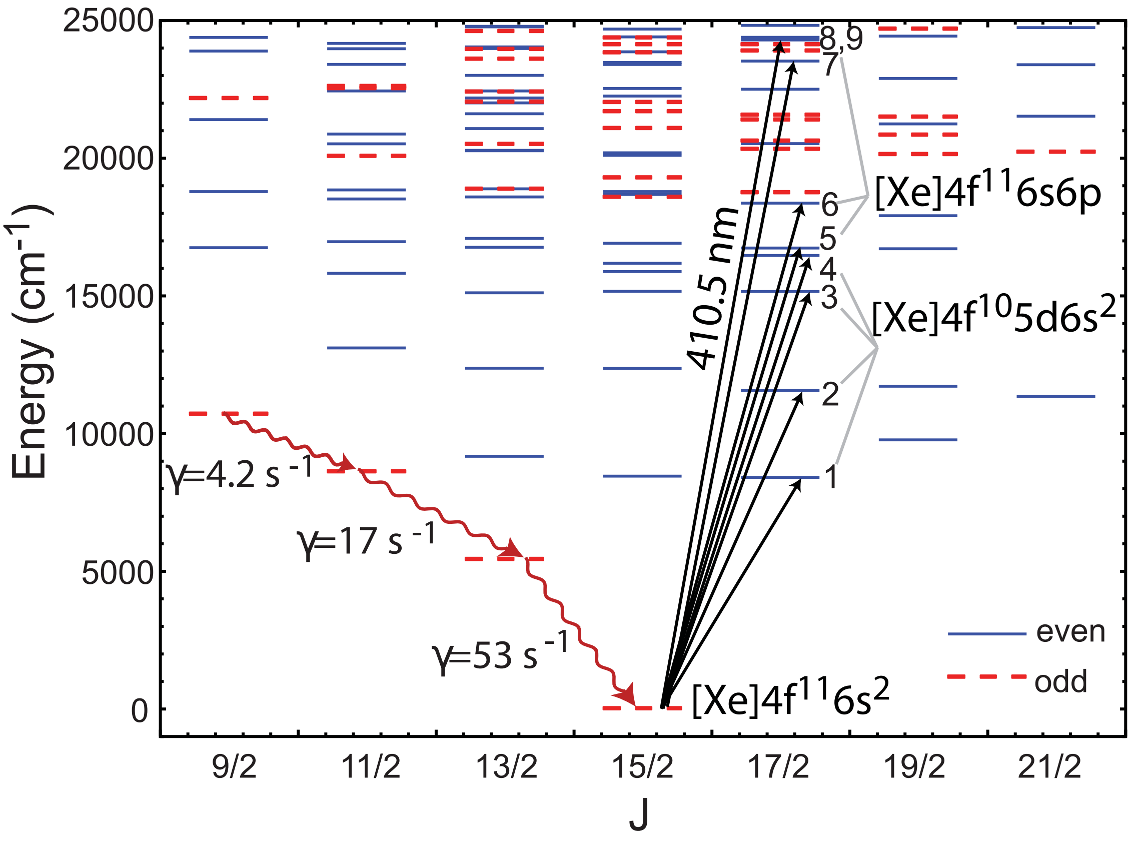

Figure 3.1 Grotrian diagram of Ho I. Levels 1-9 are lines that are potentially suitable for MOT cooling light. All dipole-allowed lines at J=13/2 have decay channels into metastable states. Unmarked dipole allowed channels at J=17/2 are two-electron transitions.

$$\gamma = \frac{\omega_{eg}^3 e^2}{3\pi\epsilon_0 \hbar c^3} \sum_{m_g=-J_g}^{J_g} \sum_{q=0,\pm1} |\langle n_g L_g s J_g m_g | r_{-q} | n_e L_e s J_e m_e \rangle|^2 \tag{3.1}$$

where ω_{eg} is the energy of the transition between $|g\rangle = |n_g L_g s J_g m_g\rangle$ and $|e\rangle = |n_e L_e s J_e m_e\rangle$. Because the strength of the transition goes as ω_{eg}^3, the decay rate to $4f^{11}5d6s(^1D), J = 17/2$ is much smaller than that to $4f^{11}6s6p(^1P), J = 17/2$. Using hydrogenic orbitals we can roughly estimate the decay to that state as 4000 s^{-1}, much smaller than the experimentally determined rate of 204×10^6 s^{-1} to the ground state.

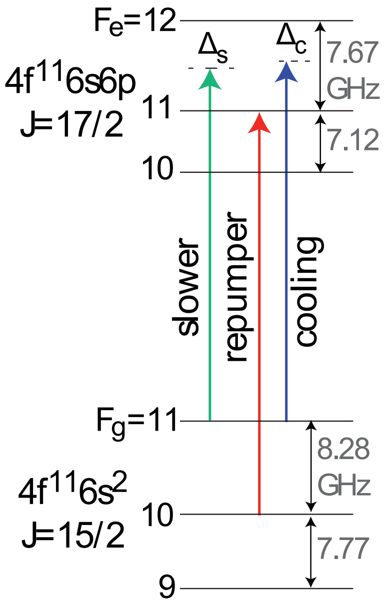

Figure 3.2 The level diagram of the participating levels of the MOT cooling, including the laser detunings used.

3.1.1 Experimental Parameters

The experimental apparatus is described in detail in chapter 2. The apparatus produces an atomic beam of Ho and the laser light for both the MOT and slowing beams. The MOT beams were arranged in a standard six-beam $\sigma_+ - \sigma-$ configuration. The beams had Gaussian waists of ($1/e^2$ intensity radius) of 2.3 mm and total incident power of 40 mW, which was doubled by retroreflecting the beams. The cooling light was detuned for the $F = 11 \rightarrow F' = 12$ cycling transition by $\Delta_c \sim -1.5\gamma$. The repumper light was tuned to $F = 10 \rightarrow F' = 11$ and overlapped with all MOT beams. The slowing beam was circularly polarized and detuned by $\Delta_s = -2\pi \times 320$ MHz from the $F = 11 \rightarrow F' = 12$ transition (Fig. 3.2). The slowing beam had a power of 140 mW and was focused to a waist of 1.0 mm. Additional data was taken with 290 mW of MOT light, MOT beam waists of 1.15 cm, and 38 mW of slower light.

The hyperfine energies shown in Fig. 3.2 were calculated from known values of the A and B constants for the ground state [59] and measured values for the excited state. We measured the

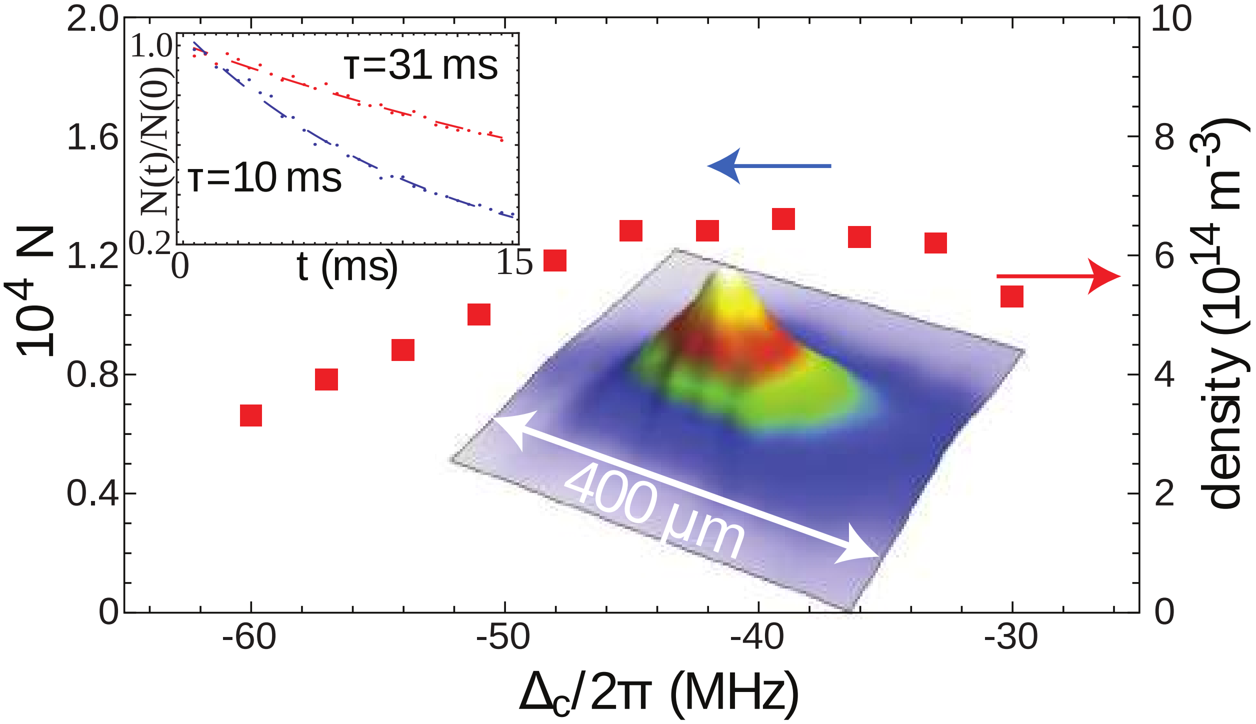

Figure 3.3 MOT population and density as a function of detuning. Sample decay curves are shown in the inset.

hyperfine constants of the upper level of the cooling transition using modulation transfer spectroscopy in the hollow cathode lamp. Fits to our data gave $A = 654.9 \pm 0.3, B = -620 \pm 20$ MHz.

3.1.2 MOT Number Measurements

With the slowing beam turned on but no repump light, we achieved a typical MOT population of $N{\sim}1.5 \times 10^4$ and atomic density of $n_a{\sim}6.5 \times 10^{14}$ m^{-3}, as shown in Fig. 3.3. The data taken with the larger MOT beams gave larger MOTs with up to $N = 2 \times 10^5$ atoms.

3.1.3 MOT Temperature

As shown in Fig. 3.5, we observe deep sub-Doppler cooling well below $T_D = 780\mu$K. Data was acquired by observing MOT expansion and fitting to Gaussian density profiles. The theoretical dependence of the molasses temperature with respect to detuning is given by [60]

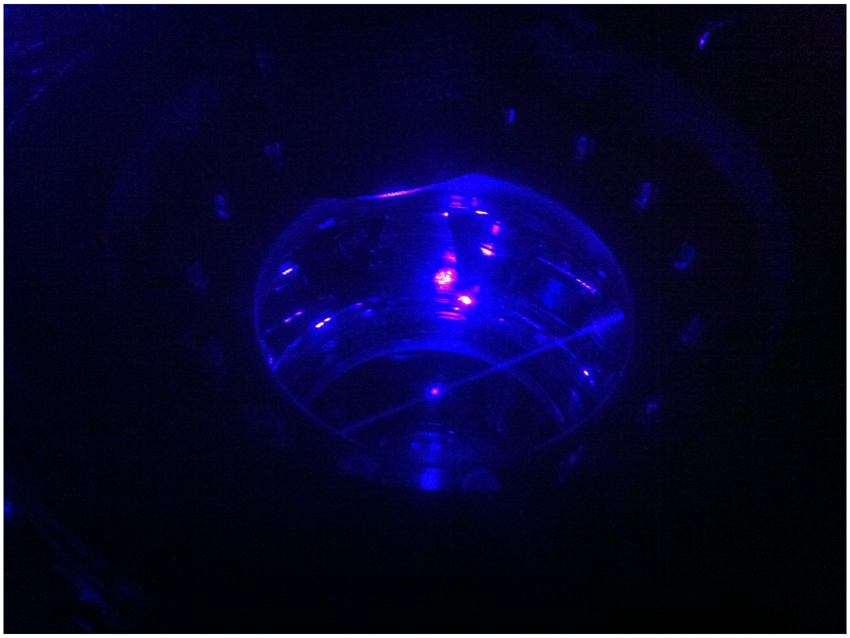

Figure 3.4 A picture of the MOT taken with a finely tuned and calibrated iPhone 4.

$$T = T_0 + \frac{\hbar\gamma^2}{2k_B|\Delta|}\frac{I}{I_s}\left(a + \frac{b}{1+4\Delta^2/\gamma^2}\right), \tag{3.2}$$

with a,b being constants and T_0 being the low-intensity temperature limit. The parameters a, b are known for low angular momentum transitions [60] but have not been calculated for the $F = 11 \leftrightarrow F' = 12$ Ho cooling transition. Using separate fit parameters for the horizontal and vertical temperature, Eq. 3.2 reproduces the observed dependence on detuning quite well. Anisotropic cooling has been observed in Dy MOTs [61] and may be due to large magnetic moments in rare earth elements. Due to the near equality of the g factors of the ground state of $F = 11$ and $F' = 12$, 0.82 and 0.83, temperatures reaching ten times below the Doppler limit are achieved with relatively small detunings.

3.1.4 Repumping

When the repumper was turned on tuned to the $F = 10 \rightarrow F' = 11$ transition, the atom number values increase by less than 1%. The negligible influence of the repump light is due to the fact that

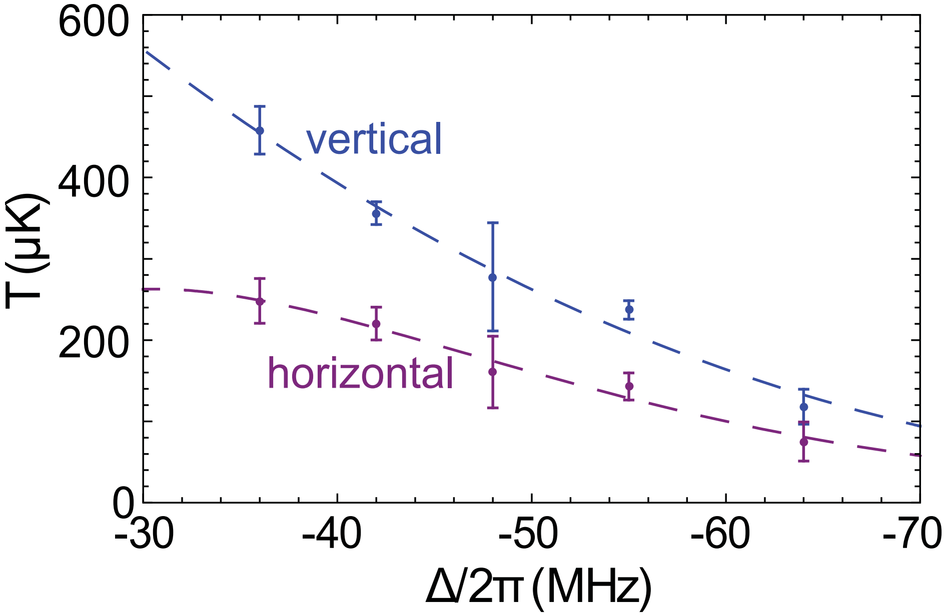

Figure 3.5 MOT temperature at a saturation parameter $I/I_s = 1.1$. The temperatures were extracted from fits to time-of-flight data for free expansion times up to 15 ms.

the cooling light also repumps the population in $F = 10$ much faster than the depumping rate out of $F = 11$. The scattering rate of the light detuned by Δ is given by

$$\frac{\gamma}{2} = \frac{I/I_s}{1 + 4\Delta_c^2/\gamma^2 + I/I_s} \tag{3.3}$$

where I is the total intensity of the six MOT beams and I_s is the saturation intensity of the MOT atoms. The saturation intensity is $2.76 I_{s0}$ where $I_{s0} = 614.0$ W/m^2 is the saturation intensity for $|F = 11, m_F = 11\rangle \leftrightarrow |F = 12, m_F = 12\rangle$, and the factor of $2.76 = 3(2\times11+1)/(2\times11+3)$ accounts for averaging over Zeeman substates and the randomly polarized light in the MOT region.

The depumping rate to $F = 10$ can be calculated by averaging over m_F levels and light polarization and accounting for the branching ratios of the fluorescence decay to give the formula

$$r_R = \gamma^3 \left[\frac{105}{69938\Delta_{F'=F}^2} + \frac{455}{17904128\Delta_{F'=F-1}^2} \right] \frac{I}{I_s}. \tag{3.4}$$

In this case, $F = 11$ is the F value for the lower level of the cycling transition, $\Delta_{F=F} = \Delta_{(F+1)_e,F'} + \Delta_c$, $\Delta_{F'=F-1} = \Delta_{(F+1)_e,(F-1)_e} + \Delta_c$ are the detunings of the MOT light from $F' =$

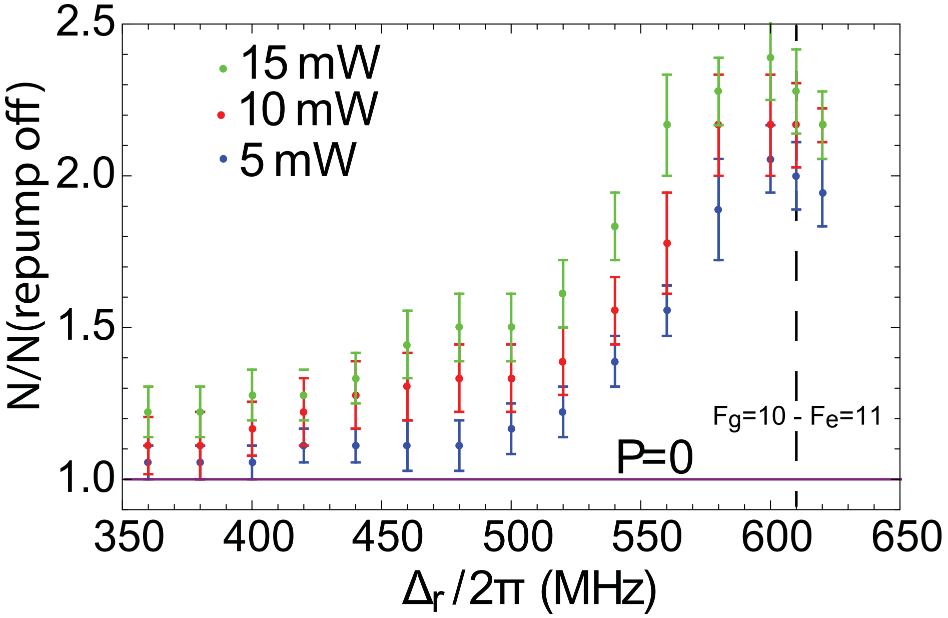

Figure 3.6 MOT population without a slower with different detunings of a repumper. The MOT population is normalized to that with no repumper on.

11 and $F' = 10$, and we have assumed the light is far detuned so that we may replace factors of$(1 + 4\Delta^2/\gamma^2 + I/I_s)^{-1}$ by $\gamma^2/(4\Delta^2)$. The excited-state hyperfine splittings shown in Fig. 3.2 are $\Delta_{12,11} = 2\pi \times 7.67$ GHz and $\Delta_{12,10} = 2\pi \times 14.79$ GHz. For our largest detuning $\Delta_c = -2\gamma$, $r_R = 80\ \mathrm{s}^{-1}$ and $r_R/r = 3.3 \times 10^{-6}$. As reasoned above, the decay to the metastable dark states should be small compared to the decay channel provided to ground and can therefore be neglected in the current analysis. We show this quantitatively in a later section 3.1.5.

The depumping rate is balanced by the repumping rate of the Raman process $F = 10 \rightarrow F' = 11 \rightarrow F = 11$. The cooling light is detuned from $F = 10 \rightarrow F' = 11$ by $\sim$650 MHz. The resulting repumping rate is $8 \times 10^5\ \mathrm{s}^{-1}$. This implies that the population is 99.9% in the $F = 11 \rightarrow F' = 12$ cooling cycle, consistent with our repumper observations.

The effect of the repumper is more significant when the MOT is operated without a slowing beam. In this case the MOT captures only a very small fraction of the low-velocity tail of the atomic beam, and the laoding rate is reduced by almost three orders of magnitude, resulting in a very small MOT with $N = 40$ atoms, again without a repumper. Turning on the repumper increases N by a factor of up to 2.5, depending on the detuning of the repumper, as shown in Fig.

3.6. The increase in atom number is not due to repumping because the cooling light already acts as an efficient repumper as was discussed in the previous paragraphs. We instead interpret the data as indicative that the slower is also slowing the $F = 10 \rightarrow F'$=11 state. Since there are 23 $F = 11$ and 21 $F = 10$ Zeeman states, we would expect roughly a factor of two increase, which is what we see in the data. No such increase is seen when the slower is on because the slower is only efficient on the $F = 11$ cycling transition, so any additional atoms from the repumper beam are negligible.

3.1.5 Loss mechanisms

We studied the internal-state dynamics by loading the MOT into a steady state with the slowing beam on and then measuring the decay lifetime with the slowing beam turned off to greatly reduce loading, but leaving the magnetic quadrupole field on. The population decay can be modeled with the rate equation [62]

$$\frac{dN}{dt} = R_{off} + \Gamma N - \beta N^2. \tag{3.5}$$

Here R_{off} is the loading rate with the slowing beam off. The loss rate is $\Gamma = (1 - \rho_{ee})\gamma_{bg} + \rho_{ee}(\gamma_{la} + \gamma_{ms})$, where γ_{bg} accounts for losses due to collisions with background gases, γ_{la} is the loss rate associated with light-assisted collisions between excited and background atoms[63], γ_{ms} is the loss rate due to scattering into dark metastable states, and β accounts for losses from collisions of trapped atoms.

Measurements of the MOT number decay curve with the slowing beam turned off showed no indication of faster two-body loss ($\beta \approx 0$). The MOT lifetime was found to range from 10 to 43 ms as the detuning was scanned from -5 to -50 MHz. Representative decay curves are shown in Fig. 3.3. Combining

$$r = \gamma \rho_{ee} \tag{3.6}$$

with eq. 3.3 we find that $\gamma_{bg} \approx 1 \pm 1$ s^{-1} and $\gamma_{ms} + \gamma_{la} \approx 300.0 \pm 100.0$ s^{-1}. Because γ_{la} is unknown, we can take 300 s^{-1} as an upper limit of the metastable decay rate and confirm our results in section 3.1.4. This rate is large compared to other rare earths [28, 64] but small compared

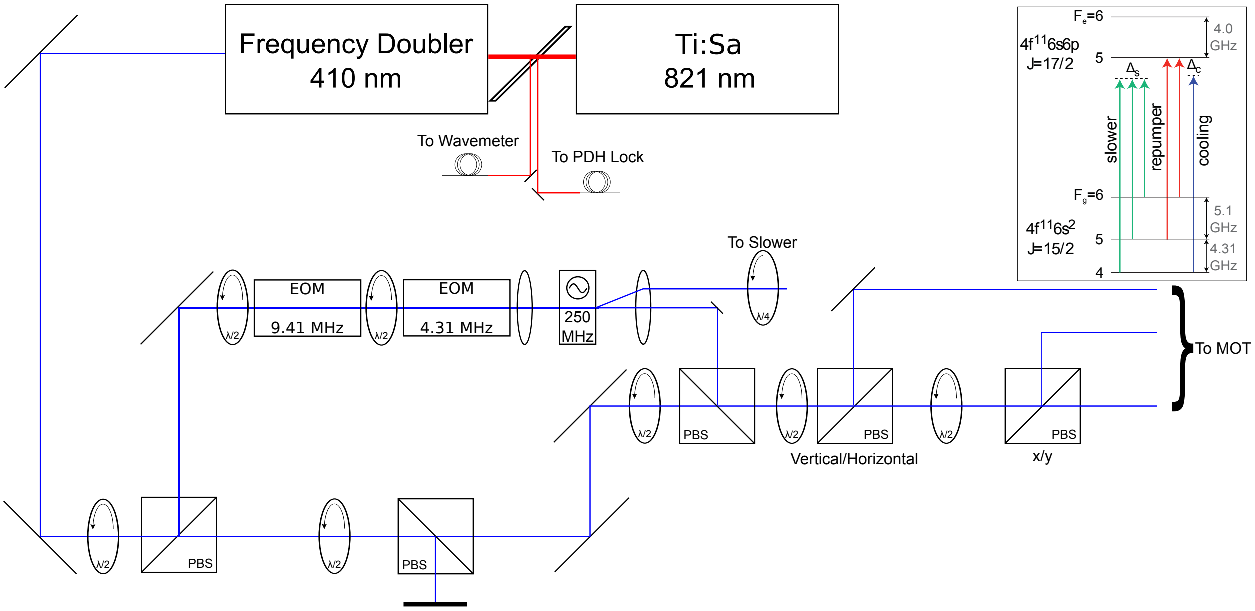

Figure 3.7 Modifications to the MOT setup for a $F = 4 \rightarrow F' = 5$ MOT. Two EOMs have been added to add repumpers to the cooling, slowing beams. Inset: Detunings of the beams involved in cooling.

to another Ho MOT experiment that measured the same value[30]. That experiment used a high pressure of He buffer gas to pre-cool the atoms, which may account for some of the discrepancy.

3.2 $F = 4 \rightarrow F' = 5$ MOT

Because the $F = 11$ hyperfine level is the most energetic of the hyperfine states, further cooling into an optical dipole trap (ODT) is susceptible to hyperfine changing collisions that can heat the atoms out of the trap very quickly. This makes a MOT that cools primarily on the $F = 4$ to $F' = 5$ transition of the 24360 cm^{-1} line of particular interest since it is the least energetic state and therefore immune to such collisions. This MOT is particularly challenging as the excited state decays not only back to $F = 4$ but also to $F = 5, 6$. Repumpers are needed to bring atoms lost to those states back into the cooling cycle.

We added two EOMs to our experimental setup to modulate a carrier beam's frequency at 4.31 and 9.41 GHz to repump our atoms on the $F = 5, 6 \rightarrow F' = 5$ transitions (Fig. 3.7). These EOMs added frequency sidebands with efficiencies of 33% (nearly the maximum efficiency achievable for an EOM) and 10% in each first order, respectively. The EOMs had a maximum rated optical power of 130 mW at 410 nm. The frequencies of these were fine-tuned by observing their signal in a saturated absorption spectroscopy experiment on a Ho hollow cathode tube.

The PBS pickoff from the main beam was set to allow 130 mW down the EOM/slower path. Half-waveplates rotated the polarizations of the beams to align properly with the EOM crystal axes for maximum frequency modulation. After the EOMs, an AOM was placed with a larger modulation frequency of 312 MHz to compensate for the removal of the AOM on the MOT beam lines and its first order diffraction was used for a slowing beam since that detuning was suitable for the MOT on the $F = 11 \to F' = 12$ line. This ordering is important because it prevents the slower from depumping the $F = 4$ state before the atoms even reach the MOT beams. It also allows us to collect slowed $F = 5$ and $F = 6$ atoms from the beam and provides some repumping when overlapped with the MOT.

The AOM that previously switched and detuned the MOT beams was removed for extra power and to allow it to be easily recombined with the zeroth order of the slower AOM. The zeroth order beam was combined on a PBS. A beam dump was installed on the main MOT beam line to allow for adjustment of the ratio of modulated and unmodulated.

To prepare the experiment, the EOMs were first turned off. The lasers were first tuned to the $F = 11 \to F' = 12$ transition. A MOT was made at this frequency and the mirror alignments fine-tuned for maximum population. The EOMs were then turned on and tested by measuring the transmission of the laser through a Fabry-Perot cavity. The lasers were collectively tuned to the $F = 4 \to F' = 5$ transition. While fluorescence from background atoms was seen, no MOT was observed.

Several other configurations were tried, including:

1. Modulating only the slower light.
2. Modulating only the MOT light.
3. Modulating only the MOT light and turning the slower off.

4. Dumping all of the MOT light that had not passed through the EOM. A $F = 11 \rightarrow F' = 12$ MOT was observed with this method, created only out of the sidebands.

5. Tuning the zeroth order of the AOM to be resonant with the $F = 6 \rightarrow F' = 5$ line to make a strong repumper relative to the main $F = 4 \rightarrow F' = 5$ MOT light, and relying on second-order EOM modulation to provide the repumper at $F = 5 \rightarrow F' = 5$.

6. Mixtures of the above configurations at various powers and detunings.

None of the above produced a $F = 4 \rightarrow F' = 5$ MOT. To explain these results, we can make estimations of the cooling done with population rate equations. For a two level system, the rate of population transfer between the ground state P_g and the excited state P_e is

$$\frac{dP_e}{dt} = -\gamma P_e - \frac{\frac{|\Omega|^2}{\gamma}}{1 + \frac{4\Delta^2}{\gamma^2}}(P_e - P_g), \tag{3.7}$$

$$\frac{dP_g}{dt} = \gamma P_e + \frac{\frac{|\Omega|^2}{\gamma}}{1 + \frac{4\Delta^2}{\gamma^2}}(P_e - P_g). \tag{3.8}$$

Here, γ is the strength of the transition, Δ is the detuning from the transition, and Ω is the Rabi flopping frequency of the transition. This can be generalized to a system with multiple ground and excited states.

$$\frac{dP_{e,k}}{dt} = -\gamma P_{e,k} - \sum_{j=1}^{N_g} \frac{\frac{|\Omega_{jk}|^2}{\gamma}}{1 + \frac{4\Delta^2}{\gamma^2}}(P_{e,k} - P_{g,j}), \qquad k = 1...N_e \tag{3.9}$$

$$\frac{dP_{g,j}}{dt} = \gamma \sum_{k=1}^{N_e} b_{jk} P_{e,k} + \sum_{k=1}^{N_e} \frac{\frac{|\Omega_{jk}|^2}{\gamma}}{1 + \frac{4\Delta^2}{\gamma^2}}(P_{e,k} - P_{g,j}), \qquad j = 1...N_g \tag{3.10}$$

$$b_{jk} = \frac{|\langle g,j|r_{m_j - m_k}|e,k\rangle|^2}{\sum_j |\langle g,j|r_{m_j - m_k}|e,k\rangle|^2} \tag{3.11}$$

where b_{jk} is the branching fraction of the decay from the excited state to a particular ground state. The Rabi flopping frequency is proportional to the dipole matrix element d and the electric field of the driving light ϵ so that $\Omega = d\epsilon/\sqrt{3}\hbar$ for unpolarized MOT light. In the $|F, m_F\rangle$ basis our dipole matrix element is given by

$$d = e\frac{\langle F, m_F||r||F', m'_F\rangle}{\sqrt{2F'+1}} C^{F',m'_F}_{Fm_F1q} \tag{3.12}$$

$$\langle F, m_F||r||F', m'_F\rangle = (-1)^{F+J+I+1}\sqrt{\frac{3\pi\gamma\epsilon_0\hbar c^3(2J'+1)}{\omega_0^3 e^2}}\sqrt{(2F'+1)(2F+1)}\begin{pmatrix} J & I & F \\ F' & 1 & J' \end{pmatrix} \tag{3.13}$$

where J is the total electronic angular momentum of the atom and I is the nuclear spin. ω_0 is the energy separation between the two states. The symbol on the far right in parentheses is the Wigner Three-J symbol.

We can solve these equations numerically for $F = 4, 5, 6$, $F' = 5$, $J = 15/2$, $J' = 17/2$ as is suitable for holmium. We select reasonable, optimistic parameters for a retroflected MOT by setting each beam power as $P_{4\to5} = 200$ mW,$P_{5\to5} = 60$ mW,$P_{6\to5} = 20$ mW in a 1 mm waist MOT beam. We set the detuning to the linewidth γ. We find a steady-state population of $P_{F=4} = 21\%$, $P_{F=5} = 24\%$, $P_{F=6} = 32\%$, $P_{F'=5} = 23\%$ (Table 3.1). This readily explains the difficulties that we have encountered. The transition strength of $F = 4 \to F' = 5$ is 40.6% that of $F = 11 \to F' = 12$ [51], decreasing the efficiency of the cooling proportionately. In addition, the atoms only spend 43% of their time in the cooling cycle $F = 4 \to F' = 5$ at all. Ideally, we would want this to be 100 %. Our slowing beam is similarly reduced in effectiveness due to reduced scattering rates on the $F = 5 \to F' = 5$ and $F = 6 \to F' = 5$ transitions, reducing our available slowed trapping population despite using about 40% more coupled hyperfine states. This combination shows that our reasonable parameters will probably not cool atoms into a MOT.

We can try other parameters, such as simulating the main beam repumping the $F = 6 \to F' = 5$ line and allowing the weaker sidebands to form our other beams. The $F = 5 \to F' = 5$ beam is particularly weak because it relies on modulation by both EOMs. We use powers of $P_{4\to5} = 20$ mW,$P_{5\to5} = 6$ mW,$P_{6\to5} = 200$ mW and achieve $P_{F=4} = 31\%$, $P_{F=5} = 31\%$, $P_{F=6} = 21\%$, $P_{F'=5} = 18\%$. The time an atom spent in the cooling cycle would be about 48%.

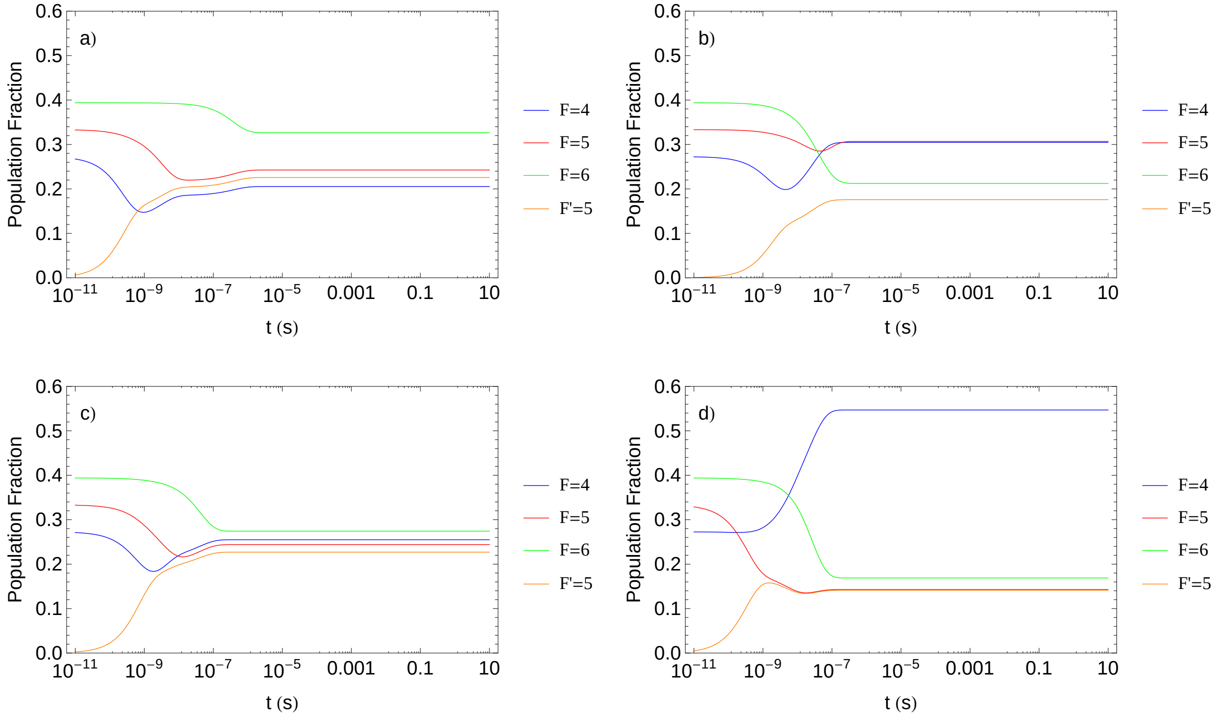

Table 3.1 Calculated state dynamics in four cases. a) Using reasonable powers achievable with our experimental power limitations. b) Also reasonable, with the strong beam on the $F = 6 \to F' = 5$ repumper. c) What we could achieve with b) if we used another high-efficiency EOM. d) Powers that are not experimentally feasible.

If we used EOMs at their maximum efficiency tuned to allow us to modulate that beam on $F = 5 \to F' = 5$ directly, we could set our powers to $P_{4\to5} = 60$ mW,$P_{5\to5} = 60$ mW,$P_{6\to5} = 200$ mW and achieve $P_{F=4}26\%$, $P_{F=5} = 24\%$, $P_{F=6}27\%$, $P_{F'=5} = 23\%$. This is hardly better than in the previous case.

The only case that we found that produces reasonable amounts of time in the cooling cycle is when we set the $F = 4 \to F' = 5$ power very low, i.e. $P_{4\to5} = 6$ mW,$P_{5\to5} = 400$ mW,$P_{6\to5} = 400$ mW. In this case, we still find that only 69% of the atoms are in the cooling cycle. Not only are the repumper powers not achievable, but the cooling light then is very weak and would have a very low capture velocity. The time spent in the cooling cycle increases with lower $F = 4 \to F' = 5$, but this is still counterproductive given that the light is already too weak to trap with. It is perhaps feasible to make such a MOT with the addition of a Zeeman slower to slow a large number of atoms down to the capture velocity at these low powers.

In conclusion, the $F = 4 \to F' = 5$ MOT is not experimentally feasible given our setup.

3.3 Narrow-Line MOTs

It is possible to improve loading and collisional rates in an optical dipole trap by reducing the MOT temperature. This can be done by further red detuning the MOT from its cooling transition or by switching to a cooling transition with a more narrow linewidth. Using weaker transitions are by far the more effective of the two techniques. There is definitely no shortage of possible transitions available to rare earths but selecting suitable transitions can require some care. For example, a lower scattering rate reduces the restoring force provided by the cooling photons. For transitions that have linewidths of a few tens or hundreds of kHz this is not typically a problem and a MOT can be created normally. However, in the regime of $\Delta\nu\sim1$ kHz gravity and magnetic effects compete directly with the restoring force and can create catastrophic instabilities in the MOT[46].

Recently, narrow-line MOTs in rare earths have been achieved [46, 65, 38, 43, 44]. Two of these have been made with extremely narrow $\sim$1 kHz cooling transitions and have succeeded in producing very low temperature MOTs of order 1 μK[46, 38]. While these are still several orders of magnitude larger than their Doppler temperature, they are still colder than the MOTs made on the broad cooling lines that are cooled to, at best, 20 μK. Fundamentally, their temperature is limited by the recoil velocity where the thermal energy of the atoms equals the momentum transfer of the absorption and emission of a photon. The recoil temperature for an atom cooled by photons with momentum k is given by

$$T_R = \frac{(\hbar k)^2}{2mk_B}. \tag{3.14}$$

These extremely narrow line MOTs operate by balancing the optical, magnetic, and gravitational forces at a place along the magnetic quadrupole field where the magnetic field is non-zero. They use blue-detuned beams to cool, which are shifted to red-detuned from the transitions due to Zeeman shifts.

Element	Cooling Line	λ (nm)	$\frac{A}{2\pi}$ (MHz)	T_D(μK)	T_R (nK)
Dy	$4f^{10}6s^2 \rightarrow 4f^9 5d6s^2$	741	0.0018	0.04 [38]	107
Ho	$4f^{11}6s^2 \rightarrow 4f^{10}(^5I_7)5d_{5/2}6s^2$	608	0.038	0.91	157
Ho	$4f^{11}6s^2 \rightarrow 4f^{11}6s6p(^3P_1)$	599	0.15	3.5	162
Ho	$4f^{11}6s^2 \rightarrow 4f^{11}6s6p(^3P_2)$	426	1.59	38	320
Ho	$4f^{11}6s^2 \rightarrow 4f^{10}(^5I)5d^26s$	412	2.3	780	342
Er	$4f^{12}6s^2 \rightarrow 4f^{12}6s6p(^3P_1)$	583	0.19	4.5 [32]	169
Er	$4f^{12}6s^2 \rightarrow 4f^{12}5d_{5/2}6s^2$	841	0.008	0.19 [46]	81
Tm	$4f^{13}6s^2 \rightarrow 4f^{12}5d_{3/2}6s^2$	530.7	0.35	8.4 [43]	202
Yb	$6s^2 \rightarrow 6s6p(^3P_1)$	556	0.182	4.4 [44]	179

Table 3.2 Narrow Line MOTs that have been made with rare earths. The transitions for Ho are only for comparison; none have been attempted.

The spectrum of holmium is very dense and we have identified several cooling lines that would be appropriate for a MOT (Labeled 1-9 in Fig. 3.1). Several of these have been measured experimentally and their linewidths obtained[1] but the rest have unknown linewidths. They may very well be of interest for very cold narrow-line MOTs. In table 3.2 we compare these lines to those used in other rare earths to obtain narrow-line MOTs. To obtain estimates for what their linewidths may be, we can perform numerical simulations with the Cowan Code.

3.3.1 The Cowan Code

The Cowan Code is a semi-empirical method for predicting transitions and their linewidths based on a relativistic Hartree-Fock method. The full details of the code are based on the methods found in [66]. It is split into four separate programs.

1. The first program calculates the one-electron radial wavefunctions for specified electron configurations using Hartree-Fock. These radial wavefunctions are used as input for the second program.

2. The second program calculates configuration-interaction Coulomb integrals for pairs of interacting configurations. It also calculates electric dipole and quadrupole interactions. These calculations are the input of the third program.

3. The third program creates energy matrices for each value of J. It diagonalizes the matrix to find the energy eigenstates for each configuration. It calculates several important features of these states, including the magnetic dipole, electric quadrupole, and the radiation spectra. The information contained in the spectra includes wavelengths, oscillator strengths, radiation transition probabilities, and radiative lifetimes. We are most interested in the oscillator strengths of the transitions whose wavelengths are already known.

4. The final program allows the user to input experimental data. The experimental data is then used to make a least squares fit that is minimized by an iterative procedure. This program thereby produces higher accuracy results. We used the experimental data found in [1] to refine and compare our results.

The Cowan Code is useful for calculating extremely complex spectra and has been used with some success for atomic structure calculations in singly ionized lanthanides [67]. We have applied it to the calculation of the structure of neutral holmium[1].

The results of our calculations are shown in Table 3.3. It provides a sampling of solutions output from the program of couplings to the ground state $4f^{11}6s^2$ and to the excited states $4f^{11}6s6p$ and $4f^{10}5d6s^2$. The table shows that for the transitions we are most interested in that have already been measured, the Cowan Code produces very reliable results. There are some discrepancies towards higher energies. This may be due to the least squares fit approaching its limits near the edges of the available experimental data. We have predicted the linewidths of several narrow transitions that are interesting for cooling Ho atoms. The 660.9 nm transition could potentially be just broad enough to provide enough radiation pressure to trap without resorting to complicated experimental setups. Failing that, the 608 nm line is very attractive.

---

[1] I would like to thank Alexander Kramida of the National Institute of Standards and Technology, Gaithersburg for useful discussion and for providing a readily compiled source of this code.

Transition[68]	Label	λ (nm)	J	Meas. $\Delta\nu(10^6\frac{1}{\mathrm{s}})$	Cowan $\Delta\nu(10^6\frac{1}{\mathrm{s}})$
$4f^{11}6s^2 \rightarrow 4f^{11}(^4I^{\circ}_{15/2})6s6p(^1P^{\circ}_1)$	9	410.4	17/2	204	-
$4f^{11}6s^2 \rightarrow 4f^{10}(^5I)5d^2(^3P)(^7H)6s$	8	412.1	17/2	14.5	-
$4f^{11}6s^2 \rightarrow 4f^{11}(^4I^{\circ}_{13/2})6s6p(^3P^{\circ}_2)$	7	425.6	17/2	10	0.27
$4f^{11}6s^2 \rightarrow 4f^{10}(^5I_6)5d_{5/2}6s^2$		493	13/2	2.15	2.49
$4f^{11}6s^2 \rightarrow 4f^{10}(^5I_6)5d_{5/2}6s^2$		497	15/2	1.11	1.11
$4f^{11}6s^2 \rightarrow 4f^{11}(^4I^{\circ})5d6s^2(^3D)$		530	13/2	0.27	0.26
$4f^{11}6s^2 \rightarrow 4f^{11}(^4I^{\circ}_{15/2})6s6p(^3P^{\circ}_2)$	6	545.3	17/2	-	0.0066
$4f^{11}6s^2 \rightarrow 4f^{11}(^4I^{\circ}_{15/2})6s6p(^3P^{\circ}_1)$		586	13/2	0.65	0.66
$4f^{11}6s^2 \rightarrow 4f^{11}(^4I^{\circ}_{15/2})6s6p(^3P^{\circ}_1)$		592	15/2	0.36	0.34
$4f^{11}6s^2 \rightarrow 4f^{11}(^4I^{\circ}_{15/2})6s6p(^3P^{\circ}_1)$	5	598.3	17/2	0.92	0.96
$4f^{10}(^5I_8)5d_{5/2}6s^2 \rightarrow 4f^{10}(^5I)5d6s6p?$		598.5	19/2	0.06	0.06
$4f^{11}6s^2 \rightarrow 4f^{10}(^5I_7)5d_{5/2}6s^2$	4	608	17/2	0.25	0.11
$4f^{11}6s^2 \rightarrow 4f^{10}(^5I_7)5d_{3/2}6s^2$	3	660.9	17/2	-	0.023
$4f^{11}6s^2 \rightarrow 4f^{10}(^5I_8)5d_{5/2}6s^2$	2	867.3	17/2	-	0.006
$4f^{11}6s^2 \rightarrow 4f^{10}(^5I_8)5d_{3/2}6s^2$	1	1193	17/2	-	<0.001

Table 3.3 Listing of linewidths for several transitions in Ho. All linewidth data in column 5 comes from [1]. The results of the Cowan Code are shown in column 6.

3.4 Conclusion

In this chapter, we have provided documentation of the creation of the first holmium MOT. We used a very broad cooling line without a Zeeman slower. This MOT is the foundation for the rest of our future experiments. In addition, we have discussed more exotic MOTs. We attempted to make a MOT on the $F = 4 \rightarrow F' = 5$ lines of our cooling transition and demonstrated that this is very technically difficult. We also considered the details of making a narrow-line MOT for cooling to lower atom temperatures using the Cowan code.

Chapter 4

Rydberg Spectroscopy

4.1 Introduction

For quantum information processing with Rydberg atoms, knowledge of the Rydberg levels is important for accurate prediction of the dipole-dipole interaction strengths and sensitivity to electric fields. Studies of the Rydberg spectra of neutral rare-earth elements have been limited to date, with initial measurements of the ionization potentials for the full ranges of lanthanides [69] and actinides [70] and energy-resolved Rydberg states for La[71], Eu[72], Dy[73], Lu[74], Gd[75], Sm[76], Th[77], Ce[78], Yb[79], Ac[80], Pu[81], and U[82].

With regards to Ho specifically, there have been no energy resolved Rydberg state measurements done. The ionization potential has been measured as 48562(5) cm^{-1}[69] . In addition, theoretical work has been done [3] to estimate the quantum defects for the first 102 elements for the Rydberg s, p, d, and f states in the high-n limit. However, no exact values are provided. With these calculations and the relatively large errors bars on the ionization potential, these values do not provide an spectroscopically useful estimation of holmium's Rydberg structure. These measurements do show that Ho can be ionized through a two-photon transition of our MOT light at 410.45 nm and a second beam at 413 nm. This allows us to use the same optics for both the MOT and Rydberg second-photon and reduces the Doppler broadening of the two-photon transition.

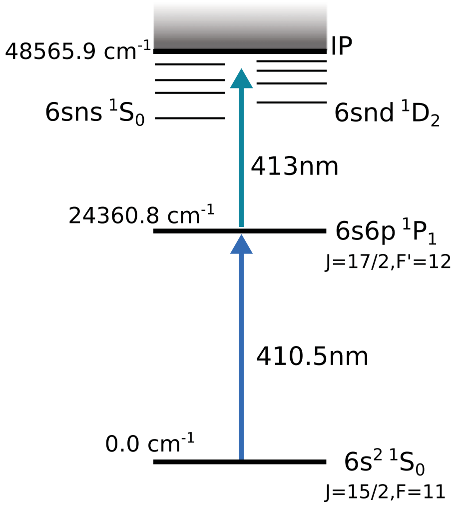

Figure 4.1 Two-photon transition to the holmium Rydberg states. The first photon is provided by the MOT beams. The second is provided by a second laser tuned only a few nanometers from the first.

4.2 Experimental Setup

4.2.1 Field Ionization

Typical Rydberg spectrum measurements are measured through ionization of trapped atoms. Rydberg atoms are produced either collisionally or optically and then are subjected to a strong electric field. Because of its weak binding energy to their parent nucleus, a Rydberg atom excited to level n can then be ionized by an electric field of [83]

$$E = \frac{1}{16n^4} \tag{4.1}$$

The ionized atoms are accelerated by the ionizing field towards a detector plate. The detector plate will count the number of Rydberg atoms produced with a large enough n to be ionized by the plate. This technique is inefficient, cumbersome, expensive, and would require significant changes to our experimental setup. We instead use a MOT depletion spectroscopy technique.

4.2.2 MOT Depletion Spectroscopy

The MOT depletion spectroscopy method is used to determine resonant transitions to Rydberg states by monitoring the steady state atomic fluorescence signal of the MOT while a second, overlapping Rydberg beam is scanned over a large frequency range. The MOT beams provide the first photon in a two-photon transition to a Rydberg state; the Rydberg beam at 413 nm provides the second. Atoms excited to the Rydberg state are then lost from the MOT, decreasing the fluorescence signal and giving a direct signature of the resonant transition energies. These population drops can be attributed to a number of things: the Rydberg atom could ionize, the Rydberg atom could decay into a dark state, unbalanced forces on the MOT, etc.

To prepare for this technique, we monitor our MOT fluorescence through a 410 nm filter with a photodiode, model Thorlabs PDA36A. This model of photodiode is powered and has many selections for signal gain, the quietest being 40 dB. More sensitive measurement of the MOT fluorescence decreased the number of measurements needed to reduce the signal-to-noise measurements and sped up data collection, however, so the photodiode was typically operated at its maximum gain of 70 dB. To compensate for extra electronic noise in this mode, the signal was modulated by a chopper placed in front of the detector. The signal was then input a lock-in amplifier to suppress much of the background electronic noise. An Andor Luca-R camera was also used to ensure the presence of a MOT during data collection.

The Rydberg beam is provided by a frequency-doubled 826 nm diode described in chapter 2. This beam is coupled into a fiber and focused onto the MOT (Fig. 4.2). The beam after the fiber and optics was 3 mW focused to a waist of 27 μm. To align the beam with the MOT, nearly resonant light was picked off from the 0^{th} order of the MOT AOM and coupled into the fiber. This light had a detuning of +60 MHz (1.8 Γ) and a power of $\sim$ 50 mW. The fiber output was mounted on a multi-axis tilt platform that allowed us to finely position the beam for maximum disruption of the MOT by the resonant light. The +60 MHz light was then dumped by a flip mirror and the Rydberg light was aligned to the MOT.

The 826 nm fundamental light of the Rydberg beam was locked to a Fabry-Pérot reference cavity, described in chapter 2, and scanned across 1-2 GHz with a linear scan period of about 10

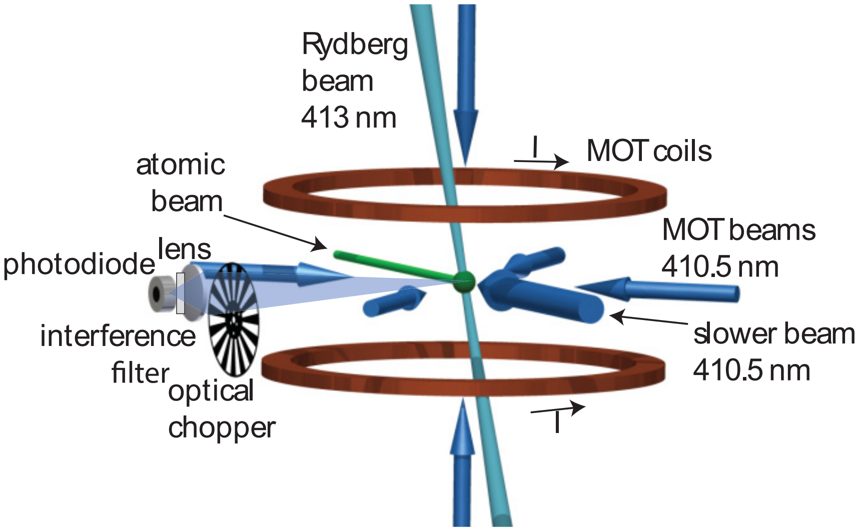

Figure 4.2 Experimental setup for MOT depletion spectroscopy. A focused Rydberg beam is overlapped with a Ho MOT, resulting in depletion of the equilibrium atom number on resonance.

s using a cavity piezo powered by a NI BNC-2090A. The Fabry-Pérot cavity uses a 10 cm long Invar spacer mounted inside a vacuum can temperature controlled to 0.01 C and PDH locked. This gives the laser a short-term linewidth of 200 kHz and a long-term drift of 8 MHz at 413 nm. As the MOT laser was locked to a ULE cavity with a short-term linewidth of $\sim$ 100 kHz and <1 MHz of long-term frequency drift, the combined frequency drift of the two lasers was dominated by the drift of the Invar cavity. The combined long-term drift was about 10 MHz, or 0.0003 cm^{-1}.

For each measurement, spectra are averaged over 50 repetitions. Increasing and decreasing frequency ramps of the 413 nm laser are compared to verify that resonances are actually observed as well as to account for any hysteresis of the frequency ramp. The high- and low-frequency endpoints of each scan were recorded using a wavemeter (HighFinesse WS-7) and the piezo voltage converted to a frequency using the linearity of the ramp. Typical MOT depletion was $\sim 10\%$. A sample spectrum is shown in Fig. 4.3.

As the wavemeter can drift by several hundred MHz day-to-day, each line found was calibrated to the MOT light. The energy of the MOT photons was well-known, referenced to an independent measurement of the center-of-gravity transition frequency from $4f^{11}6s^2$, $J = 15/2$ to $4f^{11}6s6p$,

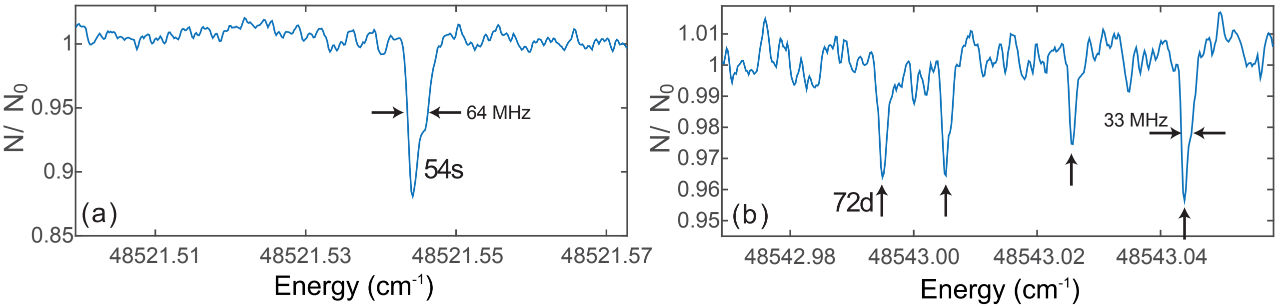

Figure 4.3 MOT Depletion spectra. (a) Isolated depletion line for the 54s state, resolved with a 60 MHz FWHM. (b) Multiple fine-structure states are resolved for the 72d series, with the lowest energy level used to determine the series parameters as it is typically the strongest resolved line for each n.

$J = 17/2$ obtained with a 1-m Fourier transform spectrometer calibrated against an argon line using the experimental setup described in [84]. This gives an energy of 24360.790(1) cm^{-1}, which is combined with precise measurements of the ground- [85, 86] and excited-state [29] hyperfine splittings to yield an absolute frequency of the MOT laser given by 730.31682(3) THz. This value is used to calibrate the wavemeter and measure the energy of the Rydberg photons, resulting in a total uncertainty of 200 MHz (0.007 cm^{-1}). Details of the energy calibration procedures are provided in the appendix C.

4.2.3 Results

Based on dipole selection rules, from the $4f^{11}6s6p, J = 17/2$ state it is possible to excite the atom to the $4f^{11}6sns$ and $4f^{11}6snd$ Rydberg states with a two-photon transition, with a total of 15 series possible. Eight of these series are triplet s- or d-states and assumed to be weak due to parity conservation. This leaves the $6sns(^1S_0), J = 15/2$ and $6snd_{5/2,3/2}(^1D_2), J = 15/2, 17/2, 19/2$ to be observed by the experiment.

The MOT depletion rate associated with a transition to state n is dependent upon the competing effect of reduced oscillator strength, which drops off with higher n, and increasing ionization rates and number of available dark states. Because of this, the absolute value of the depletion is a poor indicator of absolute transition strength; however, it does provide relative strengths for closely spaced fine-structure transitions. The number of fine-structure states resolved for the nd series varies between measurements due to the finite frequency range the second photon is scanned over, but for all data sets where the full range is included, 4 to 6 states are resolved, limited by the signal-to-noise ratio for the weaker transitions.

The energy levels E_n of the Rydberg series are described by the Rydberg-Ritz formula

$$E_n = E_{IP} - \frac{Ry}{[n - \delta(n)]^2} \tag{4.2}$$

where E_{IP} is the ionization potential, defined as the series limit as $n \to \infty$. $\delta(n)$ is the quantum defect for each series. For high-lying Rydberg states the quantum defect can be assumed to be independent of n, allowing extraction of a precision value for E_{IP} by fitting to the series convergence [87].

The initial few Rydberg states measured were found simply by tuning the Rydberg laser to $n \sim 60$, where the gaps between subsequent Rydberg states could be estimated to be about 30 GHz. After scanning through all frequencies in a block of several hundred GHz, several states were measured. To speed up data-taking, it was necessary to separate each state into its proper series and calculate its approximate $n - \delta$, allowing us to accurately predict where the next states would be. Using the measurement of the ionization potential found in [69] and plotting the energy of the Rydberg state versus its $n - \delta$ modulo 1, the states are easily identifiable into two series. These series can also be further specified by the presence of fine structure in the d-states and the lack of it in the s-states. With this information, it is possible to identify a pattern consistent with eq. 4.2 and scan the Rydberg laser over only those frequencies.

165 Rydberg levels have been identified in this way. For the d-series data, the series with the largest defect is typically the strongest line and has been observed across the full range of measured energies. For this reason, only this fine-structure state is used for analysis of the nd defect, as the remaining satellite states are insufficiently discriminated to clearly identify their corresponding series correctly. As the strongest dipole matrix elements are for transitions to $6snd_{5/2}(^1D_2)$,$J = 19/2$, this is the most probable state being analyzed, from which we infer an inverted fine structure in the nd series as is observed in the Ho II ionic ground state. The rest of the d-states measured are insufficiently discriminated to clearly identify their corresponding series correctly. Two additional

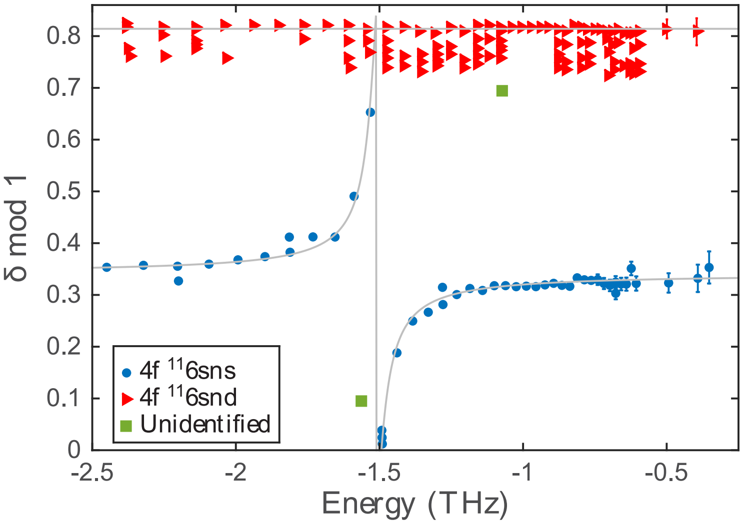

[t]

Figure 4.4 Fano plot of δ modulo 1 versus the energy of the Rydberg states. The quantum defect is constant for the d series (red triangles) and shows a perturbation at around $n = 51$ in the s series (blue circles). Green squares indicate Rydberg levels of unknown configuration. Missing fine-structure states on the nd series arise due to finite measurement ranges.

states which could not be assigned to either ns or nd series were observed at 48530.035(7) and 48513.837(7) cm^{-1}.

A Fano plot of $\delta(E)$ mod 1 is shown in Fig. 4.4. The d-series quantum defect is clearly very constant at throughout the entire range. The s-series is shown to have a large series perturbation. This perturbation prevents the data from being described with a single-channel quantum defect model, and instead multi-channel quantum defect theory (MQDT) applies [88]. In this framework, the perturbation can be treated as coupling between two near-resonant series, resulting in a modification of the quantum defect of [88, 80]

$$\delta(n) = \delta_0(n) - \frac{1}{\pi}\tan^{-1}\left(\frac{\Gamma/2}{E_n - E_j}\right) \tag{4.3}$$

where Γ is the spectral width and E_j the energy of the interloper. Interestingly, despite the perturbation occurring below the first ionization potential associated with the Ho II ground state, the bound-bound series interaction can have a large spectral width comparable to a bound-continuum autoionization resonance [89].

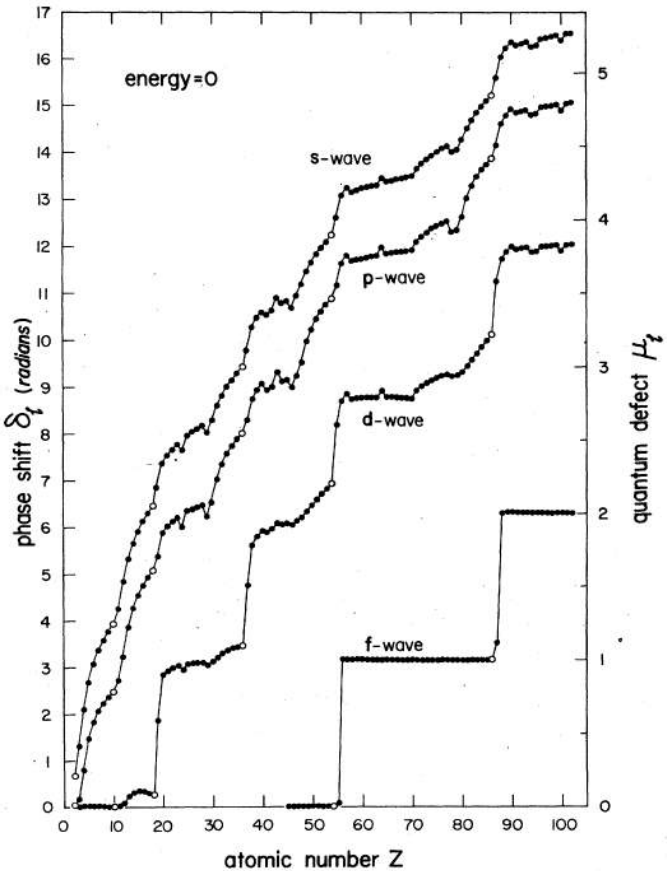

Figure 4.5 Asymptoptic quantum defects of the first four orbital angular momentum (l) states. Reproduced from [3].

The ionization potential and quantum defects are obtained using a least-squares fit to both the ns and strong nd series using eq. 4.2 and 4.3. The ionization potential is fit to $E_{IP} = 48565.910(3)$ cm^{-1}, with both series converging to the $4f^{11}(^4I^o_{15/2})6s_{1/2}$,$J = 8$ Ho II ground state. This represents an improvement of three orders of magnitude over previous measurements [87]. The fit yields asymptotic values of the quantum defect mod 1 δ_s mod $1 = 0.324(5)$ and δ_d mod $1 = 0.814(3)$. These values are in close agreement with those predicted by [3] and reproduced in Fig. 4.5, which predicts quantum defects of $\delta_s = \sim 4.3$ and $\delta_d = \sim 2.8$ for Ho. We therefore assume a full asymptotic quantum defect of $\delta_s = 4.324(5)$ and $\delta_d = 2.814$.

The fitted defect is shown in Fig. 4.4 which accurately reproduces the observed perturbations, resulting in parameters $\delta_0 = 4.341(2)$,$\Gamma = 6.9(3)$ GHz, and $E_j = 48515.47(4)$ cm^{-1}. The

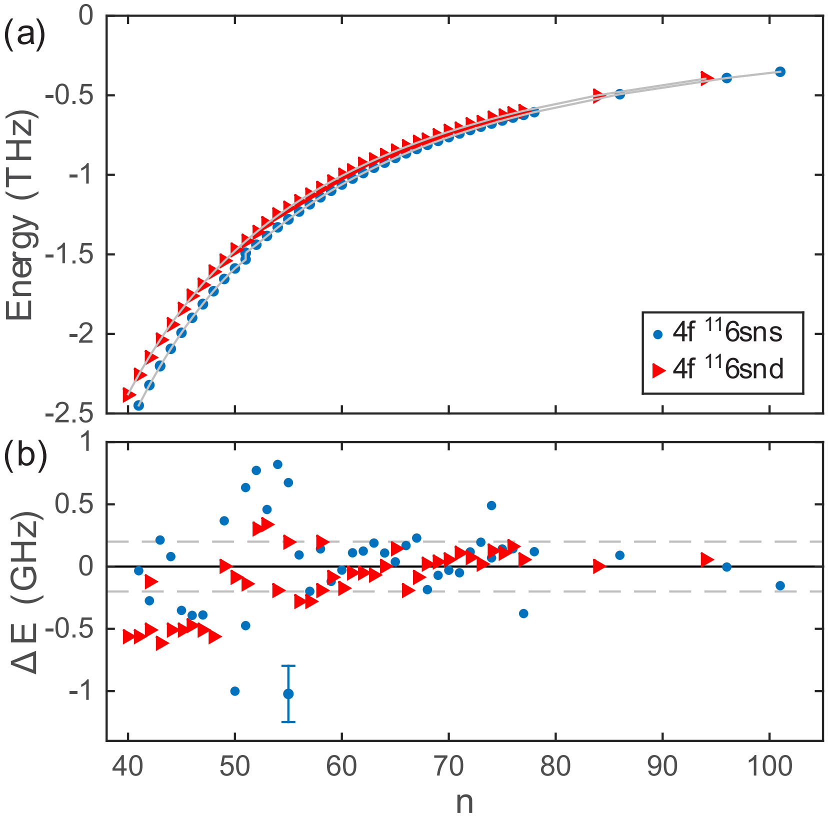

Figure 4.6 Rydberg state energy levels. (a) Measured energy levels for the ns and nd series, with solid lines calculated using fitted quantum defect parameters summarized in the text. (b) Fit residuals, yielding an RMS residual of 200 MHz for n >60 away from the 51s series perturbation, in good agreement with the 200-MHz uncertainty (indicated by the dashed gray lines and plotted as a representative error bar).

perturbing series is unknown, but likely it has the same $4f^{11}$ inner electronic configuration due to the strength of the interaction. Around this resonance the ns series is observed to split into doublets, resulting in four separate states being identified as $n = 51$ due to fine-structure splitting of the series interloper. Weak doublets are also observed for a few other s states (n=43,47,74) due either to much weaker interseries resonances or potential singlet-triplet mixing within the ns series. The mixing of these resonances with other states may offer substantially different properties (such as long lifetime if triplet in character). They may be interesting candidates for further study.

Figure 4.6 shows the spectrum of Rydberg states and demonstrates the fit to eq. 4.2. The resulting energy residuals from the ns and nd fits, with the exception of the increased error around the $51s$ series perturbation, results in an rms residual of 200 MHz for $n>60$. This is in good agreement with the 200 MHz uncertainty in determination of the absolute energy of the levels. Absolute energies and residuals for each state are given in the appendix, along with a precise description of the measurement of the absolute energies.

4.2.4 The Van der Waals Coefficient C_6 of Holmium

One of the main advantages of neutral atoms in quantum computing is their switchable interaction strength that allows them protection from decoherence while in a ground state but provides a mechanism for entanglement interactions at Rydberg scales. The interaction between two atoms separated by a distance R can be expanded as an infinite sum [90], e.g.

$$V(R) = -\sum_{n=1}^{\infty} \frac{C_n}{R^n} \tag{4.4}$$

The first two coefficients C_1 and C_2 correspond to the Coulomb and charge-dipole interaction respectively. For neutral atoms at large distances they are neglected. The C_3 coefficient corresponds to the dipole-dipole interaction. This effect is strong enough to mix electronic states and creates a dipole-dipole interaction even though the unperturbed eigenstates have no permanent dipole moment. If two Rydberg atoms are both excited to level nl, they are mixed with their dipole-allowed states $n_s l_s$ and $n_t l_t$. At large distances, the dipole-dipole interaction decays as $1/R^6$, giving rise to the C_6 coefficient [91]

$$V(R) = \frac{C_6}{R^6} \tag{4.5a}$$

$$C_6 = D_\psi \sum_{n_s n_t} \frac{e^4}{-\delta_{st}} (R_{nl}^{n_s l_s} R_{nl}^{n_t l_t})^2. \tag{4.5b}$$

In these equations, C_6 is the sum of the dipole matrix elements over the allowed dipole transitions from state nl divided by their respective Förster defects δ_{st}. The Förster defect is defined by energy defect between the state nl and the channels n_s and n_t. This is weighted by the coefficient D_ψ which contains all of the angular momentum properties for the states. For $l = 0$, D is 4/3 [91].

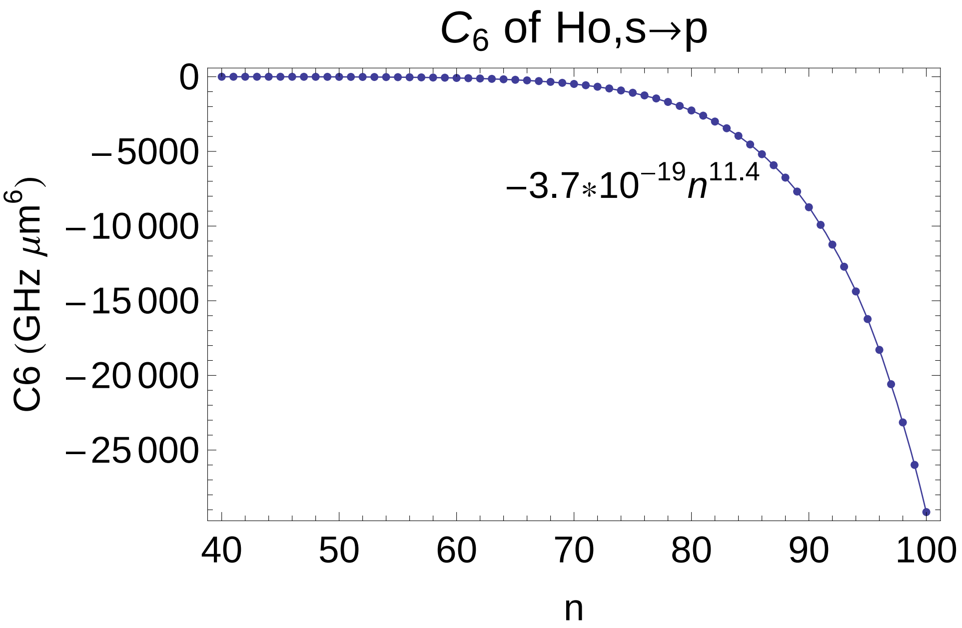

Figure 4.7 Estimated C_6 coefficients for holmium in an ns state.

We can obtain δ_{st} with knowledge of the quantum defects δ of an atom in angular momentum state l. We have discussed in the previous sections the measurement of δ for $l = 0, 2$ and found them in very close agreement with the theoretical values predicted by Fano. If we allow the assumption that Fano's calculations $\delta_{l=1} = 3.78$ [3] are also sound, we can provide a rough estimate of δ_{st} for the ns state.

This assumption also aids the calculation of $R_{nl}^{n_s l_s}$ and $R_{nl}^{n_t l_t}$. There are no closed form analytical results for atoms with non-zero quantum defects and the matrix elements must be computed numerically. There are many methods of doing this, but most are susceptible to numerical instabilities or are computationally expensive. A good compromise is to use a WKB approximation that agrees to within one percent of direct numerical integration of quantum defect wavefunctions [92]

$$
\begin{aligned}
R_{nl}^{n_s l_s} = -1^{n_s - n} \frac{\gamma_c^5}{(\gamma\gamma_s)^{3/2}(\gamma_s - \gamma)} \times \Big[\frac{1-y}{\pi} \sin[\pi(\gamma_s - \gamma)] + J'_{\gamma-\gamma_s}[y(\gamma_s - \gamma)]\Big] \\
\pm\sqrt{y^{-2} - 1}(J_{\gamma-\gamma_s}[y(\gamma_s - \gamma) - \frac{\sin[\pi(\gamma_s - \gamma)]}{\pi(\gamma_s - \gamma)}])]
\end{aligned}
\tag{4.6}
$$

where $y = [1-((l+l_s+1)/(2\gamma_c))^2]^{1/2}$, $\gamma_c^3 = 2(\gamma\gamma_s)^2/(\gamma+\gamma_s)$, and $\gamma = n-\delta$. The functions $J_\gamma(z)$ are the Anger functions defined as

$$J_\gamma(z) = \frac{1}{\pi}\int_0^\pi d\theta \cos(\gamma\theta - z\sin(\theta)) \tag{4.7a}$$

$$J'_\gamma(z) = \frac{dJ_\gamma(z)}{dz} = \frac{1}{\pi}\int_0^\pi d\theta \cos(\gamma\theta - z\sin(\theta)). \tag{4.7b}$$

Putting all of this together, we determine C_6 coefficients summarized in Fig. 4.7. The coefficient fits well to a fit to $n^{11.4}$. In most cases, the asymptotic scaling of C_6 goes as n^{11}. This can easily be seen in eq. 4.5b. The radial matrix elements of Rydberg atoms are each proportional to n^2. The Förster defect should scale as n^{-3} like the energy difference between adjacent Rydberg states. These effects combine to give the C_6 coefficient a n^{11} scaling[18]. Our fit to $n^{11.4}$ is therefore compatible with Rydberg scaling laws.

For a holmium atom at a distance of 5 μm from a Rydberg-excited holmium atom with $n = 100$, we estimate the energy level shift of the same $n = 100$ state to be -1.8 GHz. This compares nicely to alkalis (e.g. $C_{6,Rb}(n = 100) = 54500$ GHz μm^6 with an energy level shift of 3.6 GHz at 5 μm, and $C_{6,Rb}(n = 100) = 41250$ GHz μm^6 with an energy level shift of 2.6 GHz at 5 μm)[90].

4.2.5 Additional Results

Above the ionization potential, we observe a strong autoionization resonance at 48567.958(1) cm^{-1} with FWHM 9(1) GHz (Fig. 4.8). This lies 60 GHz above the ionization potential and thus is not an excitation to the J=7 fine-structure state of the ionic core which lies 637 cm^{-1} above E_{IP} [93].

Alongside the depletion resonances, a strong enhancement feature was observed resulting in up to an 80% increase in the MOT atom number at $\nu = 724.2662(2)$ THz, as shown in Fig. 4.9. The two enhancement features have a FHWM of 600 MHz and are spaced by 9.47(1) GHz, consistent with transitions between different hyperfine states. Enhancement of the MOT arises due to repumping population either from uncoupled ground-state hyperfine levels or long-lived metastable excited states back into the F=11 ground state which is cooled in the MOT. The peak

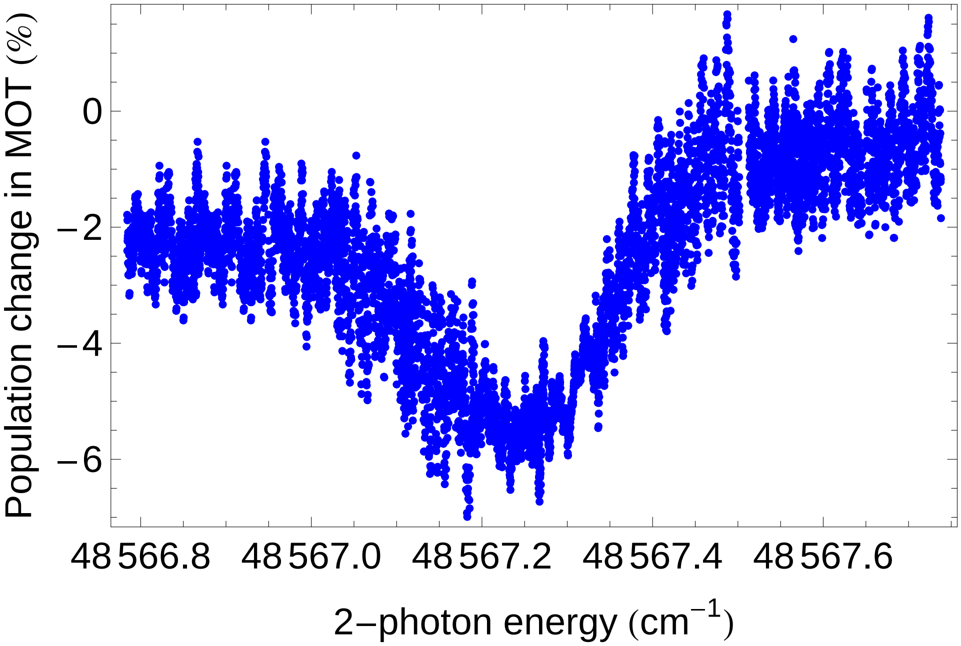

Figure 4.8 MOT depletion at an autoionization resonance 60 GHz about the ionization potential of Ho.

enhancement wavelength is independent of the MOT detuning, verifying that this effect arises from a single photon repump transition which can be exploited to create large atomic samples. The closest matching transition from published line data is from $4f^{10}(^5I_8)5d_{5/2}6s^2$,J = 17/2 ($E = 11530.56\ \mathrm{cm}^{-1}$) to $4f^{10}5d6s6p$,J = 17/2 ($E = 35692.30\ \mathrm{cm}^{-1}$) [94], which has a frequency of 724.350 THz, within 10 GHz of the measured resonance.

4.3 Conclusion

In this chapter, we presented experimental data describing the Rydberg energy levels of holmium. This is the first time these levels have been described with enough precision to allow controlled transitions to these states. We were able to extrapolate the quantum defects of the s and d levels and reduced the error in holmium's ionization potential by three orders of magnitude. We also found several unexpected spectral features, such as an autoionizing resonance, a MOT repumping line, and a series interaction in the s series. We used our results to predict the C_6 factor of holmium

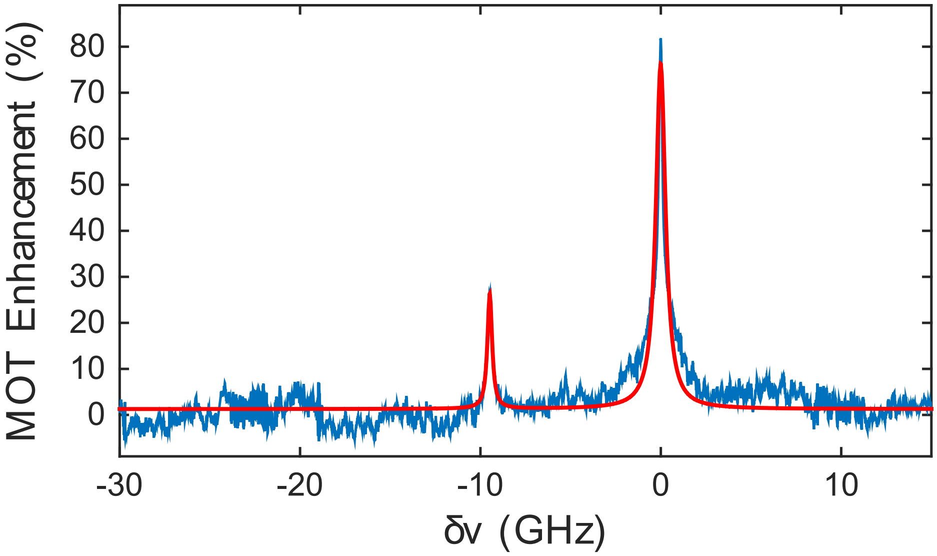

Figure 4.9 Enhancement of the MOT number as a function of detuning from ν = 724.2662(2) THz due to repumping population from a long-lived metastable state back to the ground-state cooling cycle, with a resolved hyperfine splitting of 9.47(1) GHz.

for the s series. This information will be used in the future to perform quantum gate operations via the Rydberg blockade.

Chapter 5

Dipole Trapping of Holmium

5.1 Introduction

Cooling the holmium ensemble into an optical dipole trap (ODT) is the next step towards performing coherent operations on the ensemble. These traps are based on the electrical dipole interaction an atom with an AC electric field[95]. A very intense, far off-resonant light field can produce a trapping potential in polarizable neutral atoms. This potential is conservative and generally very shallow ($\sim$1 mK), so it requires external cooling by light several linewidths from resonance to successfully fill the trap with atoms. As a rule of thumb, atoms in such a trap generally need to be pre-cooled to temperatures an order of magnitude lower than the trap depth. Because far off-resonant light is used for the ODT light, scattering from the light is negligible and extremely low temperatures can be maintained in the sample. This technique is powerful and versatile in its ability to create complex patterns of trapping potentials through interference effects and so has become a commonly used tool in cold atom physics. Energy level shifts are often comparable for all of the internal ground states of the atoms, distinguishing it from other trapping schemes such as the use of a MOT or magnetic trapping that provide very state-dependent confinement. This property is important for our experiment because we aim to take advantage of all of the hyperfine ground states of holmium. Assuming that a single ensemble utilizing all the hyperfine states can be made, calculations have shown the possibility to create an array of neutral holmium ensembles in an ODT lattice potential containing up to 1000 qubits [18].

The energy shift of an optical trap U is given by

$$U = -\frac{1}{4}\alpha(\omega)|\varepsilon|^2 \tag{5.1}$$

where α is the atomic polarizability and ε is the magnitude of the electric field. α is a term in the real domain containing scalar, vector, and tensor components that each interact with the electric field in a different way. It can be positive or negative depending on the detuning of ω from strong transitions. In a simplified model of a two-level system, red detuning from the transition produces a positive α and an attractive potential, drawing the atoms to regions of high intensity of the ODT laser. Blue detuning produces a negative α and a repulsive potential, pushing the atoms into areas of low laser intensity.

We focus on creating an attractive potential with a red-detuned ODT. This trap has the undesirable effect of shifting the atomic energy levels away from resonance with cooling and imaging light. This shift is not only inconvenient for imaging and cooling but can producing a dephasing effect if there are time-dependent intensity variations in the trapping beam. Another issue is that because the atoms are attracted to the regions of highest intensity, scattering and heating from the ODT beam is increased. Despite its drawbacks, we choose this because of its simple trapping geometry of a single focused beam. It is possible to build an ODT out of blue-detuned beams that trap at an intensity minimum and avoid these effects but these traps generally have very complicated optical setups [96, 97, 98]. After a red detuned trap has been demonstrated, we may switch to a blue-detuned trap to fully exploit its advantages.

5.2 Estimation of Ho Polarizability

Optical traps have been demonstrated in several other rare earths [33, 65, 99], indicating that similar traps should be possible in holmium. A significant challenge to making any ODT with holmium is that the AC polarizability of holmium is unmeasured and so trap depths are difficult to predict. The AC polarizability can be estimated by rewriting the energy shift for an x-polarized AC electric field with frequency ω detuned by from an electric dipole transition ω_{ba} between an excited state b and ground state a in its second order perturbation theory form.

$$U = -\frac{e^2}{2\hbar}\frac{\omega_{ba}}{\omega_{ba}^2 - \omega^2}|\langle\psi_b|x|\psi_a\rangle|^2|\varepsilon|^2 \tag{5.2}$$

Setting this equal to eq. 5.1 allows the static, vector, and tensor polarizabilities α_0,α_1, and α_2 of an atom to be found to be the sum of contributions from its dipole allowed transitions.

$$\alpha_0 = \frac{e^2}{m_e}\sum_b \frac{1}{\omega_{ba}^2 - \omega^2}\overline{f}_{ba} \tag{5.3a}$$

$$\alpha_1 = \frac{e^2}{2m_e}\left(\frac{6}{(j_a+1)j_a}\right)^{1/2}\sum_b(-1)^{j_a+b}\begin{Bmatrix} j_a & 1 & j_b \\ 1 & j_a & 1 \end{Bmatrix}\frac{\overline{f}}{\omega_{ba}^2 - \omega^2}\frac{\omega}{\omega_{ba}} \tag{5.3b}$$

$$\alpha_2 = \frac{3e^2}{2m_e}\left(\frac{40(2j_a-1)j_a)}{3(2j_a+3)(j_a+1)}\right)^{1/2}\sum_b(-1)^{j_a+b}\begin{Bmatrix} j_a & 1 & j_b \\ 1 & j_a & 2 \end{Bmatrix}\frac{\overline{f}}{\omega_{ba}^2 - \omega^2} \tag{5.3c}$$

$$\overline{f}_{ba} = \frac{2m_e\omega_{ba}}{3\hbar(2j_a+1)}|\langle n_b j_b||r||n_a j_a\rangle|^2 \tag{5.3d}$$

where $\overline{f}_{ba}$ represents the rotationally averaged oscillator strength from state $|n_a j_a\rangle$ to $|n_b j_b\rangle$. This is a particularly convenient way of expressing the polarizability because spectroscopic data frequently records the oscillator strength as $\log_{10}(gf)$, where $g = 2j_a + 1$ is the lower level degeneracy and $f = \overline{f}_{ba}$.

Fig. 5.1 shows the estimate of the polarizability based on the available experimental data found in [1] and recorded in appendix D. At the DC limit $\omega \to 0$ the static polarizability α_0 goes to 20.2 Å, in agreement with experimental observation [100] and previous theoretical work [101, 102] and summarized in Table 5.1. The tensor polarizability goes to -0.28 Å, which is also close to the experimentally determined value [103]. We note that the vector polarizability is 0 in this limit. The energy shifts of the atom for each component of the polarizability are given by the formulas

$$\Delta U_0 = -\frac{|\varepsilon|^2}{4}\alpha_0 \tag{5.4}$$

$$\Delta U_1 = -\frac{|\varepsilon|^2}{4}qm_j\alpha_1 \tag{5.5}$$

$$\Delta U_2 = \frac{|\varepsilon|^2 - 3|\varepsilon_x|^2}{8}\frac{3m_j^2 - j_a(j_a+1)}{j_a(2j_a-1)}\alpha_2 \tag{5.6}$$

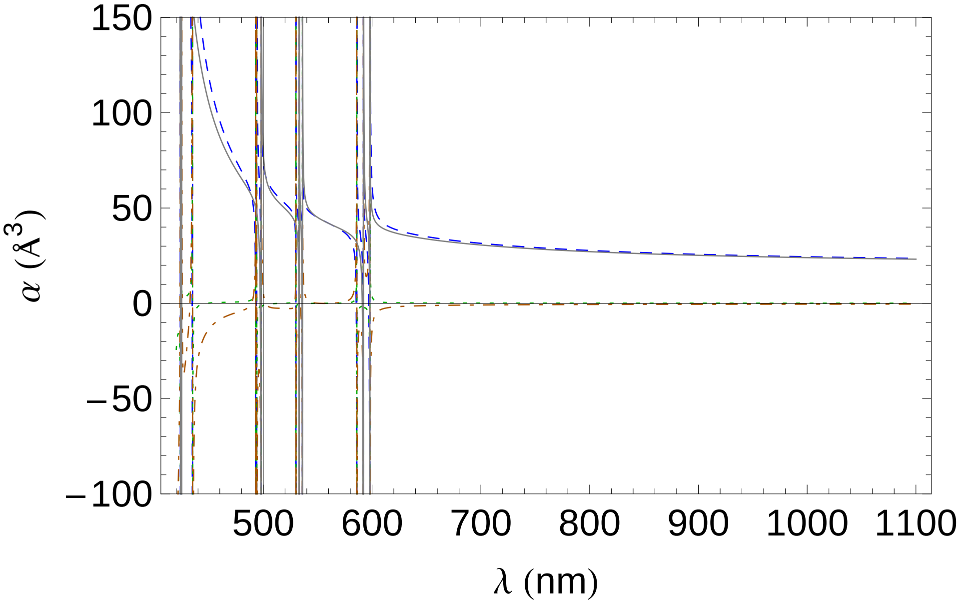

Figure 5.1 The static α_0 (blue dashed), vector α_1 (green dotted), tensor α_2 (orange dot-dashed), and total $\alpha_0 + \alpha_2$ (gray) polarizability of holmium estimated using the sum-over-states method. α_1 is much smaller than α_0 and α_2.

where $q = -1, 0, 1$ represents the index of our rank-1 vector. We note that for linearly x-polarized light (i.e. $q = 0$, $|\varepsilon| = |\varepsilon_x|$,$m_j = j_a$), the total shift is given by

$$\Delta U = -\frac{|\varepsilon|^2}{4}(\alpha_0 + \alpha_2). \tag{5.7}$$

For this reason, in Fig. 5.1 we also show the sum $\alpha_0 + \alpha_2$ to give a sense of the total energy shift for linearly polarized light.

The total DC polarizability is significantly smaller than Dy [33] and Er [104] at 1 μm wavelength, but this calculation nevertheless indicates that holmium can be optically trapped with commercially available high power 445 nm or $\lambda > 1$ μm lasers. With beam waists of $\sim$6μm and powers of 600 mW at 445 nm, trap depths of 2 mK should be readily accessible, well in excess of the MOT temperatures $\sim$100 μK that have been demonstrated by our MOT [29] at detunings of 2-3 Γ.

We can gain a more detailed sense of the trapping potentials by examining it in the $|F, m_F\rangle$ basis. We replace the sum over fine structure states with a sum over hyperfine states

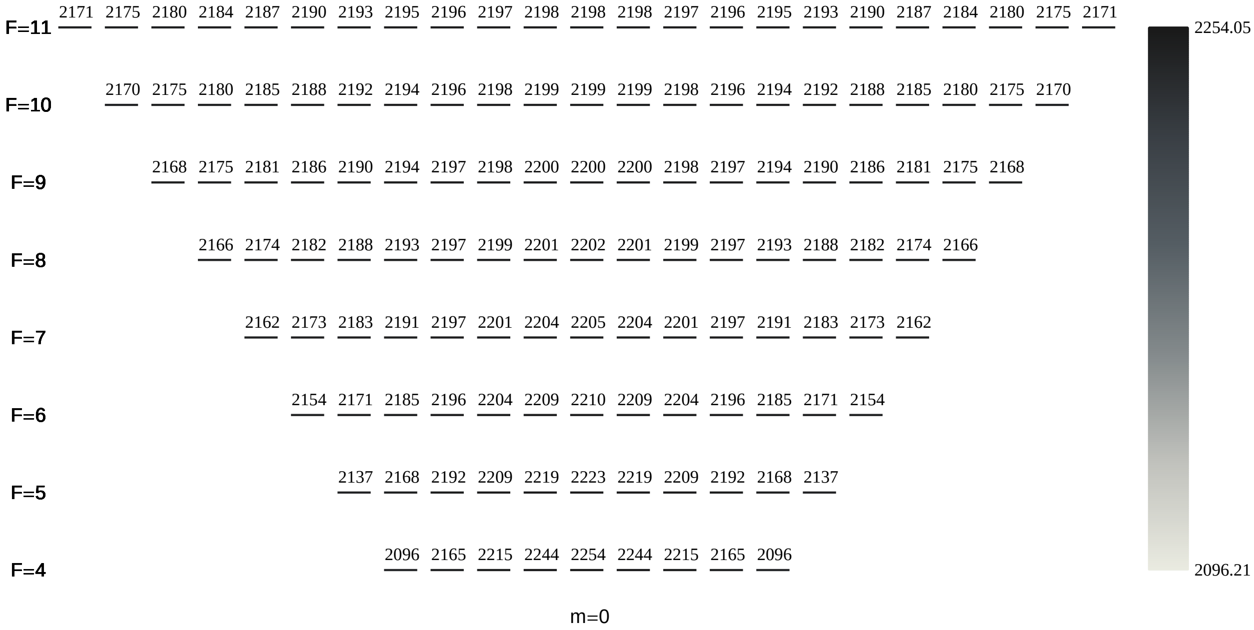

Figure 5.2 Dipole trap depths for $w_0 = 6\mu$m, $P = 600$ mW, $\lambda = 445$ nm in the $|F, m_F\rangle$ basis.

$$\alpha_{0_F} = \frac{2}{3(2f_a+1)} \sum_b \frac{\langle b||d||a\rangle}{\omega_{ba} - \omega} \tag{5.8}$$

$$\alpha_{2,F} = \alpha_2 \frac{3K(K-1) - 4F(F+1)J(J+1)}{(2F+3)(2F+2)F(2F-1)J(2J-1)} \tag{5.9}$$

where $K = F(F+1) + J(J+1) - I(I+1)$. The energy shift is analogous to eqs. 5.4 and 5.6.

$$\Delta U = -\frac{|\varepsilon|^2}{4}\alpha_{0,F} + \frac{|\varepsilon|^2 - 3|\varepsilon_x|^2}{8} \frac{3m_F^2 - F_a(F_a+1)}{F_a(2F_a-1)} \alpha_{2,F} \tag{5.10}$$

Again using our experimental parameters of $w_0 = 6\mu$m, $P = 600$ mW, $\lambda = 445$ nm, we find that our trapping potential is very isotropic for our MOT atoms that have been pumped into $F = 11$ (Fig. 5.2). In fact, we find similar trap depths for all of our hyperfine manifold, differing at most by 150μK.

Calculation	Measurement	State	α_0 (DC) (Å^3)	α_2 (DC) (Å^3)
Dalgarno [101]		Ground	25.3	-0.47
Flambaum [102]		Ground	23.2	
Saffman		Ground	20.2	-0.28
	Thorn [103]	Ground		-0.17
	de Heer [100]	Ground	21.5 (1.7)	
Flambaum		$4f^{10}5d6s^2$	21.2	

Table 5.1 A comparison of theoretical and measured values of the polarizability of the Ho ground state $4f^{11}6s^2$ and one excited state.

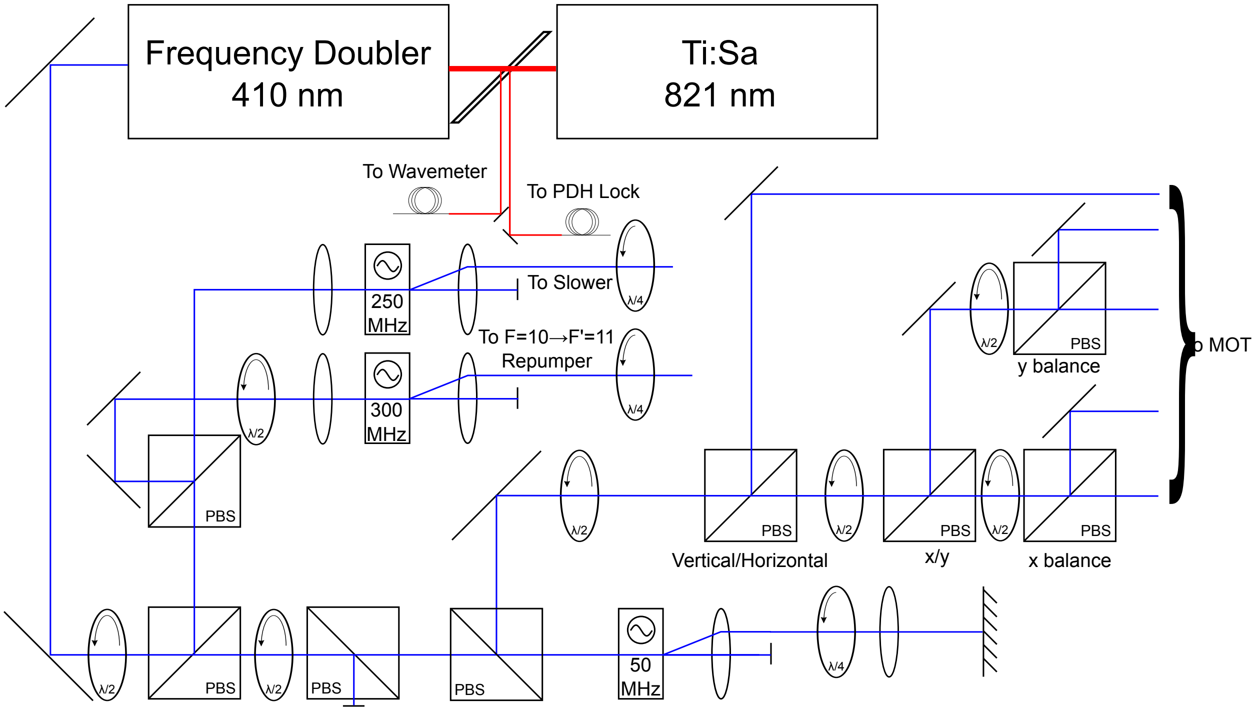

Figure 5.3 The modified optical layout for ODT experiments.

5.3 Experiment

5.3.1 Experimental Setup

5.3.1.1 Cooling Light

A few changes were made to our laser setup. Because the ODT is a conservative potential and cannot itself cool atoms, far off-resonant light must be used to cool the atoms into the trap. For this reason, we must keep our MOT beams on as an optical molasses during the optical trapping after turning the quadrupole field coils off. In our previous optical layout, the MOT beams were retroreflected for increased power to the cooling light. The main drawback to this technique is that the retroreflected beams always have less power because of losses from passing through eight surfaces (twice through a viewport and twice through a quarter waveplate) and reflecting off of a mirror. Unless the beams are weakly focusing, the difference in intensities lead to imbalance in the restoring forces and push the cooled atoms away from the ODT focus. To correct for this, we instead split the x and y cooling beams on a PBS to allow for fine-tuning the beam balances along those axes (Fig. 5.3). The z beam is left retroreflecting because of space and safety considerations. It is weakly focused to compensate.

5.3.1.2 Imaging

Imaging is done with a Princeton Instruments ProEM camera positioned at one of the 2 3/4” windows perpendicular to the atomic beam. The optical system (shown in Fig. 5.4) uses a four-lens system described in Ch. 2 with focal length $f = 11.5$ cm and numerical aperture NA=0.22 to collect light from the trap. The collected light is spatially filtered with a pinhole and then reflected off of two longpass dichroics with cutoff wavelengths of 425 nm. After this, the light enters a shielded lens tube capped with a filter centered at 415 with a passband of 10 nm. This filter has been measured to have a transmission of 90%. The filter combined with the longpass dichroic that reflects light with wavelength shorter than 425 nm and a black shroud covering the entire imaging setup creates a very effective block against room light.

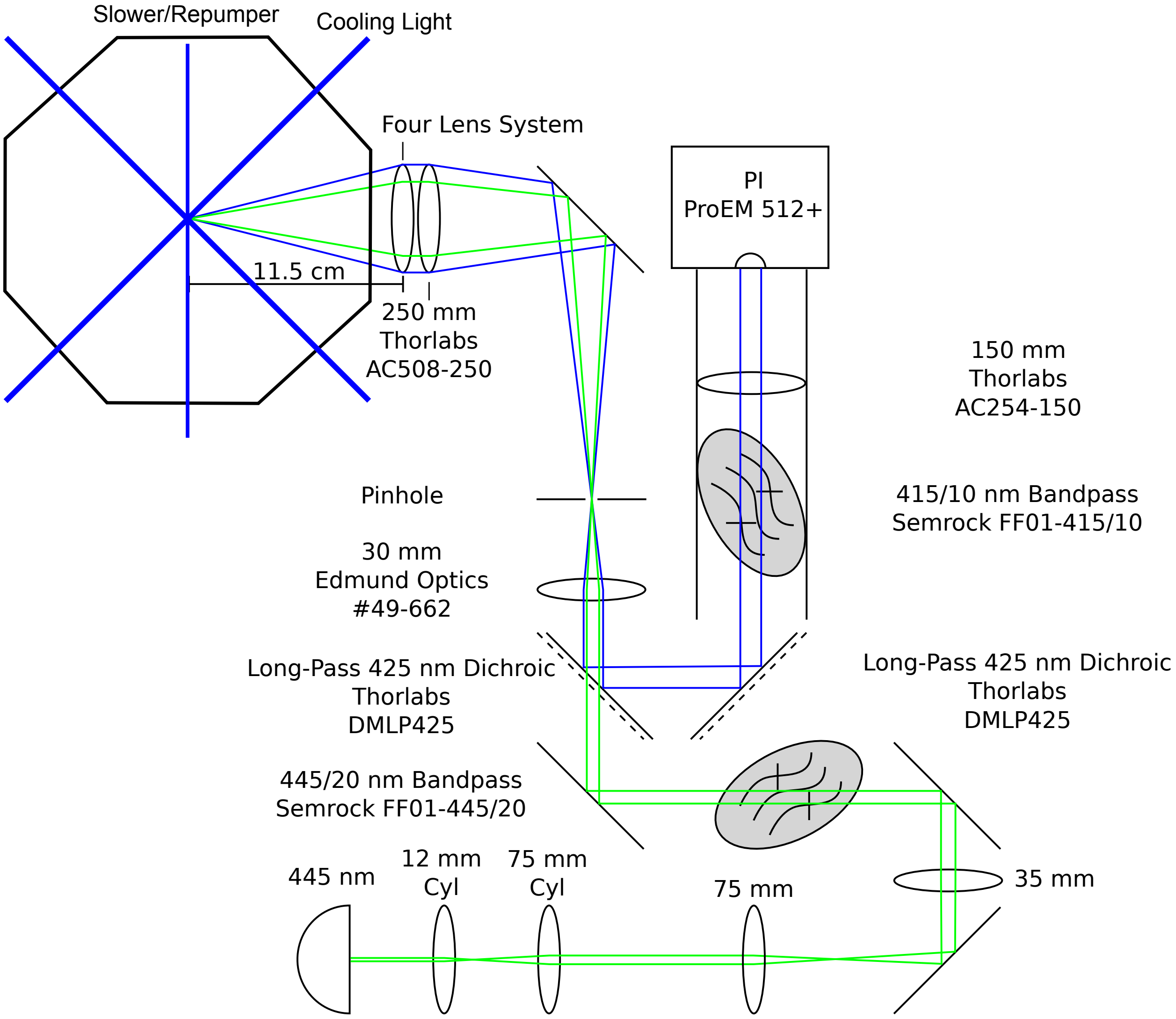

Figure 5.4 Schematic diagram of the imaging and ODT optics with respect to the vacuum chamber.

5.3.1.3 ODT Laser

The reason for this heavy filtering is because the optical system is shared with our ODT beam. We used a commercial 445 nm 900 mW diode laser as our trap laser. The beam is shaped by cylindrical lenses to be collimated and non-astigmatic incident upon the 2:1 telescope. The telescope prevents clipping of the beam on the later optics. The ODT has been measured to have some light at 410 nm (Fig. 5.5), so a bandpass filter with a center at $\lambda = 445$ nm and a FWHM $\Delta\lambda = 20$

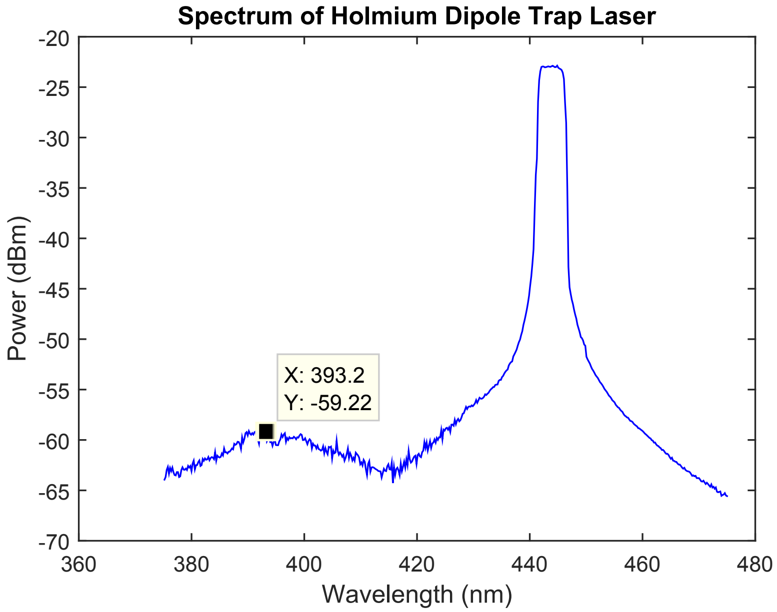

Figure 5.5 Spectrum of our ODT laser.

nm is added to prevent the ODT light from saturating the camera. The ODT beam is joined to the imaging optics with one of the dichroics so that it focuses at the same spot as the camera.

We have measured the critical parameters of the ODT. The waist of the ODT was measured to be 12 μm with a good-shaped profile. The beam was measured to have a power of 600 mW at the trap. As our calculations showed in section 5.2, this should produce a trap depth of around 500 μK. At this trap depth, we expect our trap frequencies to be [104]

$$\omega_r = \sqrt{\frac{4U}{mw_0^2}} = 2\pi \times 4200 \text{ Hz} \tag{5.11}$$

$$\omega_z = \sqrt{\frac{2U}{mz_R^2}} = 2\pi \times 35 \text{ Hz}. \tag{5.12}$$

These trap frequencies are important when considering our heating rate due to laser intensity noise. The intensity noise can be characterized by its fractional fluctuation $\epsilon(t)$ where [105]

$$\epsilon(t) = \frac{I(t) - I_0}{I_0}. \tag{5.13}$$

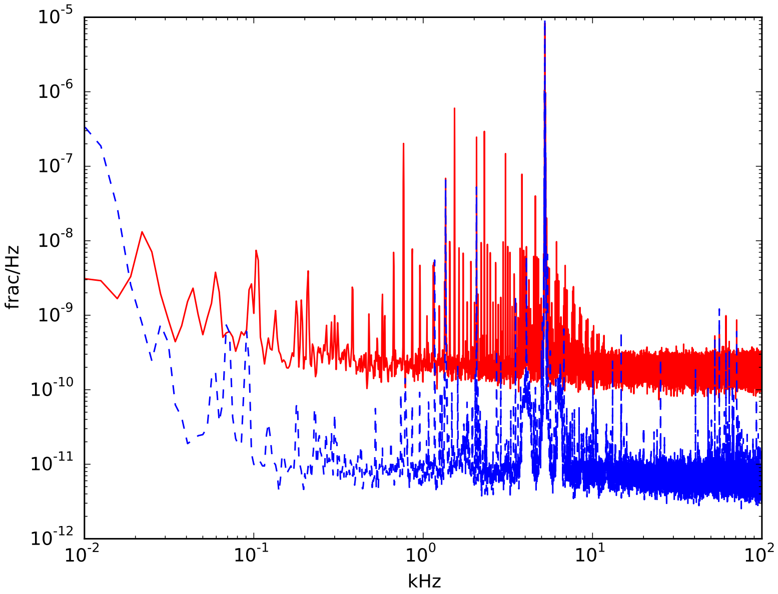

Figure 5.6 (Red) The noise spectrum of our dipole trapping beam seen on our photodetector. (Blue) The shot-noise limited spectrum of a flashlight on the same detector.

From this, we can calculate the one-sided power spectrum S_e of our laser intensity noise.

$$S_e(\omega) = \frac{2}{\pi} \int_0^\infty d\tau \cos(\omega\tau) \langle \epsilon(t)\epsilon(t+\tau) \rangle \tag{5.14}$$

We are interested in finding the heating rate from the laser noise characterized by the *e-folding time*. The e-folding time is the time T_1 for a sample to increase in temperature by a factor of e. It is dominated by contributions from noise at twice the trap frequency. The expression for this for an ODT with trap frequency ν is

$$\frac{1}{T_1} = \pi^2 \nu^2 S_e(2\nu). \tag{5.15}$$

We measured our noise spectrum on a Thorlabs PDA36A at 20 dB gain with a bandwidth of 1.0 MHz. This is a powered photodetector that has a linear voltage response to light intensity. To compensate for noise in the detector, we also measured the noise spectrum of a flashlight with an incandescent bulb with same intensity on the detector. The flashlight is a shot-noise limited light source that provides a very clean spectrum with which to compare the detector and laser noise. It

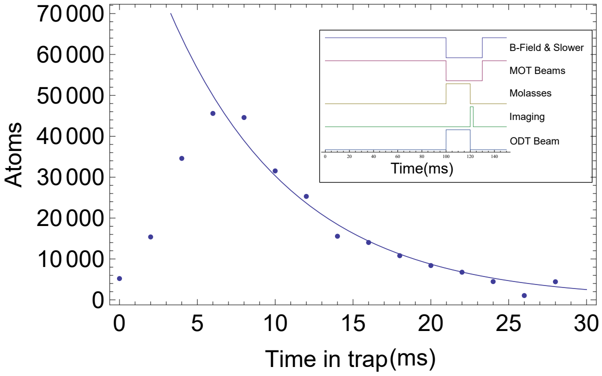

Figure 5.7 Lifetime measurement of the ODT. Inset: Timing diagram of the ODT loading process.

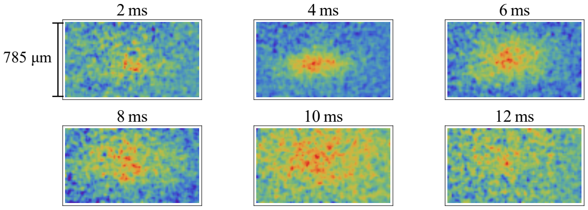

Figure 5.8 Evolution of the spatial distribution of the ODT.

is important that the DC offset on the detector be the same for both measurements so that $\epsilon(t)$ is not incorrectly inflated by low I_0.

The two power spectra are shown in Fig. 5.6. Because our data is discrete, we applied a 3-point moving average around ν_r and ν_z. This moving average is negligible because our data set was 1.25×10^6 points. We subtracted the two power spectra to obtain the actual laser noise and used this to calculate the e-folding rate. The actual rate depended on the exact type of power spectrum transformation we used, but it was typically 2-8 s in the radial direction and 3-7 s in the axial direction.

5.3.2 Results

Our experiments demonstrate very low levels of dipole trapping. We see clear evidence of increased atomic population in the region of the trap that exists for several ms (Fig. 5.7). In the data presented, we find a lifetime of 8.0 ± 0.6 ms from a MOT loaded at 100 MHz detuning (3.1 Γ) and cooled with 140 MHz (4.4 Γ) light. This is, however, an extremely short lifetime for a dipole trap at pressure $\sim10^{-10}$ T. Examination of the region of interest shows a local increase in the atomic density near the center of the trap that rapidly expands out of the trap (Fig. 5.8). While the increased signal does have the cigar shape typical of an ODT, the atoms are not well localized to the ODT size and diffuse very quickly. We interpret this to mean the atoms are almost immediately boiling out of the trap.

5.3.3 Explanation of Short Lifetime

The lifetime of the ODT is extremely short for its background pressure. There are several reasons that the might be. One reason could be that we have simply failed to achieve the appropriate trap depth. We have a trap depth several times greater than our MOT temperature, but have been typically lacking when compared to the rule of thumb that trap depths should be an order of magnitude larger in temperature. Our polarizability is also uncertain; perhaps our trap depths are actually much smaller than those that we have calculated. In addition, the polarizability of the excited state $4f^{11}6s6p$ is totally unknown and could shift in such a way that our cooling beams are actually much closer to resonant than we expect or even blue-detuned from the cooling line so that they actually are heating the atoms. The relative frequency shift could be investigated by observing spectral line shifts in either the MOT or a hollow cathode tube while perturbing the energy levels with our dipole trap light.

Heating due to the MOT equipment turning off may also be to blame. The magnetic quadrupole field shuts off slowly relative to our ODT lifetime, on the order of 10 ms, and does not fully shut off until about 15 ms. We have seen evidence that the quadrupole field changes the spatial distribution of untrapped atoms as it shuts off from MOT time-of-flight experiments. It is possible that the magnetic field does not shut off cleanly and heats the atoms out of the trap. We may therefore need to upgrade our MOT coils to provide a cleaner shut-off. It is also possible that our five beam MOT is simply unbalanced and that our cooling light blows our atoms out of the trap. We have been very careful to balance these beams properly but dipole traps can be very sensitive to these errors.

We do not think that the ODT light itself is blowing away any atoms. Our laser line filter eliminates most of the light from any frequencies resonant with strong lines and we do not see any fluorescence from the beam. The excess is also not a false positive due to charge building up in our camera while the ODT light is on. The fluorescence signal is seen on our Andor camera that does not share a beam path with the ODT light and it is not seen when there is no MOT loading.

Rare Earth Isotope	Statistics	I	J	F	Ground States	HF Structure
$^{162,164}_{66}$Dy[33, 106]	Boson	0	8	8	17	None
$^{161}_{66}$Dy[106]	Fermion	5/2	8	11/2→21/2	102	Inverted
$^{163}_{66}$Dy[33]	Fermion	5/2	8	11/2→21/2	102	Regular
$^{168}_{68}$Er[65]	Boson	0	6	6	13	None
$^{169}_{69}$Tm[99]	Boson	1/2	7/2	3→4	16	Inverted
$^{168,170,172,174,176}_{70}$Yb[44]	Boson	0	0	0	1	None
$^{171}_{70}$Yb[107]	Fermion	1/2	0	1/2	2	None
$^{173}_{70}$Yb[107]	Fermion	5/2	0	5/2	6	None

Table 5.2 A list of all of the optically trapped rare earths and the features of their hyperfine structure. All except for ^{163}Dy have no hyperfine structure or an irregular hyperfine structure, preventing hyperfine changing collisions.

Another major reason that we propose to explain this is the presence of hyperfine changing collisions in the ensemble, which is known to dramatically decrease trap lifetimes in other elements[95]. The other rare earths that have been optically trapped have either no, an inverted, or non-monotonic hyperfine structure that allows their closed, maximum F cooling transition to cycle on the lowest energy hyperfine state as demonstrated in Table 5.2. Of those cooled into a MOT, only ^{163}Dy has a regular hyperfine structure. It has not been shown to be trapped in an ODT for any appreciable amount of time even after loading from a narrow-line MOT[33].

If this is the reason for our short lifetimes, we should be able to achieve single-atom trapping. Hyperfine changing collisions are a pairwise collision processes and so we should be able to see trapping of single atoms when we initialize our trap with an odd number of atoms. We discuss some interest in single-atom trapping of holmium in chapter 7.

There are several solutions that we could implement to combat hyperfine-changing collisions. The first is to try to make a MOT on the $F = 4 \to F' = 5$ transition, which requires repumpers on $F = 5 \to F' = 5$ and $F = 6 \to F' = 5$. Because this is formed on the lowest energy level of the hyperfine manifold there would be no hyperfine changing collisions. We have attempted this and the results have been shown in section 3.2. As shown in that section, the basic power requirements of this solution are very technically difficult and we were not able to observe such a MOT.

Another solution is to optically pump our MOT into the $F = 4$ state using coherent pulses of microwaves to transfer our population from $F = 11$ to $F = 4$. The time of this transfer would have to be significantly faster than our dipole trap lifetimes.

It is also possible that we may be able to magnetically tune our collisional cross-section using bias magnetic fields. It has been shown that Feshbach resonances in ultracold rare earth gases of Dy can enhance scattering rates and rapidly destroy optically dipole traps[23]. These resonances become wider and more numerous at high atom temperatures. The Dy experiments were done at temperatures of around 800 nK, two orders of magnitude below our MOT temperatures, with very modest magnetic field magnitudes of less than 6 G demonstrating dozens of Feshbach resonances. We have attempted to tune out our inelastic dipolar scattering crossing with a bias magnetic field over similar magnitudes but did not observe any measurable effect on our trap lifetimes. It is likely that our atom temperatures are too high to reproduce the results in [23]. Perhaps loading a narrow-line MOT would lower us to the required temperatures.

5.4 Conclusion

In this chapter, we performed many calibrations of the equipment to ensure that it is suitable for use in a dipole trap. We have calculated the expected parameters needed to optically trap holmium, comparing it to the relevant literature. The early results show some very short-lived trapping but indicate that our atoms are rapidly boiling out of our ODT. We have reviewed a number of issues that could be causing the problems and we have proposed several remedies for them.

Chapter 6

Experimental Upgrades

6.1 Introduction

The current experiment chamber is somewhat restricted in optical access. It is therefore advantageous to transport our dipole trap into a glass cell. This is also an opportunity to improve various aspects of the experiment.

6.2 Vacuum Upgrades

A CAD drawing of entire chamber is shown in Fig. 6.1. Starting from the atomic source on the right, the upgrades are as follows:

1. Two unused spherical cubes are removed, reducing the volume under vacuum and potential for leaks.

2. The ion pump that was on one removed spherical cube is moved to the atomic source, providing a more direct pump to the virtual leak.

3. A Zeeman slower made of permanent magnets is added. Only its support is shown. Details of the slower can be found in [108].

4. A second gate valve is added. The new chamber is too long (128 cm) to fit inside of our oven. The two gate valves allow them to be independently pumped down and baked.

5. The ion pump that was on the other spherical cube is placed closer to the MOT chamber, doubling its conductivity to the volume of interest.

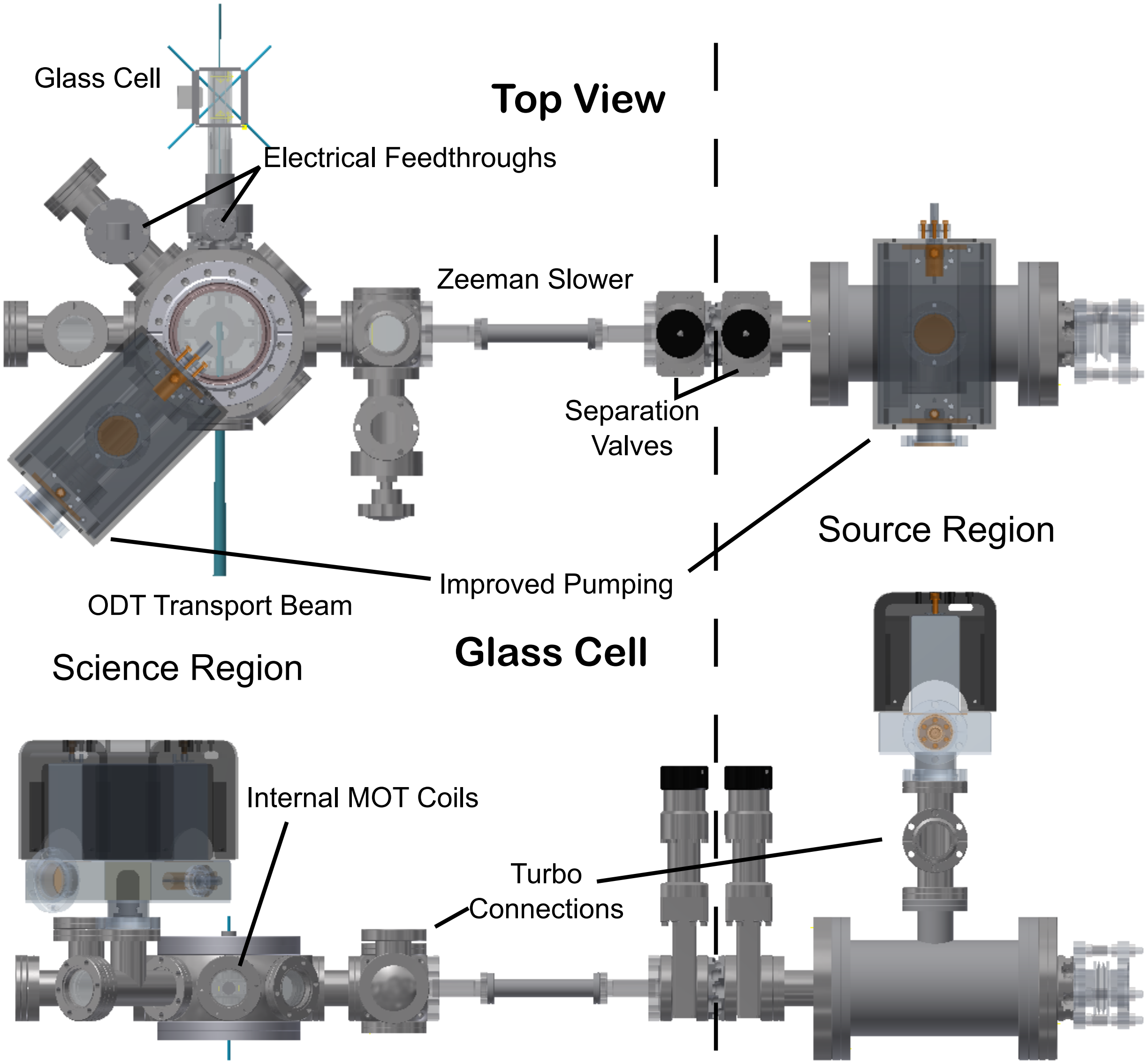

Figure 6.1 CAD drawing of the proposed changes to the vacuum system.

6. The MOT coils have been moved inside of the vacuum. This is fully detailed in 6.3.

7. A glass cell is added to increase optical access. Because it is far off-axis from the atomic beam, the atoms must be transported into the cell. The appropriate optics to transport a dipole trap are discussed in section 6.4.1.

8. A custom made breadboard (not shown) creates a second optical tier and increases the stability of the optics.

6.2.1 Pressure Improvements

Many of the hardware changes may improve the vacuum pressure. In the source region, a spherical cube, four viewports, and a tee have been removed. This reduces the surface area by $\sim$15% and the volume by $\sim 5\%$, which is nice but should not produce significant change. There should be a lower leak rate due to the reduction in parts decreases the number of Conflat connections by about a factor of two. The speed of the pump is increased because the conductance of the vacuum system restricting molecular flow is increased.

We can estimate this increase by noting that in molecular flow, conductance is measured in L/s by the formula $C = 12.4D^3/L$, where D is the diameter of the tube and L is its length in cm[109]. Right angle bends decrease the conductance by a factor of two[110]. By removing two right angle bends and reducing the length of tubing used from 28 cm to 6.35 cm, we estimate that we increase the conductance to the 6" tee that contains the holmium source by a factor of about 16. Using the dimensions of the tubes for D, we can estimate that the conductance presently is about 6 L/s, so we should end up with a conductance of about 100 L/s, well in excess of the 20 L/s that our ion pump can actually provide and therefore potentially only providing a smaller, factor 3-4 gain in pumping speed. Because ultimate pressure is inversely proportional to pumping speed, we may see a modest improvement in our vacuum in the source region.

The science region may see a substantial improvement to the pressure. A major leak to the science region is from the source region, which is typically two orders of magnitude higher pressure. This differential is maintained by our 2.5 mm diameter pinhole drilled into a copper blank. This hole only slows the diffusion into the science chamber and leaving the gate valve that presently separates the two regions open overnight has been known to raise the pressure in the science region by two orders of magnitude to 10^{-8} Torr. Because we are adding a Zeeman slower, a 12" (305 mm) tube will replace our pinhole. This tube has been custom designed to have a 2 mm diameter aperture instead of a more typical 19 mm aperture. We can estimate the change in conductance in this case by using Dushman's table[110]. The conductance from the source chamber to the science chamber will therefore be reduced from ~2.4 L/s to $C \ll 0.1$ L/s, perhaps even by several orders of magnitude (although it is not clear how these rules scale with such skinny, long apertures). It is safe to claim that the two systems will be effectively separated from each other except for a thin atomic holmium beam. The holmium should not be much of a contaminant to our experiments and has been known to act as a getter.

There is no significant change in the volume from our changes to the science region, although the surface area increases noticeably due to the extra hardware that will be installed. Because everything is UHV safe, we hope that with proper cleaning the surface area increase will negligibly impact our ultimate pressure. Our ion pump is moved from 37 cm to 12.5 cm and a right angle is removed, increasing the conductance from ~5 L/s to ~27 L/s. This is still beneath the 35 L/s pumping speed our ion pump has, so we may be able to actually decrease our pressure by a factor of about 5, even neglecting the reduced contamination from the source area. This could produce a vacuum that is regularly low 10^{-11} Torr in the science chamber.

6.2.2 Assembly

Before use, the vacuum chamber must be baked under vacuum to 200 °C to remove excess water vapor from the surface inside the chamber. It is too large to be placed inside our oven, so it must be broken into pieces to bake. There are two gate valves that can be used to do this separation. During preparation, they are sealed. A turbo pump can connect through angle valves to the turbo vacuum ports indicated in Fig. 6.1. When a side has finished baking, the angle valves can be closed to prevent the reintroduction of atmospheric gases and the ion pump will be able to hold the pressure of the vessel steady while the other side bakes. One both sides are baked out, they can be connected via a 2.75" close coupler between the gate valves. While the close coupler is only 0.7" deep, it contains enough air to easily overwhelm an ion pump. Because the source pressure is far less important than the pressure in the science region, the close coupler is placed on the source side of the Zeeman tube. After connection, the source ion pump should be turned off to protect it and a

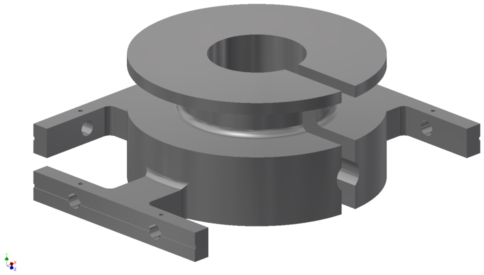

Figure 6.2 A CAD drawing of the new MOT coil holder.

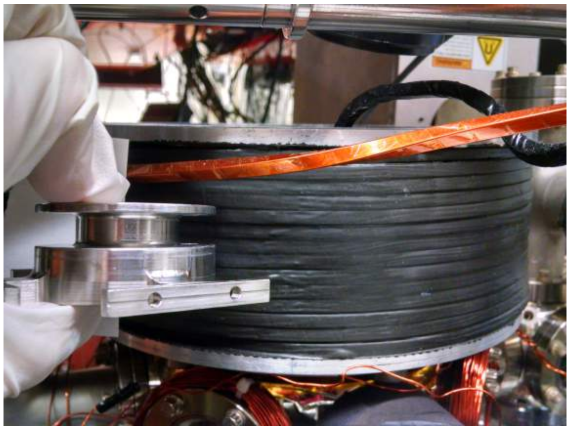

Figure 6.3 Physical comparison of the present MOT coils with the proposed new coil holder.

turbo pump attached. The gate valve to the source region can then be quickly repumped down to safe pressures and the chamber should be ready for experiments within a few minutes.

6.3 MOT Coils

Our current MOT coils turn off slowly ($\sim$10 ms). This is caused by the large inductance of the coil and a solid aluminum coil holder that sustains eddy currents. It is possible to turn the coils off faster, but doing so results in large voltage spikes on the ground plane, causing sparks between the coil and the vacuum chamber and interfering with locks, triggers, and other operations around the table. We will solve all of these problems by redesigning the MOT coils to be inside the vacuum chamber.

The new coils are mounted in a 304L stainless steel coil form. The form has a slot in it to eliminate large eddy currents. Sharp internal corners are avoided to prevent buildups of vacuum contaminants and several vent slots and vent holes are included to eliminate air pockets (Fig. 6.2). The coil form is designed to mate with groove grabbers attached to the 6” port of the MOT chamber. The inner radius of this coil form is 10 mm.

The new coil will be made of Kapton coated, UHV safe 18 gauge copper wire. Each coil will have an inner radius of 1.6 cm, an outer radius of 2.75 cm, and a height of 0.8 cm. This supports a coil of 60 turns, 10 in the radial direction and 6 in the vertical z direction. The separation between the coils will be 1.6 cm. The magnetic field for a pair of circular loops of current a distance D away from the origin in an anti-Helmholtz configuration is given to first order by

$$B_z = 3\mu_0 I \frac{DR^2}{(D^2 + R^2)^{5/2}} z \tag{6.1}$$

$$B_\rho = -\frac{3}{2}\mu_0 I \frac{DR^2}{(D^2 + R^2)^{5/2}} z \tag{6.2}$$

where R is the radius of the loops and I is the current. The gradient in each direction is easily shown to be just the prefactor of the equations, with the gradient being twice as strong in the z direction as the radial. At large separations compared to the dimensions of a wire coil forming the current loop, the current in a wire can be replaced by the term NI to signify the number of turns times the current in each turn. However, because our coil separations are of the same length scale as the size of the coils, we must calculate each loop individually for its distance D and radius ρ depending on where it in the wire bundle. These parameters can be estimated by the wire diameter and how many turns it is in each dimension from the lower, inner coil.

Performing this calculation, this configuration gives a gradient of 14.7 G/cm/A, so we should run at $\sim$2 A. This is within the capabilities of the normal coil drivers used in the lab which output a maximum current of 3 A. The power is provided *in vacuo* by a sub-D electrical feedthrough located in one of the tees (Fig. 6.1) capable of providing 5 A at 500 V. The feedthrough is part of a kit that includes a bundle of UHV safe wires that can be connector via barrel connector to the MOT coils and a UHV safe connector that securely plugs in to the sub-D feedthrough. This kit allows us ease of construction and eliminates the need for solder which may threaten the integrity of the vacuum.

The inductance of a coil of these dimensions is $\sim 200\mu$H, a factor of ten smaller than the present coils. The resistance is $\sim$105 mΩ, which is about 2/3 that of the present coils (Fig. 6.3 shows a size comparison). The current needed is 2 A instead of the 30 A used in the present coils, leading to a power use of 0.3$\%$ that across the present coil. The IGBT in the present setup has a voltage drop of 1.7 V, leading to a total of 210 W dissipated in the coil circuit. The new design compares very favorably by only using 0.45 W. The current decay constant of a solenoid is L/R, so we estimate that these coils can turn off at least 7 times faster than the current coils. We are optimistic that this could be even faster with the slot added to the coil form to reduce eddy currents and the reduced amount of power being dumped to ground.

A major concern of internal magnetic field coils is heat dissipation. The wire is coated in Kapton, stable to 400 °C, so outgassing of the material is not a concern. However, high temperatures could lead to stress on the nearby viewports and their coatings, increased blackbody radiation, increased resistance that may stress the coil drivers, and magnetic field instability if the coils are irregularly cycled. We can make a pessimistic estimate of the equilibrium temperature by neglecting conductive heat losses and solving for the temperature at which the radiative losses match the absorbed power into the coil. The Stefan-Boltzmann law states that

$$P_{rad} = A\epsilon\sigma T^4 \tag{6.3}$$

where the power P_{rad} emitted by an object is related to its temperature T, its emissivity ϵ, its area A, and the Stefan-Boltzmann constant $\sigma = 5.67 \times 10^{-8}$W m^{-2}K^{-4}. At steady state at room temperature, this power is $P_0 = A\epsilon\sigma(300)^4$. We add in the electrical power dissipated in the coil, P_e=0.45 W. Because the faces of the MOT coil holders that face towards each other emit directly into each other, we neglect their contribution to the emission. We estimate an ϵ of 0.5 given that the coil in made up of a moderately polished stainless steel coil holder (ϵ~0.07) and a rough Kapton coated copper coil (ϵ~0.9). Adding the two contributions to the power in and solving for T gives

$$T_{eq} = \left(\frac{P_0 + P_e}{A\sigma\epsilon}\right)^{1/4} \tag{6.4}$$

This calculation gives us an equilibrium temperature of 45 °C. This is very manageable, but may be moreso if conductive losses to the chamber are significant. The rate of heating immediately after the coil is turned on can be estimated by considering the specific heat c of the copper coil (C) and stainless steel holder (H) and the electrical power dumped into them.

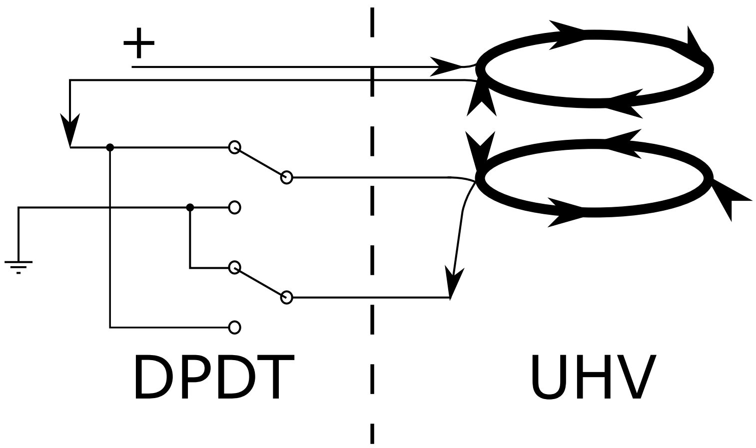

Figure 6.4 An electrical schematic for switching the magnetic field coils between Helmholtz and anti-Helmholtz configurations. This demonstrates the switch in the anti-Helmholtz configuration.

$$P_e = \frac{dQ}{dt} = (m_H c_{ss} + m_C c_{Cu})\frac{\Delta T}{dt} \tag{6.5}$$

This is only valid immediately after the coil in turned on when there is no excess heat dissipated radiatively or conductively. Later heating should only be slower as the coil reaches an equilibrium temperature. With an 8 m long, 18 AWG copper coil estimated to be 0.35 kg and a stainless steel coil holder estimated by our CAD program to be 0.31 kg, we find an initial heating rate to be 0.1 °C/min, indicating that there will be no runaway heating. This is well within the heating rate tolerance of the viewports (2-3 °C/min [111]) and indicates that there will be plenty of time to turn the coils off if they become intolerably hot.

Because these are rough estimates, it is important to monitor this in vacuum. The temperature dependence of resistance is given by

$$\frac{\Delta R}{R_0} = \alpha \Delta T \tag{6.6}$$

where α is the temperature coefficient of the material ($3.9\times10^{-3}\ \frac{1}{^\circ\mathrm{C}}$ for copper). A temperature increase of 10 °C therefore leads to a voltage change of 3.9% for a constant current, which is easily measurable on the atmospheric side of the sub-D connectors. These coils should therefore be very safe to use in a vacuum.

The sub-D electrical feedthrough has 9 pins. The MOT will use four of the pins, one pair for each coil. The coils will be connected in series to ensure uniform current. This series connection will be performed outside the chamber with a double pole changeover (DPCO) switch that will allow us to easily change from anti-Helmholtz to Helmholtz configurations (Fig. 6.4). This feature may allow us to perform interesting experiments (e.g. Stern-Gerlach imaging or creating magic conditions for pairs of hyperfine states) in a biased magnetic field in the future.

6.4 The Glass Cell

We use a commercial glass cell AR coated to 1% reflection for 400-1100 nm from Precision Glassblowing of Colorado. This provides us with the flexibility to use the cooling light from any of our cycling transitions described in chapter 1, the ODT light at 445 nm, and possibly 821 nm or 1064 nm light for dipole trapping at far red detunings. The cell gives us a large amount of optical and magnetic access. Because it protrudes from the chamber a large distance away from the atomic beam, we will have to transport cooled holmium atoms into it using an optical transport beam.

6.4.1 Dipole Trap Transport

We require that our dipole trap maintain its trap depth over the entire transport range. This is typically done by using large mechanical translation stages that physically move all of the ODT optics together and maintain the trap waist size. Such stages can be expensive, difficult to calibrate, and can cause disruptive vibrations across the optical table. As detailed in [112], these difficulties can be circumvented by using focus tunable lenses. With one permanent lens and one tunable lens, it is possible to move the waist of a Gaussian beam without changing its size. By adding in a second a tunable lens, the position and size of the waist can be independently controlled.

We first describe how one tunable lens and one permanent lens can move the waist of a Gaussian beam without changing its size. The basic idea can be demonstrated easily with ray transfer matrices. We start with an expression for a general ray with height x_1 above the optical axis at angle θ_1. It can be transformed into a ray with height x_2 and angle θ_2 by an optical system represented by the coefficients A, B, C, D.

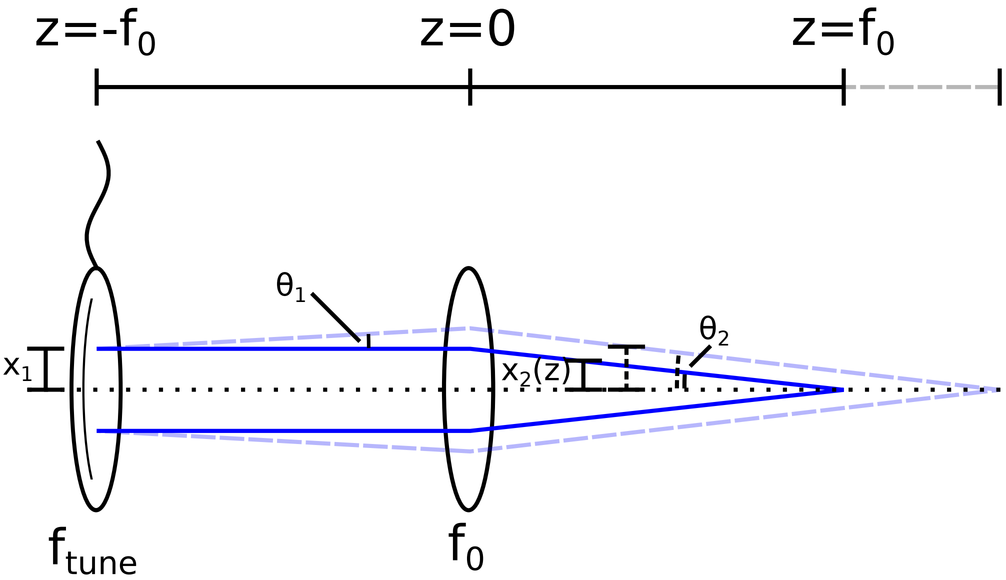

Figure 6.5 General ray diagram for ODT transport using tunable lens. An arbitrary ray transforms to have the same angle independently of the focal length f_{tune}. The invariance of this angle allows uniformly sized waist to be moved by changing f_{tune}.

$$\begin{pmatrix} x_2 \\ \theta_2 \end{pmatrix} = \begin{pmatrix} A & B \\ C & D \end{pmatrix} \begin{pmatrix} x_1 \\ \theta_1 \end{pmatrix} \tag{6.7}$$

We use the ray transfer matrices for free space (FS) and thin lenses (TL), respectively.

$$\begin{pmatrix} A & B \\ C & D \end{pmatrix}_{FS} = \begin{pmatrix} 1 & d \\ 0 & 1 \end{pmatrix} \tag{6.8}$$

$$\begin{pmatrix} A & B \\ C & D \end{pmatrix}_{TL} = \begin{pmatrix} 1 & 0 \\ -\frac{1}{f} & 1 \end{pmatrix} \tag{6.9}$$

In a system with a two lenses, one permanent lens of focal length f_0 at $z = 0$ and one tunable lens with focal length f_{tune} at $z = -f_0$, our input ray crosses $z = -f_0$ with some arbitrary x_1 and θ_1 (Fig. 6.5). The transformed ray after the permanent lens along the optical axis z is expressed by

$$\begin{pmatrix} x_2 \\ \theta_2 \end{pmatrix} = \begin{pmatrix} 1 & z \\ 0 & 1 \end{pmatrix} \begin{pmatrix} 1 & 0 \\ -\frac{1}{f_0} & 1 \end{pmatrix} \begin{pmatrix} 1 & f_0 \\ 0 & 1 \end{pmatrix} \begin{pmatrix} x_1 \\ \theta_1 \end{pmatrix} = \begin{pmatrix} x_1(1 - \frac{z}{f_0}) + \theta_1 f_0 \\ -\frac{x_1}{f_0} \end{pmatrix} \tag{6.10}$$

We observe that while the height of the output ray x_2 is dependent on θ_1, the angle θ_2 of the output ray is entirely independent of θ_1. θ_2 represents the divergence of the beam and can be uniquely mapped onto a beam waist by considering the far-field limit of the beam size $w(z) = w_0\sqrt{1+(z/z_R)^2}$ where w_0 is the beam waist and z_R is the Rayleigh range where $w(z_R) = \sqrt{2}w_0$. For $z/z_R \gg 1$, the beam diverges with a constant slope of $w_0/z_R = \tan\theta_2 = \tan(-\frac{x_1}{f_0})$. If we change f_{tune}, x_1 of the input ray does not change but θ_1 does. Thus we can change the position of the waist without changing the size of the waist simply by changing f_2. This result can be reproduced using complex beam parameters to fully describe a Gaussian beam. However, this does not produce an easily represented analytic result and so we do not present it here.

We can add further to the flexibility of this system to allow us tunable, independent control of both the waist size and position. If we place a second tunable lens before the first to independently adjust x_1 at $z = -f_0$, we can change the divergence and therefore the size of the ODT waist. The utility of focus tunable lenses in this context is apparent. A specific example of this kind of optical setup is shown in Fig. 6.6. We use Optotune EL-10-30 tunable lenses.

We have several constraints for the design of our optical system.

1. The total distance our trap needs to move is 23.5 cm to get from the center of the MOT to the center of our glass cell.

2. Over this travel we do not want clipping that will reduce our trap depth. There are four places this could happen:

   (a) The tunable lenses have an aperture of diameter 10 mm. This restricts our waist to 3 mm through either lens (99.6% transmission)

   (b) The z electrodes in the dipole trap have an inner diameter of 0.4 cm (0.157”).

   (c) The aperture between the MOT region and glass cell has a diameter of 0.61 cm (0.24”).

   (d) The new MOT coils (section 6.3) have a separation of 1.6 cm.

3. The trap depth must be suitable for our MOT temperatures.

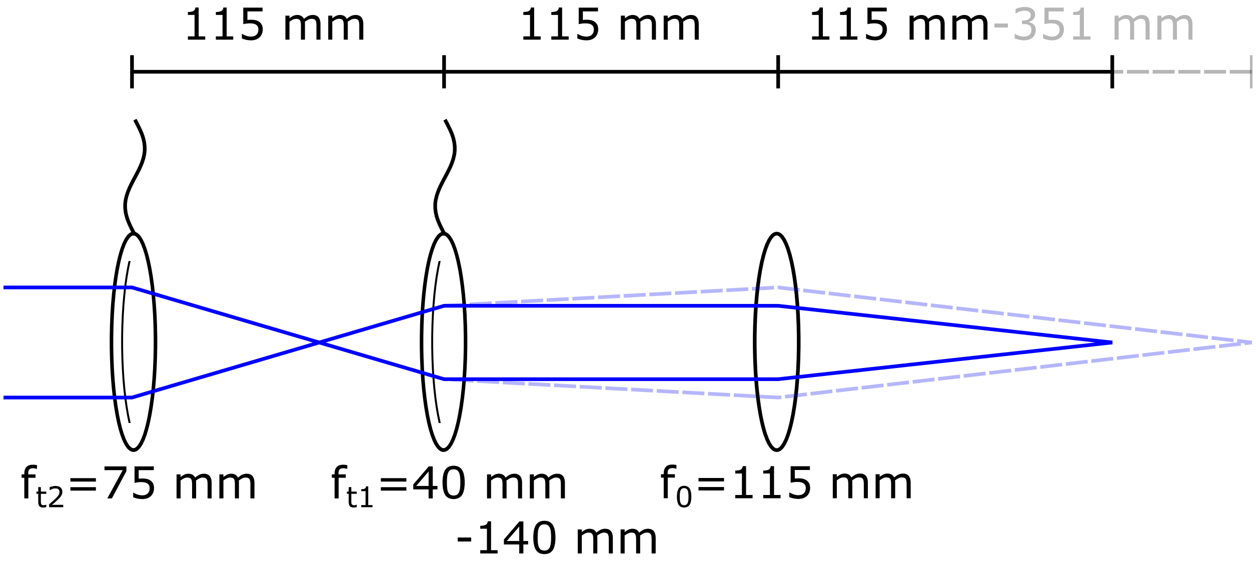

Figure 6.6 Optical layout for ODT transport using tunable lens. A beam enters a telescope of two tunable lenses and is focused by a permanent lens. The spacings indicated create a uniformly sized waist at all focal lengths of the second lens.

4. The necessary focal lengths must be within the possible range of the Optotune EL-10-30 lenses. This range has been measured to be 50-160 mm.
5. The trap needs to have one end overlapped with the MOT inside the chamber using optics from outside the chamber. This requires a minimum focal length of at least 10.4 cm (4.1").

Constraint 2 increases our trap waist to 10 μm, a reduction of 50% trap depth from the 7 μm waist used in previous experiments. This still leaves us with a 1 mK trap depth, which should still be cold enough for condition 3 given that our MOT temperatures have been measured at 70 μK (Chapter 3).

One optical setup that achieves all of these goals is shown in figure 6.6. A collimated beam with $w_0 = 3$ mm is sent through a telescope consisting of two Optotune lenses. The beam then passes through a permanent thin lens one of its focal lengths from the near lens of the telescope. The focus of the trap beam will then be at the focal length of this lens.

Condition 5 is easily satisfied by making the permanent lens longer than 10.4 cm. It has been designed to be 115 mm so that we can use the same aberration-minimizing four-lens optic that is in our current setup. The first tunable lens can be set at f=75 mm and the second to f=40 mm separated by 115 mm, giving a waist at 115 mm of 10.2 μm. This waist can be changed by changing either the focal length of the first lens or the spacing between lenses (e.g. A focal length of f_{t2} =60 mm (or a spacing of 125 mm) gives a waist of 8.1 μm, a focal length of 80 mm (or a spacing of 105 mm) gives a waist of 10.9 μm), allowing us to easily fine-tune the ODT waist to compensate for focal length errors in the lenses or optical aberrations. Both of these options retain full range of the transport but change where in space the range is located. By changing the focal length on the second lens from 40 to 140 mm, a translation of 23.6 cm can be achieved, achieving the conditions set by 1. If more translation is required, a longer focal length permanent lens can be used. By adjusting f_{t1} along its entire range, waists of 5 μm to a diverging beam can be achieved at the cost of useful translation range (i.e. there will be patches within the 11.5-35.1 cm desired translation range that will be unobtainable for certain waist sizes).

6.4.2 Technical Considerations

While simple in concept, there are several technical challenges to creating a stable translation. Tunable lenses have only recently been made at high enough quality to be viable for use in experimental setups of this nature. They are essentially a flexible membrane enclosing an optical fluid with an electromagnetic ring around the edges to control the focal length as a function of current. Because they are so much more complicated than standard glass lenses, they still present the danger of optical aberrations if handled incorrectly. In particular, they must be mounted so that their optical axis is vertical in order to ensure that the force of gravity is uniform across the entire membrane. If this is not done, large coma can result.

In addition, significant heating occurs at short (high current) focal lengths. At f=40 mm, we have measured that the temperature increases by 4 °C. The manual [113] states that the focal length changes by 0.67 diopters/°C. [112] solved this problem by using the second tunable to compensate for temperature fluctuations. We will try a different method for increased stability by mounting the lenses in custom-made, temperature controlled lens mounts. This eliminates the need for complicated compensation calibrations and is hopefully a very robust, simple solution. This solution may also provide us with the ability to tune the available focal length ranges by adjusting the temperature of the lenses.

Due to the nature of the tunable lens design, the focal length is not linear with the current. We have calibrated both lenses to obtain their focal length dependence on current. We can then map this onto a finite set of control voltages built-in voltage-to-current function in the Optotune Lens Driver Controller program. This function interpolates a function using a table of control voltages and set currents. The Lens Driver Controller then uses this interpolation to interpret any arbitrary control voltage into lens current. We found that using only seven entries into this table we can in principal reduce the error in between the calibration points to $5\times10^{-3}\%$.

The fluid nature of the lens has demonstrated some mechanical feedback issues. A test can be made of the minimum focal length modulation time by placing a pinhole after one of the tunable lens and measuring the transmission of a beam through the pinhole. As the waist on the pinhole changes, the signal measured changes. We found significant errors in the response driving the lenses at frequencies higher than 50 Hz. When a square wave was used, oscillations in the focal length persisted in the lens for $\sim$10 ms. This limitation should not be a problem as we expect to transport at significantly slower rates to prevent heating of the atoms in the trap.

6.4.3 Dipole Trap Electrodes

Since the polarizability of Rydberg atoms scales as n^7, they are very sensitive to electric fields [83]. For this reason, in our glass cell we will wish to precisely control our electric fields, usually to null out any stray electric fields. For full control we have designed a system that allows us to act in all three dimensions independently. Because the glass in the cell can act as a dielectric to cancel out external fields, our electrodes are contained entirely within the glass cell under vacuum. The compensation system consists of two annular stainless steel plates in the z direction separated by 3.4 cm and four stainless steel rods in a 1.05 cm square that allow us to control the field in the x-y plane (Fig. 6.7). A sub-C electrical feedthrough provides up to 500 V, allowing us to create fields of up to 25 V/cm in the z direction and 625 V/cm in the x-y plane. The sub-C connector is part of

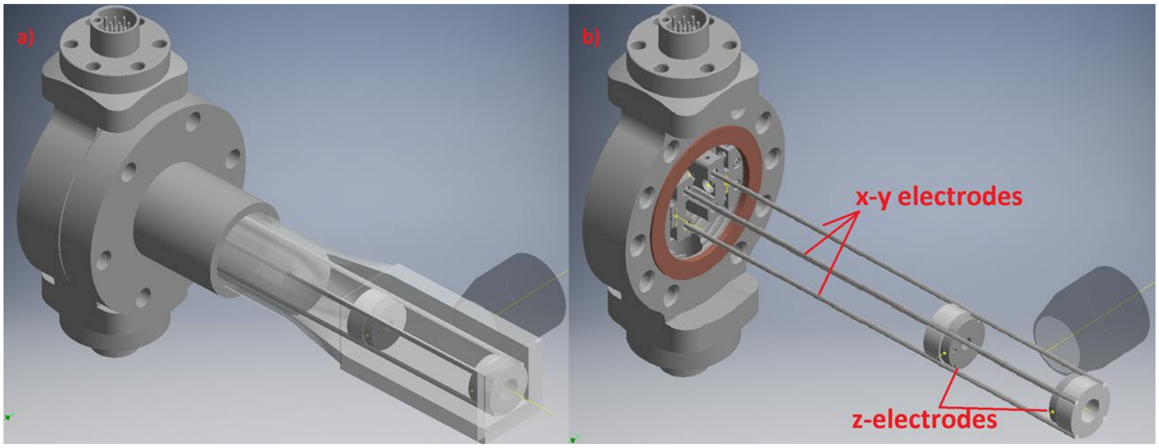

Figure 6.7 CAD drawings of the proposed glass cell electrodes. a) A full drawing including the glass cell demonstrating the fit of the electrodes. The voltage of the electrodes is supplied by the sub-C connector at the top of the drawing. b) A cut-away to demonstrate the mounting of the electrodes.

a kit similar to that described in section 6.3 allowing electrical connections to be made without the use of solder.

The x-y rods support the entire structure on a custom-machined, stainless steel mount . Two through holes to allow it to screw into a set of groove grabbers attached to the chamber walls (Fig. 6.8). The x-y rods slide into the holes in the mount insulated by alumina tubes. The rods are connected to an external voltage source via the sub-C connection, giving us full, isolated control of the fields in the x-y plane. The z electrode plates are secured by drops of the UHV-safe epoxy Torr Seal to two Macor plates that act as both support and electrical insulation. Both the electrodes and the supports have holes in them that allow us to perform the full ODT transport with <1% clipping. The electrode nearest the electrical feedthrough is very simply connected to a high-voltage source with a screw pinning a connecting wire to the surface. To avoid risking a wire falling into a beam path while making the electrical connection to the far z electrode, one of the x-y electrodes is a hollow tube. The connection to the far z electrode is routed through this tube. This wire is coated in Kapton to prevent any short circuits. It has a breakdown voltage of 2 kVDC.

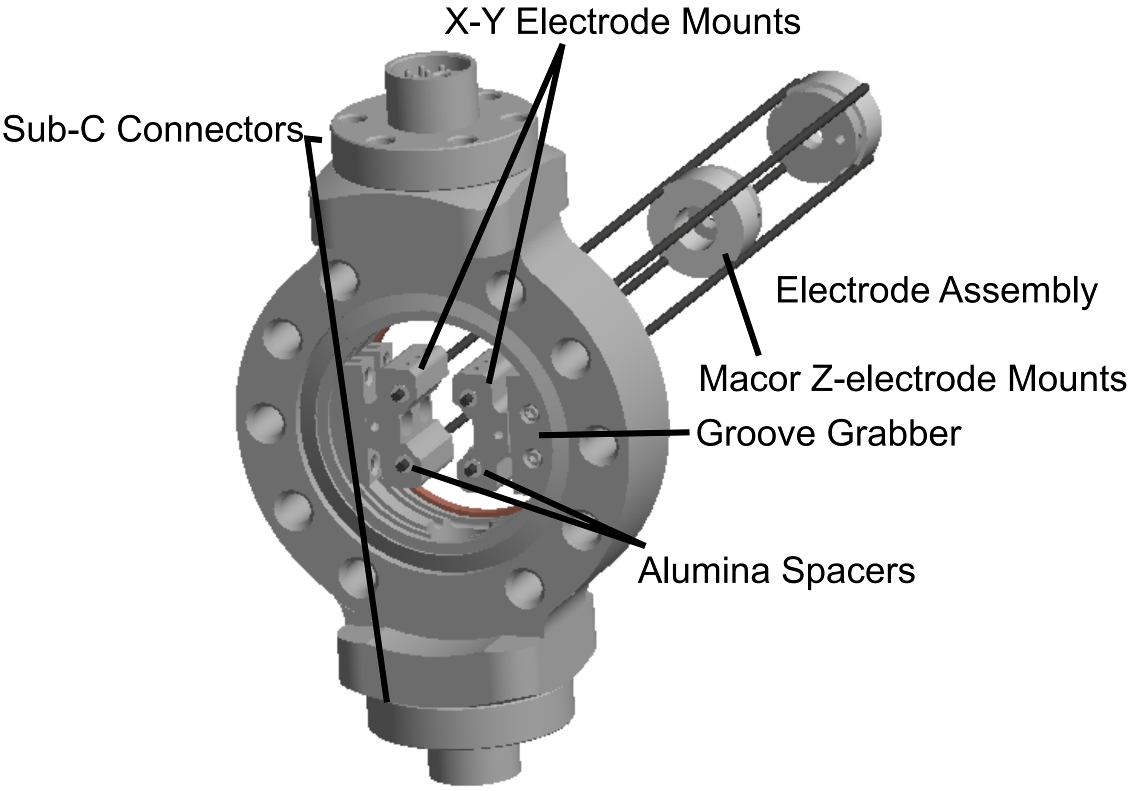

Figure 6.8 A labeled schematic of the mounting scheme of the electrodes.

The fields along the z-axis can be computed analytically by modeling the electrodes as perfect annuli. The potential along the axis of a charged annulus with charge density σ, inner radius a, and outer radius b is given by

$$V = \frac{\sigma}{2\epsilon_0}\left(\sqrt{b^2+z^2}-\sqrt{a^2+z^2}\right). \tag{6.11}$$

If we interpret this as a modified form of the potential of an infinite sheet of charge and draw an analogy to the potential of a parallel plate capacitor formed from two such sheets, we can see that the prefactor $\frac{\sigma}{\epsilon_0} = V_0/d$,where V_0 is the potential difference between the two annuli and d is the spacing between them. We can therefore express the potential and the electric field of annular electrodes in terms of the potential difference at which they are held.

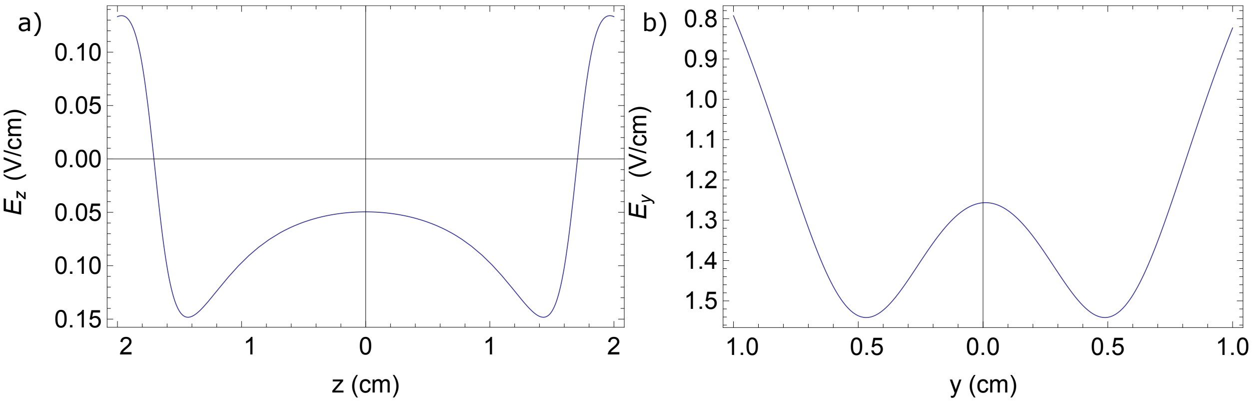

Figure 6.9 The electric fields of the proposed electrodes with ±1V. a) Two annular plates separated by 3.4 cm. b) Four rods that are pairwise-biased.

$$V = \frac{V_0}{2d}\left[\sqrt{b^2+\left(z-\frac{d}{2}\right)^2}-\sqrt{a^2+\left(z-\frac{d}{2}\right)^2}-\left(\sqrt{b^2+\left(z+\frac{d}{2}\right)^2}-\sqrt{a^2+\left(z+\frac{d}{2}\right)^2}\right)\right] \tag{6.12a}$$

$$E = -\frac{dV}{dz} \tag{6.12b}$$

This formula reproduces the parallel plate capacitor at a=0 and b≫d. Our plates have an outer radius of 8 mm and an inner radius of 2 mm. With our parameters, we find that our electric field in the center of the plates is 0.05 V/cm for ±1 V on each electrode with a curvature of 0.036 V/cm^3, giving us excellent uniformity over about 3 mm (Fig. 6.9a). If we apply a voltage difference of 1 kV, we should be able to produce an electric field in the z direction of 25 V/cm, enough to deal with most stray electric fields. The x-y rod electrodes can most easily be simulated with an iterative relaxation method to numerically solve Laplace's equation [114]. This method creates a grid of uniformly null potential points with the exception of the grid points representing electrodes. The method then sets all grid points to the average value of its adjacent points. The electrode grid points are reset to their original potentials and the edges of the grid are set to a null potential to prevent the solution from blowing up and to ensure V=0 at infinity. The process is repeated until the grid finds a stable solution. Our simulation was iterated 530000 times to achieve an error of $<10^{-10}$. We separated the electrodes by 105 pixels on a 1000× 1000 pixel grid. The potential map is shown in Fig. 6.10.The electric field with $\pm V_0$ on pairwise electrodes is predicted to be $1.25V_0$

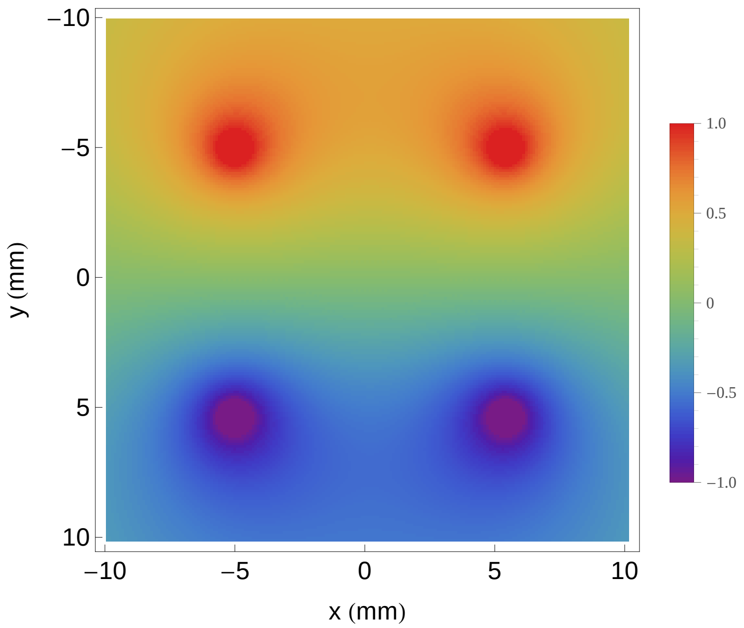

Figure 6.10 A map of the electric potential of the x-y rod electrodes numerically calculated with a relaxation method. The potential scale is in V.

V/cm with a curvature of 1.47 V/cm^3, giving us a $<1\%$ variation over $\pm 800\mu$m. The results of such a simulation are shown in Fig. 6.9b.

6.5 Conclusion

Our present setup has produced many good experimental results but time has revealed several ways in which it could be improved. In this chapter, I have detailed the changes we will make to our experimental apparatus and what benefits exactly are expected. They should enhance our background pressure, our magnetic and electric field control, our optical access, and open several new a interesting experimental avenues. We expect all of our current results to improve as we move on to more difficult experimental challenges.

Chapter 7

Use of Holmium in Single Atom Physics

In this final chapter, we perform a series of calculations beyond the collective quantum computing purposes that motivated the work done in previous chapters. We discuss three calculations specifically, all building towards using holmium in single atom quantum computing. In the first section, we discuss using rare earths for use in single-atom experiments. In the second section, we find many “magic” magnetic fields for hyperfine pairs in holmium. In the third section, we estimate holmium’s sensitivity to blackbody radiation shifts.

7.1 Rare Earths in Single Atom Imaging

In chapter 1 we reviewed several properties that could make rare earths and specifically holmium useful for single atom imaging. We commented that these could be used as an interesting alternative to the alkalis that are typically used for single atom experiments. We expound on this in this section.

One challenge to single atom imaging is scattering enough photons to create a measurable signal on a detector. This is limited by two properties of the imaging line. First, the linewidth of the atom determines the scattering rate of the atom. As shown in table 7.1, the scattering rate for the rare earths can be quite large compared the alkalis. Rare earths will therefore scatter photons more quickly and require shorter integration times for imaging.

The other property is the rate of Raman transitions out of the imaging cycle. Normally, one cycles photons on a closed $F \rightarrow F' = F + 1$ transition (e.g. Cesium’s D$_2$ $F = 4 \rightarrow F' = 5$ transition) or on an open transition with a repumper laser to maximize the number of photons

Element	Line	λ (nm)	$\frac{A}{2\pi}$ (MHz)	α (DC) (Å^3)	$\Delta E_{F\|e\rangle}$ (GHz)	μ_B
^{85}Rb	$5s_{1/2} \rightarrow 5p_{3/2}$	780	6.1	47.3	0.12[34]	1.44
^{87}Rb	$5s_{1/2} \rightarrow 5p_{3/2}$	780	6.1	47.3	0.27[35]	2.92
Cs	$6s_{3/2} \rightarrow 6p_{1/2}$	852	5.3	59.4	0.25[36]	2.82
^{161}Dy	$4f^{10}6s^2 \rightarrow 4f^{10}6s6p$	421	31.9	24.5 [116]	0.33[27]	10.6
Ho	$4f^{11}6s^2 \rightarrow 4f^{11}6s6p$	410	32.5	21.5	7.67 [29]	10.6
^{167}Er	$4f^{12}6s^2 \rightarrow 4f^{12}6s6p(^1P_1)$	401	35.6	22.7 [116]	2.04 [32]	9.6
Tm	$4f^{13}6s^2 \rightarrow 4f^{13}6s6p$	411	10	21.8[116]	1.86 [28]	7.6
^{173}Yb	$6s^2 \rightarrow 6s6p$	399	28	20.9[116]	0.21[37]	4.54

Table 7.1 A list of typical, broad cooling lines in the rare earths and their corresponding Doppler temperatures. Column 6 includes the hyperfine splittings of cycling transitions of the excited states that are used for cooling. Column 7 indicates the energy mismatch between the cooling photon and a second, ionizing photon to give some idea of the Doppler broadening of a two-photon transition to a Rydberg state. Frequently trapped alkalis are included for comparison.

scattered before a Raman scattering event off of $F' = F$ occurs and the atom is lost to some other, non-imaging hyperfine state. The rate of Raman scattering events is reduced in many of the rare earths because some, like holmium, possess large excited hyperfine splittings as a fraction of their imaging linewidth compared to the alkalis. Others, like all isotopes of Er except for ^{167}Er, have no ground hyperfine structure and large linewidths, entirely avoiding the problem of Raman scattering. These properties make holmium a good choice for single-atom experiments in fields like quantum information that require multiple ground states and erbium a good choice for experiments that do not require multiple ground states. An experiment using single erbium atoms in optical lattices to study dipolar gases with a quantum gas microscope is currently being developed by the Greiner group[115].

Rare earths also have the advantage of being highly magnetic. They can be cooled and optically trapped very similarly to the alkalis [104, 117, 33, 99, 47]. This is to be expected because their DC polarizabilities are only a factor of 2-3 times smaller than the alkalis (Table 7.1) and intense CW light fields for ODTs are generally not a limitation. Once cooled, they can be magnetically trapped in quadrupole or Ioffe-Pritchard traps that are several times deeper than what could be made for alkali atoms. These magnetic traps can be traced onto substrates. If the traps are made with only a single layer on a substrate, the atoms can be magnetically trapped above the substrate. On the other hand, if the traps are made with two layers and holes are etched out of the substrate, the magnetic minimum of the trap can be formed inside the holes of the substrate. If the substrate is optically opaque, this can drastically reduce cross-talk between nearby atoms. As discussed in section 7.2, we can even select a non-zero minimum for our magnetic traps that reduces their sensitivity to magnetic field noise.

From these arguments, we observe that there is strong reason to consider rare earths for the future of single-atom imaging.

7.2 "Magic" Magnetic Fields in Holmium

The stability of qubits encoded onto hyperfine states of neutral atoms depend critically on the magnetic field sensitivity of the hyperfine states. For this reason, single-atom qubits trapped in optical arrays are encoded $m_F = 0$ because these states are insensitive to first order to magnetic fields. This is easily seen by referring to the Zeeman Hamiltonian for an atom in a weak magnetic field.

$$H_Z = -\overrightarrow{\boldsymbol{\mu}} \cdot \overrightarrow{\mathbf{B}} = \mu_B g_F m_F |B| \tag{7.1}$$

Pursuant to a scheme of qubits encoded on paired hyperfine states of magnetically trapped single atoms as described in the previous section, we calculate the sensitivity of the states to magnetic field noise. This can be computationally expensive for holmium's 128 hyperfine states, so we first reduce the size of this problem by considering what states cannot be trapped in a magnetic potential. From eq. 7.1, we see that we can either form a trap for $m_F < 0$ (called *high-field seekers*) with a local magnetic field maximum or for $m_F > 0$ (called *low-field seekers*) with a local magnetic field minimum, and no magnetic trapping can be done for $m_F = 0$. We can further refer to Earnshaw's Theorem[118], which states that in free space the magnitude of the magnetic field $|B|$ has no local maxima. Therefore, we may only magnetically trap atoms with $m_F > 0$.

$\lvert F, m_F\rangle$	$\lvert F', m'_F\rangle$	B_{mag} (G)	$\Delta\nu_0$ (GHz)	$\frac{dU}{dB}$ (MHz/G)	$\tau(10^3$ s)	γ
$\lvert 4,1\rangle$	$\lvert 5,1\rangle$	231	4.231	2.03	47	6
$\lvert 5,5\rangle$	$\lvert 6,6\rangle$	319	5.075	10.4	Large	5
$\lvert 5,1\rangle$	$\lvert 6,1\rangle$	408	5.017	1.92	23	5
$\lvert 4,2\rangle$	$\lvert 5,2\rangle$	454	3.984	4.10	9	6
$\lvert 4,4\rangle$	$\lvert 5,5\rangle$	646	4.072	9.68	15	6
$\lvert 4,3\rangle$	$\lvert 5,3\rangle$	662	3.526	6.27	17	6
$\lvert 6,1\rangle$	$\lvert 7,1\rangle$	698	5.755	2.00	66	4
$\lvert 5,2\rangle$	$\lvert 6,2\rangle$	802	4.765	3.88	38	5
$\lvert 4,4\rangle$	$\lvert 5,4\rangle$	845	2.721	8.63	12	6
$\lvert 5,5\rangle$	$\lvert 6,5\rangle$	1011	3.905	8.65	80	5
$\lvert 7,1\rangle$	$\lvert 8,1\rangle$	1140	6.440	2.26	4504	3
$\lvert 5,3\rangle$	$\lvert 6,3\rangle$	1164	4.289	5.94	Large	5
$\lvert 6,6\rangle$	$\lvert 7,6\rangle$	1180	4.868	8.99	450	5
$\lvert 6,2\rangle$	$\lvert 7,2\rangle$	1308	5.481	4.00	161	4
$\lvert 7,7\rangle$	$\lvert 8,7\rangle$	1348	5.710	9.52	18	4
$\lvert 5,4\rangle$	$\lvert 6,4\rangle$	1470	3.412	8.25	17	5
$\lvert 8,8\rangle$	$\lvert 9,8\rangle$	1513	6.460	10.2	3	3
$\lvert 6,6\rangle$	$\lvert 7,5\rangle$	1564	3.161	8.28	26	5
$\lvert 6,5\rangle$	$\lvert 7,5\rangle$	1646	4.646	8.33	49	5
$\lvert 9,9\rangle$	$\lvert 10,9\rangle$	1667	7.128	10.9	6	2
$\lvert 8,1\rangle$	$\lvert 9,1\rangle$	1717	7.067	2.66	1126	2
$\lvert 7,6\rangle$	$\lvert 8,6\rangle$	1786	5.589	8.78	3	5
$\lvert 10,10\rangle$	$\lvert 11,10\rangle$	1799	7.715	11.7	Large	1
$\lvert 6,3\rangle$	$\lvert 7,3\rangle$	1819	4.959	6.06	102	4
$\lvert 8,7\rangle$	$\lvert 9,7\rangle$	1909	6.389	9.41	1	4
$\lvert 7,7\rangle$	$\lvert 8,6\rangle$	1951	3.871	8.83	94	4
$\lvert 7,2\rangle$	$\lvert 8,2\rangle$	1968	6.132	4.34	1126	3
$\lvert 6,5\rangle$	$\lvert 7,4\rangle$	1968	2.360	7.91	Large	4

Table 7.2 "Magic" qubit pairs with one-photon transitions. The fourth column shows the qubit frequency. The fifth column shows the energy dependence of each state on the magnetic field at B_{magic}. The fifth column is the coherence time for a magnetic field noise of 10 mG. The sixth column shows the number of photons the qubits are away from either $|11,0\rangle$ or $|11,11\rangle$.

$\|F, m_F\rangle$	$\|F', m'_F\rangle$	B_{mag} (G)	$\Delta\nu_0$ (GHz)	$\frac{dU}{dB}$ (MHz/G)	$\tau(10^3$ s)	γ
$\|5,5\rangle$	$\|7,7\rangle$	3	10.94	10.9	94	4
$\|4,2\rangle$	$\|6,3\rangle$	100	9.390	5.38	23	5
$\|7,5\rangle$	$\|9,6\rangle$	206	13.72	7.76	141	5
$\|4,1\rangle$	$\|6,1\rangle$	275	9.259	1.88	27	5
$\|9,9\rangle$	$\|11,10\rangle$	286	16.03	11.4	102	1
$\|5,3\rangle$	$\|7,4\rangle$	348	10.89	6.31	17	4
$\|8,7\rangle$	$\|10,8\rangle$	349	14.93	9.68	23	3
$\|4,3\rangle$	$\|6,4\rangle$	454	9.058	7.14	141	5
$\|5,1\rangle$	$\|7,1\rangle$	486	10.78	1.86	21	4
$\|4,2\rangle$	$\|6,2\rangle$	543	8.803	3.76	94	5
$\|8,8\rangle$	$\|10,9\rangle$	551	14.86	10.8	375	2
$\|4,4\rangle$	$\|6,6\rangle$	560	9.172	10.1	47	5
$\|7,6\rangle$	$\|9,7\rangle$	703	13.61	9.10	450	4
$\|7,7\rangle$	$\|9,8\rangle$	736	13.48	10.2	24	3
$\|4,3\rangle$	$\|6,3\rangle$	798	7.976	5.66	281	5
$\|6,1\rangle$	$\|8,1\rangle$	825	12.21	2.02	60	3
$\|4,4\rangle$	$\|6,5\rangle$	839	8.066	8.66	28	5
$\|6,6\rangle$	$\|8,7\rangle$	842	11.92	9.60	Large	4

Table 7.3 "Magic" qubit pairs with two-photon transitions. The fourth column shows the qubit frequency. The fifth column shows the energy dependence of each state on the magnetic field at B_{magic}. The fifth column is the coherence time for a magnetic field noise of 10 mG. The sixth column shows the number of photons the qubits are away from either $|11,0\rangle$ or $|11,11\rangle$. Continued on next page in tab 7.4.

Since we pair the hyperfine states, we only consider changes in relative separation in pairs due to magnetic field noise. Ideally, we would find pairs $|0\rangle$ and $|1\rangle$ such that their energy levels respond identically at a "magic" magnetic field B_{mag}, i.e.

$$\left.\frac{dU_0}{dB}\right|_{B_{mag}} = \left.\frac{dU_1}{dB}\right|_{B_{mag}} . \tag{7.2}$$

It is not important to consider exactly what the qubit frequency is; as long as the separation is stable the experimental parameters can be adjusted to match it.

$\vert F, m_F\rangle$	$\vert F', m'_F\rangle$	B_{mag} (G)	$\Delta\nu_0$ (GHz)	$\frac{dU}{dB}$ (MHz/G)	$\tau(10^3$ s)	γ
$\vert 5,5\rangle$	$\vert 7,6\rangle$	874	10.14	9.06	Large	5
$\vert 5,2\rangle$	$\vert 7,2\rangle$	942	10.30	3.73	14	4
$\vert 4,2\rangle$	$\vert 6,1\rangle$	1035	7.416	2.03	51	5
$\vert 5,5\rangle$	$\vert 7,5\rangle$	1200	8.741	8.06	188	5
$\vert 4,3\rangle$	$\vert 6,2\rangle$	1215	6.221	4.00	563	5
$\vert 6,5\rangle$	$\vert 8,6\rangle$	1251	12.04	8.60	24	5
$\vert 7,1\rangle$	$\vert 9,1\rangle$	1316	13.52	2.34	141	2
$\vert 5,3\rangle$	$\vert 7,3\rangle$	1354	9.409	5.62	38	4
$\vert 6,6\rangle$	$\vert 8,6\rangle$	1368	10.55	8.64	38	5
$\vert 5,5\rangle$	$\vert 7,4\rangle$	1492	6.914	7.20	18	4
$\vert 6,2\rangle$	$\vert 8,2\rangle$	1501	11.67	3.97	161	3
$\vert 7,7\rangle$	$\vert 9,7\rangle$	1533	12.15	9.31	2	4
$\vert 8,8\rangle$	$\vert 10,8\rangle$	1689	13.58	10.0	1	3
$\vert 5,4\rangle$	$\vert 7,4\rangle$	1706	7.880	7.49	78	4
$\vert 5,2\rangle$	$\vert 7,1\rangle$	1751	8.206	2.47	102	4
$\vert 6,6\rangle$	$\vert 8,5\rangle$	1766	8.684	7.92	21	5
$\vert 9,9\rangle$	$\vert 11,9\rangle$	1825	14.84	10.8	35	2
$\vert 6,5\rangle$	$\vert 8,5\rangle$	1890	10.12	8.02	94	5
$\vert 8,1\rangle$	$\vert 10,1\rangle$	1905	14.72	2.77	281	1
$\vert 5,5\rangle$	$\vert 7,3\rangle$	1927	4.450	6.16	161	4
$\vert 5,3\rangle$	$\vert 7,2\rangle$	1974	6.870	4.34	125	4

Table 7.4 Continued from table 7.3. "Magic" qubit pairs with two-photon transitions. The fourth column shows the qubit frequency. The fifth column shows the energy dependence of each state on the magnetic field at B_{magic}. The fifth column is the coherence time for a magnetic field noise of 10 mG. The sixth column shows the number of photons the qubits are away from either $|11,0\rangle$ or $|11,11\rangle$.

The Zeeman effect in hyperfine states can be expressed in the coupled angular momentum basis. In this basis eq. 7.1 is expressed as

$$H_Z = -\overrightarrow{\boldsymbol{\mu}} \cdot \overrightarrow{\mathbf{B}} = \mu_B(g_J\hat{\mathbf{J}} + g_I\hat{\mathbf{I}}) \cdot \overrightarrow{\mathbf{B}}. \tag{7.3}$$

g_j and g_I have been measured to be 1.1951429(25) and $-6.423(42) \times 10^{-4}$ in holmium, respectively[119]. The matrix elements are therefore given by

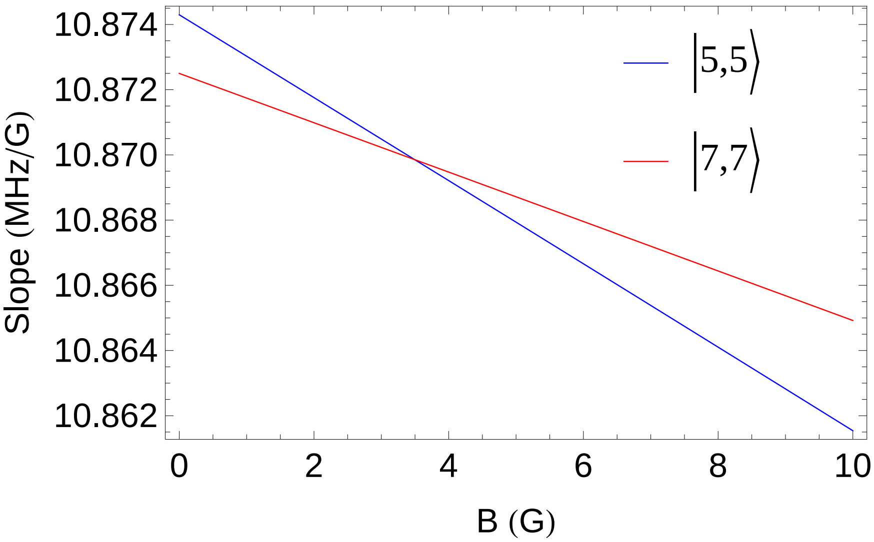

Figure 7.1 The slopes of a pair of hyperfine states as a function of the magnetic field. This pair is interesting because of its low field requirements.

$$U = \langle JI; F'm'_F | H_{HFS} + H_Z | JI; Fm_F \rangle \tag{7.4}$$

$$\langle JI; F'm'_F | H_{HFS} | JI; Fm_F \rangle = \frac{1}{2} AK + \frac{\frac{3}{2}K(K+1) - 2I(I+1)J(J+1)}{2I(2I-1)2J(2J-1)} \tag{7.5}$$

$$\langle JI; F'm'_F | H_Z | JI; Fm_F \rangle = \mu_B B_z g_F m_F \tag{7.6}$$

$$= \mu_B B_z \sum_{m_J m_I} C^{F'm'_F}_{Jm_J I m_I} C^{Fm_F}_{Jm_J I m_I} (g_J m_J + g_I m_I). \tag{7.7}$$

where $K = F(F+1) - I(I+1) - J(J+1)$ and C represents Clebsch-Gordan coefficients. We can find complicated analytic solutions to the eigenvalues of this Hamiltonian as a function of B_z. From there, we can find the first derivative of their magnetic energies. The identities of each state are also easily resolved. In the weak-field regime the perturbations to the hyperfine energies are linear in both B_z and m_F, so their ordering can be deduced by simply solving the eigenvalues for a small B_z of 1 G. After identification, we solve for the magnetic field at which each pair of hyperfine states have the same first derivative, restricting our search to pairs with $m_F > 0$ that are within a two-photon transition from each other and are magic at a $0 < B_z < 2000$ G, a reasonable experimental range for magnetic fields. We would also prefer states that are near to a state that is easily optically pumped like $|11, 11\rangle$ or $|11, 0\rangle$. This is to minimize the error rates in initializing the states.

We find a large list of possible qubit states (tables 7.2 and 7.3). The most notable pair is $|5, 5\rangle$ and $|7, 7\rangle$. We predict that these two states will be magic at a very modest field of 3.4 G. A non-zero magnetic field is desirable because it prevents spin-flips to degenerate states. At this magnetic field, the qubit frequency is 10.94 GHz. This pair is also only 4 transitions away from $|11, 11\rangle$ and is therefore one of the easier pairs to access from an optically pumped sample. We can estimate the coherence time τ_B of this pair by calculating the sensitivity of its qubit frequency $\Delta\nu_0(B)$ to a magnetic field noise of magnitude ϵ.

$$\tau_B = \left| \frac{1}{\Delta\nu_0(B_{mag} + \epsilon) - \Delta\nu_0(B_{mag} - \epsilon)} \right| \tag{7.8}$$

For the $|5, 5\rangle$ and $|7, 7\rangle$ pair, we find that the coherence time due to a manageable magnetic field noise of ±10 mG is 94000 s. In general, the coherence time under such conditions is very long. A complete list of magic qubit pairs under 2000 G and their coherence times with ±10 mG of magnetic field noise is shown in tables 7.2, 7.3, and 7.4. They show that holmium's rich atomic structure allows some flexibility if one set of states or magnetic fields proves to be inconvenient for some reason. This is a good argument for uses holmium as a single-atom qubit.

7.3 Blackbody Shifts in Holmium

Just as energy levels can be shifted by an applied AC electric field from a focused laser, so can they be affected by background blackbody radiation (BBR). It is important to understand these shifts for research involving precision measurement, such as quantum information or atomic clocks. Experimentally, blackbody radiation shifts can be difficult to predict or control for without the use of cryogens. It is therefore desirable to use states that are insensitive to BBR (i.e. $\delta\nu_{BBR}/\nu_0$ is small). The AC Stark shift is the same as previously stated.

$$\delta\nu = -\frac{1}{2}\frac{\alpha|\varepsilon|^2}{h} \tag{7.9}$$

The electromagnetic power radiated from a blackbody is given by the Stefan-Boltzmann law.

$$P_{rad} \propto T^4 \tag{7.10}$$

Because no body can exist at a temperature of absolute zero, any environment will emit some form of EM radiation. Our experiment runs at room temperature and is therefore subjected to a bath of thermal EM fields that may shift its hyperfine levels. This can be a problem for atomic clocks if the experiments are maintained if an environment without full temperature stability as fluctuations in temperature may cause fluctuations in the clock state frequencies. Because of this, candidates for frequency standards can be characterized by a stability constant β such that [120]

$$\frac{\delta\nu_{clock}}{\nu_{clock}} = \beta T^4. \tag{7.11}$$

The current standard for the second is defined by the separation of cesium's ground state hyperfine levels with $\beta = -17 \times 10^{-15}$ (Tab. 7.3)[121]. Proposed replacements include Al$^+$ with $\beta = -3.8 \times 10^{-18}$. While it is less important for quantum information, the estimation of β is still interesting for the purpose of establishing the stability of our quantum register.

To find the mean electric field of BBR, we refer to Planck's Law. The energy density as a function of ω for a blackbody is given by

$$\rho(\omega, T) = \frac{\hbar\omega^3}{4\pi^3 c^2} \frac{1}{e^{\hbar\omega/k_B T} - 1}. \tag{7.12}$$

Integrating over all frequency space to obtain the total energy per unit volume and equating it to the energy density of an electromagnetic wave $\rho_{EM} = \frac{\epsilon_0}{4} \langle\varepsilon^2\rangle$ predicts a mean electric field of $\langle\varepsilon^2\rangle = (831.9\text{V/m})^2$. Inserting $\langle\varepsilon^2\rangle$ into equation 7.9 gives

$$\delta\nu = -\frac{1}{2}(831.9\text{V/m})^2 \left(\frac{T(\text{K})}{300}\right)^4 \alpha. \tag{7.13}$$

As stated in chapter 5, the scalar polarizability of $\alpha_0 = \alpha_{0,F}$, so the shifts should be identical for two hyperfine levels. However, the contribution to the shift from the tensor polarizability α_2 changes with F. We can use the tensor polarizabilities found in chapter 5 to estimate the BBR

Element	Transition	β
Rb	$5s(F=1 \to F=2)$	1.25×10^{-14} [122]
Cs	$6s(F=3 \to F=4)$	1.7×10^{-14} [123]
Sr	$5s^2(^1\mathrm{S}_0) \to 5s5p(^3\mathrm{P}_0)$	-2.6×10^{-16} [124]
Yb	$6s^2(^1\mathrm{S}_0) \to 6s6p(^3\mathrm{P}_0)$	-5.5×10^{-15} [124]
Al^+	$3s^2(^1\mathrm{S}_0) \to 3s3p(^3\mathrm{P}_0)$	-3.8×10^{-18} [125]
Ho	$6s^2(F=4 \to F=5)\{F=4 \to F=6\}$	$3.6 \times 10^{-13}\{2.3 \times 10^{-13}\}$
Ho	$6s^2(F=5 \to F=6)\{F=5 \to F=7\}$	$1.2 \times 10^{-13}\{8.1 \times 10^{-14}\}$
Ho	$6s^2(F=6 \to F=7)\{F=6 \to F=8\}$	$4.8 \times 10^{-14}\{3.5 \times 10^{-14}\}$
Ho	$6s^2(F=7 \to F=8)\{F=7 \to F=9\}$	$2.2 \times 10^{-14}\{1.7 \times 10^{-14}\}$
Ho	$6s^2(F=8 \to F=9)\{F=8 \to F=10\}$	$1.2 \times 10^{-14}\{9.0 \times 10^{-15}\}$
Ho	$6s^2(F=9 \to F=10)\{F=9 \to F=11\}$	$6.5 \times 10^{-15}\{5.2 \times 10^{-15}\}$
Ho	$6s^2(F=10 \to F=11)$	3.9×10^{-15}

Table 7.5 Predicted β for a variety of elements. All values are theoretical except for Cs.

shift. At room temperature 300 K, the peak emission wavelength of the Planck distribution is 10.8 μm, far into the DC limit for any transitions from the ground state of holmium and so we can use the DC limit of $\alpha_{2,F}$.

In table 7.3 we summarize the BBR shift relative to possible hyperfine pairs (i.e. pairs of hyperfine states with $\Delta F \leq 2$) as β. We predict a wide range of stability constants, some of which compare favorably even to the cesium standard. The table includes Yb and Sr because their atomic structure is most similar to Ho of the β that have been predicted, though their clock transitions are in the optical rather than RF range. They both have closed s-shells. Al^+ is included as the clock proposal most robust against BBR shifts.

These calculations show that certain pairs of holmium states are very stable against BBR shifts but this should not be interpreted as reason to consider it as an atomic clock candidate. One reason is that the uncertainty in these calculations is as important as the values of β themselves. The uncertainty is our calculations are very large compared to others that take into account higher order processes [121]. Whereas the alkalis and alkali earths have fairly simple spectra, the spectrum of holmium has also not been completely characterized, lending much uncertainty to the value of α. We have also not included any estimates on the quality of holmium based on its transition widths or frequencies.

Our calculations show that the BBR shift should not be a problem in our experiment. We do not need to take any special precautions in dealing with them in either the ensemble or single-atom schemes that we have proposed for quantum computing with holmium.

7.4 Conclusion

In this chapter, we have presented many arguments and calculations demonstrating holmium's suitability for single-atom quantum information experiments. With some of these calculations we found interesting properties of some of the rare earths that may pose interesting avenues of research in the future. It has, at the very least, been shown that experiments with rare earths are still in their infancy and hold much promise for the future.

Chapter 8

Concluding Remarks

In this thesis, we have presented the first steps towards performing quantum information processes with collective holmium ensembles. We have prepared an experimental apparatus that has been shown to be successful at cooling and trapping holmium in a MOT, something that has never before been achieved. From this, we have been able to perform many other measurements in preparation for future coherent operations on our holmium ensemble. We measured 165 Rydberg states that we will be able to choose from when we begin Rydberg blockade experiments. This information is complete enough that we are able to experimentally determine the quantum defects for the s and d states of holmium and refine the measurement of the ionization potential of holmium by several orders of magnitude. This work also allows us to estimate the blockade strength of the ns series in our ensemble.

We have made solid steps towards dipole trapping of holmium. The creation of holmium is an ODT is the next logical step and may lead directly to coherent operations on an ensemble. We have well-characterized our experimental trap parameters and estimated our trap depths using atomic polarizability calculations. Our imaging optics have been built so that we should be able to perform single-atom imaging on our holmium ODT. We have identified several challenges in our experimental setup and to optically trapping holmium in particular, such as the difficulty of preventing hyperfine changing collisions in our ODT. These challenges are not insurmountable and we have proposed several methods of overcoming them.

In addition to these experimental achievements, we have performed many exploratory calculations that demonstrate fertile ground for future experiments. We have used the Cowan Code to suggest many narrow-line MOTs that may improve the temperature of our atoms before loading into an ODT. Single atom trapping seems very achievable with our atomic species. We are in good standing to attempt Rydberg blockade in our sample in our future and have identified many possible state pairs that would be suitable for initial forays into single-qubit or two-qubit gates. Our current experimental apparatus has been very successful but we have identified many improvements that can be made. We have proposed several experimental upgrades to our vacuum chamber that will improve stability and performance over the coming years to allow us to achieve these more ambitious goals. These include incorporating several cutting edge techniques that will move our field forward.

Our work has been shown to be applicable to a much larger scope of experiments than we had previously expected. We have suggested several different routes that future experimenters could take in research involving single neutral atoms.

Experiments in holmium demonstrate great promise for the future. There is still much work to be done and we are in good standing to achieve much more using this work as a foundation.

LIST OF REFERENCES

[1] G. Nave, “Atomic transition rates for neutral holmium (hoi),” *J. Opt. Soc. Am. B*, vol. 20, pp. 2193–2202, Oct 2003.

[2] M. Saffman, T. G. Walker, and K. Mølmer, “Quantum information with rydberg atoms,” *Rev. Mod. Phys.*, vol. 82, pp. 2313–2363, Aug 2010.

[3] U. Fano, C. Theodosiou, and J. Dehmer, “Electron-optical properties of atomic fields,” *Rev. Mod. Phys*, vol. 48, no. 49, 1976.

[4] T. Ladd, F. Jelezko, R. Laflamme, Y. Nakamura, C. Monroe, and J. O’Brien, “Quantum computers,” *Nature*, vol. 464, pp. 45–53, 2010.

[5] P. Kok, W. Munro, K. Nemoto, T. Ralph, J. Dowling, and G. Milburn, “Linear optical quantum computing with photonic qubits,” *Rev. Mod. Phys.*, vol. 79, no. 135, 2007.

[6] D. Loss and D. DiVincenzo, “Quantum computation with quantum dots,” *Phys. Rev. A*, vol. 57, no. 1, 1998.

[7] J. Clarke and F. K. Wilhelm, “Superconducting quantum bits,” *Nature*, vol. 453, pp. 1031–1042, 2008.

[8] H. Häffner, C. Roos, and R. Blatt, “Quantum computing with trapped ions,” *Phys. Rep.*, vol. 469, no. 4, 2008.

[9] J. Weber, W. Koehl, J. Varley, A. Janotti, B. Buckley, C. V. de Walle, and D. Awschalom, “Quantum computing with defects,” *Proc. Natl. Acad. Sci. USA*, vol. 107, no. 19, pp. 8513–8518, 2010.

[10] D. Jaksch, J. I. Cirac, P. Zoller, S. L. Rolston, R. Côté, and M. D. Lukin, “Fast quantum gates for neutral atoms,” *Phys. Rev. Lett.*, vol. 85, pp. 2208–2211, Sep 2000.

[11] D. Yavuz, P. Kulatunga, E. Urban, T. Johnson, N. Proite, T. Henage, T. Walker, and M. Saffman, “Fast ground state manipulation of neutral atoms in microscopic optical traps,” *Phys. Rev. Lett.*, vol. 96, no. 063001, 2006.

[12] L. Isenhower, E. Urban, X. Zhang, A. Gill, T. Henage, T. Johnson, T. Walker, and M. Saffman, “Demonstration of a neutral atom controlled-not quantum gate,” *Phys. Rev. Lett.*, vol. 104, no. 010503, 2010.

[13] X. Zhang, L. Isenhower, A. Gill, T. Walker, and M. Saffman, “Determistic entanglement of two neutral atoms via rydberg blockade,” *Phys. Rev. A*, vol. 82, no. 030306, 2010.

[14] K. Maller, M. Lichtman, T. Xia, Y. Sun, M. Piotrowicz, A. Carr, L. Isenhower, and M. Saffman, “Rydberg-blockade controlled-not gate and entanglement in a two-dimensional array of neutral-atom qubits,” *Phys. Rev. A*, vol. 92, no. 022336, 2015.

[15] K. Nelson, X. Li, and D. Weiss, “Imaging single atoms in a three-dimensional array,” *Nature Phys.*, vol. 3, pp. 556–560, 2007.

[16] M. Ebert, M. Kwon, T. G. Walker, and M. Saffman, “Coherence and rydberg blockade of atomic ensemble qubits,” *Phys. Rev. Lett.*, vol. 115, p. 093601, Aug 2015.

[17] M. D. Lukin, M. Fleischhauer, R. Cote, L. M. Duan, D. Jaksch, J. I. Cirac, and P. Zoller, “Dipole blockade and quantum information processing in mesoscopic atomic ensembles,” *Phys. Rev. Lett.*, vol. 87, p. 037901, Jun 2001.

[18] M. Saffman and K. Mølmer, “Scaling the neutral-atom rydberg gate quantum computer by collective encoding in holmium atoms,” *Phys. Rev. A*, vol. 78, p. 012336, Jul 2008.

[19] S. Kim, R. R. Mcleod, M. Saffman, and K. H. Wagner, “Doppler-free, multiwavelength acousto-optic deflector for two-photon addressing arrays of rb atoms in a quantum information processor,” *Appl. Opt.*, vol. 47, pp. 1816–1831, Apr 2008.

[20] T. Xia, M. Lichtman, K. Maller, A. W. Carr, M. J. Piotrowicz, L. Isenhower, and M. Saffman, “Randomized benchmarking of single-qubit gates in a 2d array of neutral-atom qubits,” *Phys. Rev. Lett.*, vol. 114, p. 100503, Mar 2015.

[21] W. Dür, G. Vidal, and J. I. Cirac, “Three qubits can be entangled in two inequivalent ways,” *Phys. Rev. A*, vol. 62, p. 062314, Nov 2000.

[22] E. Brion, L. H. Pedersen, M. Saffman, and K. Mølmer, “Error correction in ensemble registers for quantum repeaters and quantum computers,” *Phys. Rev. Lett.*, vol. 100, p. 110506, Mar 2008.

[23] N. Q. Burdick, K. Baumann, Y. Tang, M. Lu, and B. L. Lev, “Fermionic suppression of dipolar relaxation,” *Phys. Rev. Lett.*, vol. 114, p. 023201, Jan 2015.

[24] E. L. Raab, M. Prentiss, A. Cable, S. Chu, and D. E. Pritchard, “Trapping of neutral sodium atoms with radiation pressure,” *Phys. Rev. Lett.*, vol. 59, pp. 2631–2634, Dec 1987.

[25] K. Honda, Y. Takahashi, T. Kuwamoto, M. Fujimoto, K. Toyoda, K. Ishikawa, and T. Yabuzaki, "Magneto-optical trapping of yb atoms and a limit on the branching ratio of the $^1P_1$ state," *Phys. Rev. A*, vol. 59, pp. R934–R937, Feb 1999.

[26] J. J. McClelland and J. L. Hanssen, "Laser cooling without repumping: A magneto-optical trap for erbium atoms," *Phys. Rev. Lett.*, vol. 96, p. 143005, Apr 2006.

[27] M. Lu, S. H. Youn, and B. L. Lev, "Trapping ultracold dysprosium: A highly magnetic gas for dipolar physics," *Phys. Rev. Lett.*, vol. 104, p. 063001, Feb 2010.

[28] D. Sukachev, A. Sokolov, K. Chebakov, A. Akimov, S. Kanorsky, N. Kolachevsky, and V. Sorokin, "Magneto-optical trap for thulium atoms," *Phys. Rev. A*, vol. 82, p. 011405, Jul 2010.

[29] J. Miao, J. Hostetter, G. Stratis, and M. Saffman, "Magneto-optical trapping of holmium atoms," *Phys. Rev. A*, vol. 89, no. 041401, 2014.

[30] B. Hemmerling, G. K. Drayna, E. Chae, A. Ravi, and J. M. Doyle, "Buffer gas loaded magneto-optical traps for yb, tm, er and ho," *New Journal of Physics*, vol. 16, no. 6, p. 063070, 2014.

[31] H. Lu, I. Kozyryev, B. Hemmerling, J. Piskorski, and J. Doyle, "Magnetic trapping of molecules via optical loading and magnetic slowing," *Phys. Rev. Lett.*, vol. 112, p. 113006, Mar 2014.

[32] A. Frisch, K. Aikawa, M. Mark, F. Ferlaino, E. Berseneva, and S. Kotochigova, "Hyperfine structure of laser-cooling transitions in fermionic erbium-167," *Phys. Rev. A*, vol. 88, p. 032508, Sep 2013.

[33] M. Lu, N. Q. Burdick, S. H. Youn, and B. L. Lev, "Strongly dipolar bose-einstein condensate of dysprosium," *Phys. Rev. Lett.*, vol. 107, p. 190401, Oct 2011.

[34] D. Steck, "Rubidium 85 d line data," 9 2013. available online at http://steck.us/alkalidata.

[35] D. Steck, "Rubidium 85 d line data," 10 2003. available online at http://steck.us/alkalidata.

[36] D. Steck, "Cesium d line data," 12 2010. available online at http://steck.us/alkalidata.

[37] D. Das, S. Barthwal, A. Banerjee, and V. Natarajan, "Absolute frequency measurements in yb with 0.08 ppb uncertainty: Isotope shifts and hyperfine structure in the 399-nm $^1s_0 \rightarrow ^1 p_1$ line," *Phys. Rev. A*, vol. 72, p. 032506, Sep 2005.

[38] M. Lu, S. H. Youn, and B. L. Lev, "Spectroscopy of a narrow-line laser-cooling transition in atomic dysprosium," *Phys. Rev. A*, vol. 83, p. 012510, Jan 2011.

[39] M. N. Reddy, S. A. Ahmad, and G. N. Rao, "Laser optogalvanic spectroscopy of holmium," *J. Opt. Soc. Am. B*, vol. 9, pp. 22–26, Jan 1992.

[40] J. Wyart, P. Camus, and J. Vergés, “Etude du spectre de l’holmium atomique: I. spectre d’emission infrarouge niveaux d’émission infrarouge niveaux d’énergie de ho i et structures hyperfines,” *Physica B+C*, vol. 92, no. 3, pp. 377–296, 1977.

[41] S. Kröger, J.-F. Wyart, and P. Luc, “Theoretical interpretation of hyperfine structures in doubly-excited configurations 4f 10 5d6s6p and 4f 10 5d 2 6s and new energy levels in neutral holmium (ho i),” *Physica Scripta*, vol. 55, no. 5, p. 579, 1997.

[42] A. Frisch, K. Aikawa, M. Mark, A. Rietzler, J. Schindler, E. Zupanič, R. Grimm, and F. Ferlaino, “Narrow-line magneto-optical trap for erbium,” *Phys. Rev. A*, vol. 85, p. 051401, May 2012.

[43] G. A. Vishnyakova, E. S. Kalganova, D. D. Sukachev, S. A. Fedorov, A. V. Sokolov, A. V. Akimov, N. N. Kolachevsky, and V. N. Sorokin, “Two-stage laser cooling and optical trapping of thulium atoms,” *Laser Physics*, vol. 24, p. 074018, July 2014.

[44] T. Kuwamoto, K. Honda, Y. Takahashi, and T. Yabuzaki, “Magneto-optical trapping of yb atoms using an intercombination transition,” *Phys. Rev. A*, vol. 60, pp. R745–R748, Aug 1999.

[45] W. A. van Wijngaarden and J. Li, “Measurement of isotope shifts and hyperfine splittings of ytterbium by means of acousto-optic modulation,” *J. Opt. Soc. Am. B*, vol. 11, pp. 2163–2166, Nov 1994.

[46] A. J. Berglund, J. L. Hanssen, and J. J. McClelland, “Narrow-line magneto-optical cooling and trapping of strongly magnetic atoms,” *Phys. Rev. Lett.*, vol. 100, p. 113002, Mar 2008.

[47] R. Maruyama, *Optical Trapping of Ytterbium Atoms*. PhD thesis, University of Washington, 5 2003.

[48] S. B. Hill and J. J. McClelland, “Atoms on demand: Fast, deterministic production of single cr atoms,” *Applied Physics Letters*, vol. 82, no. 18, 2003.

[49] G. F. Wakefield, A. H. Daane, and F. Spedding, “Vapor pressure of holmium,” *Journal of Chemical Physics*, vol. 47, no. 12, pp. 4994–4999, 1967.

[50] J. Schindler, “Characterization of erbium atomic beam,” Master’s thesis, University of Innsbruck, 7 2011.

[51] J. Miao, *Laser cooling and Magneto-Optical Trapping of Holmium Atoms*. PhD thesis, University of Wisconsin-Madison, 8 2013.

[52] Sanyo, *Laser Diode*, 11 2007.

[53] N. E. Alloys, “Invar properties and low coefficient of expansion.” `http://www.nealloys.com/invar_invar.php`. Accessed online, Mar. 15 2016.

[54] Arroyo, *TECSource 5240 User's Manual*, 2 2011.

[55] M. Lichtman, *Coherent Operations, Entanglement, and Progress Toward Quantum Search in a Large 2D Array of Neutral Atom Qubits*. PhD thesis, University of Wisconsin-Madison, 8 2015.

[56] National Instruments, *User Manual: NI-2163B*, 11 2007.

[57] National Instruments, *BNC2090A User Manual*, 1 2007.

[58] Analog Devices, *AD9910 Datasheet*, 2007.

[59] L. Goodman, H. Kopfermann, and K. Schlümann, "Drehimpulsquantenzahl und hyperfeinstrukturaufspaltung des grundzustandes im ho165 i-spektrum," *Naturwissenschaften*, vol. 49, no. 5, pp. 101–102, 1962.

[60] J. Dalibard and C. Cohen-Tannoudji, "Laser cooling below the doppler limit by polarization gradients: simple theoretical models," *J. Opt. Soc. Am. B*, vol. 6, pp. 2023–2045, Nov 1989.

[61] S. H. Youn, M. Lu, and B. L. Lev, "Anisotropic sub-doppler laser cooling in dysprosium magneto-optical traps," *Phys. Rev. A*, vol. 82, p. 043403, Oct 2010.

[62] D. Sesko, T. Walker, C. Monroe, A. Gallagher, and C. Wieman, "Collisional losses from a light-force atom trap," *Phys. Rev. Lett.*, vol. 63, pp. 961–964, Aug 1989.

[63] J. E. Bjorkholm, "Collision-limited lifetimes of atom traps," *Phys. Rev. A*, vol. 38, pp. 1599–1600, Aug 1988.

[64] T. Loftus, J. R. Bochinski, R. Shivitz, and T. W. Mossberg, "Power-dependent loss from an ytterbium magneto-optic trap," *Phys. Rev. A*, vol. 61, p. 051401, Apr 2000.

[65] A. Frisch, K. Aikawa, M. Mark, A. Rietzler, J. Schindler, E. Zupanič, R. Grimm, and F. Ferlaino, "Narrow-line magneto-optical trap for erbium," *Physical Review A*, vol. 85, no. 051401, 2012.

[66] R. D. Cowan, *The Theory of Atomic Structure and Spectra*. University of California Press, Ltd., 1981.

[67] P. Quineta, P. Palmeria, and E. Biémont, "On the use of the cowan's code for atomic structure calculations in singly ionized lanthanides," *J. Quant. Spectrosc. R. A.*, vol. 62, no. 5, pp. 625–646, 1976.

[68] A. Kramida, Yu. Ralchenko, J. Reader, and and NIST ASD Team. NIST Atomic Spectra Database (ver. 5.3), [Online]. Available: `http://physics.nist.gov/asd` [2016, March 10]. National Institute of Standards and Technology, Gaithersburg, MD., 2015.

[69] E. Worden, R. Solarz, J. Paisner, and J. Conway, "First ionization potentials of lanthanides by laser spectroscopy," *J. Opt. Soc. Am.*, vol. 68, no. 52, 1978.

[70] N. Erdmann, M. Nunnemann, K. Eberhardt, G. Herrmann, G. Huber, S. Köhler, J. Kratz, G. Passler, J. Peterson, N. Trautmann, and A. Waldek, "Determination of the first ionization potential of nine actinide elements by resonance ionization mass spectroscopy (rims)," *J. Alloys Compd.*, vol. 271-273, no. 837, 1998.

[71] P. Xue, X. Xu, W. Huang, C. Xu, R. Zhao, and X. Xie, "Observation of the highly excited states of lanthanum," *AIP Conf. Proc.*, vol. 388, no. 299, 1997.

[72] S. Nakhate, M. Razvi, J. Connerade, and S. Ahmad, "Investigation of rydberg states of the europium atom using resonance ionization spectroscopy," *J. Phys. B*, vol. 33, no. 5191, 2000.

[73] X. Xu, H. Zhou, W. Huang, and D. Chen, "Rims studies of high rydberg and autoionizing states of the rare-earth element dy," *Inst. Phys. Conf. Ser.*, vol. 128, no. 71, 1992.

[74] Y. Ogawa and O. Kujirai, "Study of even-parity autoionization states of lutetium atom by atomic beam laser resonance ionization spectroscopy," *J. Phys. Soc. Jpn.*, vol. 68, no. 428, 1999.

[75] M. Miyabe, M. Oba, and I. Wakaida, "Analysis of the even-parity rydberg series of gd i to determine its ionization potential and isotope shift," *J. Phys. B*, vol. 31, no. 4559, 1998.

[76] T. Jayasekharan, M. Razvi, and G. Bhale, "Even-parity bound and autoionizing rydberg series of the samarium atom," *J. Phys. B*, vol. 33, no. 3123, 2000.

[77] E. Vidolova-Angelova, G. I. Bekov, L. N. Ivanov, V. Fedoseev, and A. A. Atakhadjaev, "Laser spectroscopy investigation of highly excited states of the tm atom," *J. Phys. B*, vol. 17, no. 953, 1984.

[78] E. P. Vidolova-Angelova, T. B. Krustev, D. A. Angelov, and S. Mincheva, "Laser resonance ionization spectroscopy of the cerium atom," *J. Phys. B*, vol. 30, no. 667, 1997.

[79] P. Camus, A. Débarre, and C. Morillon, "Highly excited levels of neutral ytterbium. i. two-photon and two-step spectroscopy of even spectra," *J. Phys. B*, vol. 13, no. 1073, 1980.

[80] J. Roßnagel, S. Raeder, A. Hakimi, R. Ferrer, N. Trautmann, and K. Wendt, "Determination of the first ionization potential of actinium," *Phs. Rev. A*, vol. 85, no. 012525, 2012.

[81] E. F. Worden, L. R. Carson, S. A. Johnson, J. A. Paisner, and R. W. Solarz, "Ionization potential of neutral atomic plutonium determined by laser spectroscopy," *J. Opt. Soc. Am. B*, vol. 10, no. 1998, 1993.

[82] R. W. Solarz, C. A. May, L. R. Carson, E. F. Worden, S. A. Johnson, J. A. Paisner, , and J. L. J. Radzeimski, “Detection of rydberg states in atomic uranium using time-resolved stepwise laser photoionization,” *Phys. Rev. A*, vol. 14, no. 1129, 1976.

[83] T. F. Gallagher, *Rydberg Atoms*. Cambridge University Press, 1994.

[84] J. Lawler, “Improved atomic data for ho ii and new holmium abundances for the sun and three metal-poor stars,” *Astrophys. J. Lett.*, vol. 604, no. 850, 2004.

[85] W. Darkwort, J. Ferch, and H. Gebauer, “Hexadecapole interaction in the atomic ground state of165ho,” *Z. Phys. A*, vol. 267, no. 229, 1974.

[86] B. Burghardt, S. Buttgenbach, N. Glaeser, R. Harzer, G. Meisel, B. Roski, and F. Träber, “Hyperfine structure measurements in metastable states of165ho,” *Z. Phys. A*, vol. 307, 1982.

[87] E. F. Worden, R. W. Solarz, J. A. Paisner, and J. G. Conway, “First ionization potentials of lanthanides by laser spectroscopy,” *J. Opt. Soc. Am.*, vol. 68, no. 52, 1978.

[88] M. Seaton, “Quantum defect theory,” *Rep. Prog. Phys.*, vol. 46, no. 167, 1983.

[89] M. Aymar, C. H. Greene, and E. Luc-Koenig, “Multichannel rydberg spectroscopy of complex atoms,” *Rev. Mod. Phys.*, vol. 68, no. 1015, 1996.

[90] K. Singer, J. Stanojevic, M. Weidermüller, and R. Côté, “Long-range interactions between alkali rydberg atom pairs correlated to the ns-ns,npnp ad nd-nd asymptotes,” *Journal of Physics B:Atomic Molecular and Optical Physics*, vol. 38, pp. S295–S307, 2005.

[91] T. G. Walker and M. Saffman, “Consequences of zeeman degeneracy for the van der waals blockade between rydberg atoms,” *Phys. Rev. A*, vol. 77, no. 032723, 2008.

[92] B. Kaulakys, “Consistent analytical approach for the quasi-classical radial dipole matrix elements,” *Journal of Physics B:Atomic Molecular and Optical Physics*, vol. 28, no. 4963, 1995.

[93] W. C. Martin, R. Zalubas, and L. Hagan, *Atomic Energy Levels-The Rare-Earth Elements*. U.S. Government Printing Office, 1978.

[94] S. Kröger, J. Wyart, and P. Luc, “Theoretical interpretation of hyperfine structures in doubly-excited configurations 4f105d6s6p and 4f105d26s and new energy levels in neutral holmium (ho i),” *Phys. Scr.*, vol. 55, no. 579, 1997.

[95] R. Grimm, M. Weirdemüller, and Y. B. Ovchinnikov, “Optical dipole traps for neutral atoms,” in *Advances in Atomic, Molecular, and Optical Physics* (E. Arimondo, C. C. Lin, and S. F. Yelin, eds.), pp. 95–170, Elsevier Inc., 2000.

[96] M. J. Piotrowisz, M. Lichtman, K. Mallar, G. Li, S. Zhang, L. Isenhower, and M. Saffman, “Two-dimensional lattice of blue-detuned atom traps using a projected gaussian beam array,” *Physical Review A*, vol. 88, no. 013420, 2013.

[97] G. Li, S. Zhang, L. Isenhower, K. Maller, and M. Saffman, “Crossed vortex bottle beam trap for single-atom qubits,” *Optics Letters*, vol. 37, no. 5, pp. 851–853, 2012.

[98] V. V. Ivanov, J. A. Isaacs, M. Saffman, S. A. Kemme, A. r. Ellis, G. R. Brady, J. R. Wendt, G. W. Biedermann, and S. Samora, “Atom trapping in a bottle beam created by a diffractive optical element,”

[99] G. A. Vishnyakova, E. S. Kalganova, D. D. Sukachev, S. A. Federov, A. V. Sokolov, A. V. Akimov, N. N. Kolachevsky, and V. N. Sorokin, “Two-stage laser cooling and optical trapping of thulium atoms,” *Laser Physics*, vol. 24, no. 129601, 2014.

[100] L.M., J. Indergaard, B. Zhang, I. Larkin, R. Moro, and W. de Heer, “Measured atomic ground-state polarizabilities of 35 metallic elements,” *Phys. Rev. A*, vol. 91, no. 010501, 2015.

[101] X. Chu, A. Dalgarno, and G. C. Gorenenboom, “Dynamic polarizabilities of rare-earth-metal atoms and dispersion coefficients for their interaction with helium atoms,” *Phys. Rev. A*, vol. 75, no. 032723, 2007.

[102] V. A. Dzuba, A. Kozlov, and V. V. Flambaum, “Scalar static polarizabilities of lanthanides and actinides,” *Physical Review A*, vol. 89, no. 042507, 2014.

[103] R. H. Rinkleff and F. Thorn, “On the tensor polarizabilities in the $4f^n6s^2$ ground levels of the neutral rare-earth atoms,” *Zeitschrift für Physik D*, vol. 32, pp. 173–177, 1994.

[104] S. Baier, “An optical dipole trap for erbium with tunable geometry,” Master’s thesis, University of Innsbruck, 10 2012.

[105] T. A. Savard, K. M. O’Hara, and J. E. Thomas, “Laser-noise-induced heating in far-off resonance optical traps,” *Phys. Rev. A*, vol. 56, pp. R1095–R1098, Aug 1997.

[106] M. Lu, N. Q. Burdick, and B. L. Lev, “Quantum degenerate dipolar fermi gas,” *Phys. Rev. Lett.*, vol. 108, p. 215301, May 2012.

[107] T. Fukuhara, Y. Yakasu, M. Kumakura, and Y. Takahasi, “Degenerate fermi gases of ytterbium,” *Physical Review Letters*, vol. 98, no. 030401, 2007.

[108] G. Stratis, “Constructing a zeeman slow using permanent magnets,” undergraduate honors thesis, University of Wisconsin-Madison, 5 2013.

[109] J. D. Ellis, “Uhv vacuum techniques: Basic concepts.” Accessed 2016-03-23.

[110] “Conductance calculations.” Accessed 2016-03-23.

[111] Kurt J. Lesker Company, *Flanges, Fittings, and Components*, 10 2009.

[112] J. Léonard, M. Lee, A. Morales, T. M. Karg, T. Esslinger, and T. Donner, "Optical transport and manipulation of an ultracold atomic cloud using focus-tunable lenses," *New Journal of Physics*, vol. 16, no. 9, p. 093028, 2014.

[113] Optotune AG, *Electrical Lens Driver 4 Manual*, 1 2016.

[114] G. Shortley and R. Weller, "The numerical solution of laplace's equation," *J. Appl. Phys.*, vol. 9, no. 334, 1938.

[115] M. Greiner, "The erbium microscope." Accessed 2016-04-3.

[116] CRC Handbook, *CRC Handbook of Chemistry and Physics, 88th Edition*. CRC Press, 88 ed., 2007.

[117] Y. Takasu, K. Honda, K. Komori, T. Kuwamoto, M. Kumakura, Y. Takahashi, and T. Yabuzaki, "High-density trapping of cold ytterbium atoms by an optical dipole force," *Phys. Rev. Lett.*, vol. 90, p. 023003, Jan 2003.

[118] S. Earnshaw, "On the nature of the molecular forces which regulate the constitution of the luminiferous ether," *Trans. Camb. Phil. Soc.*, vol. 7, p. 97–114, 1842.

[119] W. Dankwort and J. Ferch, "Reevaluation of the atomic gj-factor and the nuclear gi-factor of165ho," *Zeitschrift für Physik*, vol. 267, no. 3, pp. 239–241.

[120] W. M. Itano, L. L. Lewis, and D. J. Wineland, "Shift of $^2s_{\frac{1}{2}}$ hyperfine splittings due to blackbody radiation," *Phys. Rev. A*, vol. 25, pp. 1233–1235, Feb 1982.

[121] M. S. Safronova, M. G. Kozlov, and C. W. Clark, "Blackbody radiation shifts in optical atomic clocks," *IEEE Trans. Ultrason. Ferroelectr. Freq. Control*, vol. 59, pp. 439–447, March 2012.

[122] M. S. Safronova, D. Jiang, and U. I. Safronova, "Blackbody radiation shift in the $^{87}\mathrm{Rb}$ frequency standard," *Phys. Rev. A*, vol. 82, p. 022510, Aug 2010.

[123] E. Simon, P. Laurent, and A. Clairon, "Measurement of the stark shift of the cs hyperfine splitting in an atomic fountain," *Phys. Rev. A*, vol. 57, pp. 436–439, Jan 1998.

[124] S. G. Porsev and A. Derevianko, "Multipolar theory of blackbody radiation shift of atomic energy levels and its implications for optical lattice clocks," *Phys. Rev. A*, vol. 74, p. 020502, Aug 2006.

[125] M. S. Safronova, M. G. Kozlov, and C. W. Clark, "Precision calculation of blackbody radiation shifts for optical frequency metrology," *Phys. Rev. Lett.*, vol. 107, p. 143006, Sep 2011.

[126] W. Whaling, W. Anderson, M. Carle, J. Brault, and H. Zarem, “Argon i lines produced in a hollow cathode source, 332 nm to 5865 nm,” *J. Res. Natl. Inst. Stand. Technol.*, vol. 107, no. 149, pp. 149–169, 2002.

[127] R. C. M. Learner and A. P. Thorne, “Wavelength calibration of fourier-transform emission spectra with applications to fe i,” *J. Opt. Soc. Am. B*, vol. 5, no. 149, 1988.

Appendix A: ULE Cavities

A.1 Introduction

The M Squared SolsTiS Ti:Sa laser is locked to an ultra-low expansion (ULE) cavity with a PDH lock. ULE glass is a proprietary material made by Corning with a coefficient of thermal expansion of 10^{-8} 1/K. This makes it ideal as a reference cavity material.

A.1.1 Optical Setup

The SolsTiS has a glass slide pick off for its 821 nm light. One reflection off of the slide is used for wavelength measurement. The reflection is coupled into a fiber with its output coupled into a Photline NIR-MPX800-LN-05-P-P-FA-FA fiber EOM. This EOM has a very large bandwidth (> 4 GHz) and requires no RF amplifier to achieve good modulation. This feature allows two sets of sidebands to be easily put on the carrier. One set is used for the PDH lock and is tuned to maximize the phase matching for the lock, and one set is used to lock to any arbitrary frequency in the cavity's 1.5 GHz FSR. The modulated light is coupled into the ULE cavity in a PDH configuration.

A.1.2 Cavity Details

The reference cavity is made by Advanced Thin Films, model ATF-6020-4. The ULE spacer is 10 cm in length, yielding a FSR of 1.5 GHz. The cavity is made of two mirrors of reflectivity R=0.999984 with a finesse of $\sim$196000 and linewidth 7.6 kHz. These mirrors are optically contacted to the cavity in a slightly offset hemispherical configuration to give mode spacings of 220 MHz.

The cavity is contained in a vacuum can. The can is held at a pressure of 10^{-8} T to eliminate variations from humidity of pressure changes. The cavity is supported inside the can by two Viton o-rings at its Airy points to reduce length changes. These o-rings provide a thermal time constant of about 6 hours. The can is temperature stabilized by heater tape monitored and controlled by an Arroyo TECSource 5240, stable to ± 0.004 K.

A.1.3 Cavity Preparation

Alignment of high-finesse optical cavities is more difficult than medium- or low-finesse optical cavities. They require a special procedure:

1. The beam is emitted from a single-mode fiber so it should be a good TEM00 mode. Pick a suitable lens to achieve a waist size of 200 μm.

2. Make sure the beam is flat, straight, and at the same height as the center of the cavity. As is usual for a PDH lock, two mirrors and a PBS should be used.

3. Place the cavity with the flat mirror first so that the 200 μm waist is at the center of the flat mirror. A $\lambda/4$ waveplate should be placed before the cavity so that the reflection can either retroreflect along the beam path or be picked off by the PBS.

4. Retroreflect the beam off of the flat mirror.

5. Use as much optical power as is available. For the Photline NIR-MPX800-LN-05-P-P-FA-FA, the damage threshold is 20 mW into the fiber.

6. Ramp the laser frequency at 50-100 Hz. Look for peaks in the transmission signal. While adjusting the alignment, a large, low-frequency transmission signal may be seen. This is a signal that the beam is poorly aligned and has begun to resonate with the low-finesse etalon formed by the ULE spacer. It may be useful to double-check steps 3 and 4.

7. Walk the beam into the cavity using two mirrors. Maximize the transmission peaks. This can be very difficult because the filling and ring-down time of high-finesse cavities is long, so the peak height can vary wildly with each pass. This effect can be minimized with faster frequency ramping. It is possible to notice general trends in increasing or decreasing peak height until the TEM00 mode is obvious and easier to align.

8. Pick off the reflection with the PBS. Place a mirror to reflect the cavity back-reflection into the high-speed photodetector used for PDH locking. Maximize the signal with it and then connect it to the PDH electronics.

9. Once an error signal is seen, adjust the fiber EOM frequency until it is maximized. Do this instead of changing BNC lengths to get the signal's phase matched correctly. In this case, the frequency was 81.5 MHz.

10. Maximize the peaks again.

11. Repeat steps 8-10 until maximum peak height and error signal is obtained.

12. Turn off the frequency ramp and tune the laser far off-resonance. Lock the laser and observe how quickly the feedback voltage changes. Adjust the vertical offset of the PDH lock to slow the rate of this change. This will produce the strongest lock, as any small bumps will not immediately force the laser far off-resonance and there will be time to allow the lock to quickly recapture.

After the ULE cavity is aligned, it is desirable to minimize its coefficient of thermal expansion. One interesting property of ULE material is that its coefficient of thermal expansion can be engineered to cross from positive to negative near room temperature. By keeping the cavity at the correct temperature, the coefficient can be minimized. For this cavity, the temperature was 28.77 C.

To find this temperature, we used a 918.8970 nm (326.2525 THz) laser referenced to a frequency comb so that its frequency was stable to 1-2 MHz. This laser was coupled into the fiber EOM for modulation. The following procedure was used.

1. Change the modulation frequency until the sidebands are resonant with the cavity. Record this frequency. It may be useful to sweep the RF frequency and reduce the span of the sweep to ”zoom in” on the signal.

2. Change the temperature of the vacuum can by 0.5 C. Wait at least 7-8 hours to allow for thermalization of the cavity.

3. Repeat step 1 at the new temperature.

4. Repeat step 3 at several temperatures. Eventually the resonant RF frequency should ”turn over” and begin to track back towards to the first data point. This indicates that the coefficient of thermal expansion has changed sign. Fit the data to a parabola and set the cavity’s temperature permanently at the zero slope point of the fit.

Appendix B: Rydberg States of Holmium

B.1 Measurement of Absolute Energy Levels of Rydberg States

n	Energy (cm^{-1})	ΔE (GHz)	Level Energies (cm^{-1})				
40	48486.532	-0.63	48486.503	48486.720	48486.781		
41	48490.634	-0.64	48490.700	48490.861			
42	48494.441	-0.19	48494.428	48494.525	48494.556	48494.583	
43	48497.936	-0.68	48498.149				
44	48501.200	-0.57					
45	48504.231	-0.55					
46	48507.054	-0.52	48507.126				
47	48509.687	-0.55					
48	48512.145	-0.61	48512.215	48512.295	48512.344		
49	48514.466	-0.03	48514.563				
50	48516.620	-0.13	48516.711	48516.740	48516.782		
51	48518.643	-0.17	48518.752	48518.789			
52	48520.560	0.28	48520.641	48520.642	48520.668	48520.702	
53	48522.351	0.32	48522.398	48522.427	48522.445	48522.452	48522.461
54	48524.019	-0.22	48524.079	48524.107			
55	48525.622	0.17	48525.705	48525.732			
56			48527.144	48527.169	48527.191	48527.216	
57	48528.526	-0.29	48528.563	48528.606			
58	48529.884	0.18	48529.871	48529.906	48529.920	48529.930	48529.949
59	48531.145	-0.10					
60	48532.348	-0.19					
61	48533.495	-0.07					
62	48534.581	-0.06					
63	48535.613	-0.07					
64	48536.598	-0.00	48536.624	48536.643	48536.654	48536.669	
65	48537.537	0.13	48537.562	48537.592	48537.606		
66	48538.417	-0.20					

n	Energy (cm^{-1})	ΔE (GHz)	Level Energies (cm^{-1})				
67	48539.270	-0.10	48539.295	48539.321	48539.335		
68	48540.085	0.02	48540.107	48540.127	48540.139		
69	48540.860	0.03					
70	48541.601	0.04					
71	48542.310	0.10	48542.319	48542.339	48542.368		
72	48542.987	0.07	48543.005	48543.026	48543.036		
73	48543.634	0.02	48543.651				
74	48544.259	0.13	48544.297				
75	48544.854	0.11	48544.890	48544.899			
76	48545.427	0.16	48545.444	48545.461	48545.469		
77	48545.972	0.06	48545.988	48546.007	48546.015		
84	48549.261	0.00					
94	48552.714	0.05					

Table B.2: Measured states for the $4f^{11}6snd$ series, accurate to 0.007 cm^{-1}. The first column represents the dominant series used for determination of the quantum defect and IP for the series. The residuals relative to the Rydberg-Ritz formula are labeled ΔE, with $\delta_0 = 2.813(3)$. The remaining levels are weaker fine structure states which could not be unambiguously assigned to a common series.

n	Energy (cm^{-1})	δ	ΔE (GHz)	n	Energy (cm^{-1})	δ	ΔE (GHz)
41	48484.198	4.353	-0.04	59	48529.210	4.315	-0.12
42	48488.466	4.355	-0.28	60	48530.516	4.317	-0.02
43	48492.429	4.357	0.21	61	48531.756	4.319	0.12
*43	48492.537	4.357	3.46	62	48532.929	4.320	0.13
44	48496.074	4.360	0.08	63	48534.045	4.322	0.19
45	48499.442	4.364	-0.36	64	48535.100	4.323	0.11
46	48502.578	4.370	-0.39	65	48536.104	4.324	0.04
*47	48505.407	4.377	-2.90	66	48537.066	4.324	0.17
47	48505.490	4.378	-0.39	67	48537.981	4.325	0.24
48	48508.150	4.391	-1.68	68	48538.837	4.326	-0.18
49	48510.713	4.417	0.37	69	48539.671	4.326	-0.06
50	48512.925	4.476	-1.00	70	48540.465	4.327	-0.02
51	48514.823	4.677	1.62	71	48541.222	4.327	-0.04
51	48516.151	4.011	-1.75	72	48541.951	4.327	0.13
51	48516.181	4.017	-0.48	73	48542.646	4.328	0.20
51	48516.207	4.022	0.63	74	48543.305	4.328	0.08
52	48517.905	4.201	0.77	*74	48543.319	4.328	0.50
53	48519.736	4.257	0.46	75	48543.943	4.328	0.15
54	48521.543	4.282	0.82	76	48544.551	4.329	0.15
55	48523.194	4.294	-1.02	77	48545.118	4.329	-0.37
55	48523.250	4.295	0.68	78	48545.694	4.329	0.13
56	48524.853	4.302	0.10	86	48549.460	4.331	0.10
57	48526.379	4.308	-0.20	96	48552.850	4.331	0.01
58	48527.843	4.312	0.15	101	48554.161	4.332	-0.14

Table B.1 Measured energies for the $4f^{11}6sns$ series, accurate to 0.007 cm^{-1} with best-fit quantum defect δ determined from Eq. (4.3) using $\delta_0 = 4.341(2)$, $\Gamma = 6.9(3)$ GHz and $E_j = 48515.47(4)$ cm^{-1}. The residuals relative to the Rydberg-Ritz formula are labeled ΔE. Multiple $n = 51$ states appear due to the series perturbation, as well as a number of additional weak doublets indicated by an asterisk (*).

Appendix C: Calibration of Rydberg Energy Levels

To provide accurate energy levels of the measured Rydberg states we use an independent measurement to determine the absolute frequency of the MOT laser, which is stabilized to the TEM00 mode of a high-finesse ULE cavity providing a stable long-term frequency reference. Figure C.1(a) shows the relevant energy levels and splittings used in the experiment, while the laser setup is shown in Fig. C.1(b). The center-of-mass frequency for the $4f^{11}6s^{21}S_0$, J = 15/2 to $4f^{11}6s6p^1P_1$, J =17/2 transition is determined by the 1-m Fourier transform spectrometer at the National Solar Observatory using the setup detailed in Ref. [84]. High-resolution spectra from a Ho-Ar hollow cathode lamp are recorded, using lines in the well-known Ar II series [126, 127] for calibration to give a transition frequency of $E_{6s^2\rightarrow 6s6p} = 24360.790(1)$ cm^{-1}, which is 0.02 cm$^{-}1$ less than the value in the NIST tables [93]. For the cooling transition from F = 11 to F′ = 12, the hyperfine splittings of the ground and excited states are calculated from measurements of the hyperfine constants, giving $\Delta^{6s^2}_{F=11} = 20.589319(1)$ GHz [85, 86] and $\Delta^{6s6p}_{F'=12} = 19.33(1)$ GHz [29]. The frequency of the MOT transition can then be calculated from

$$\nu_{MOT} = E_{6s^2\rightarrow 6s6p} + \Delta^{6s6p}_{F'=12} - \Delta^{6s^2}_{F=11} + \Delta_{MOT}, \tag{C.1}$$

where $\Delta_{MOT} = -22(2)$ MHz is the detuning from resonance determined from spectroscopy of the atomic beam, giving $\nu_{MOT} = 730.31682(3)$ THz. Accounting for the double-pass acousto-optic modulator at 50 MHz and frequency doubling of the second-harmonic generation, the frequency of the master Ti:Sa laser locked to the cavity is given by $\nu_{ref} = 365.15836(2)$THz. For each measurement, the wavelength of this laser (ν_1) is recorded on a wavemeter to determine the wavemeter offset $\delta\nu = \nu_{ref} - \nu_1$. The Rydberg energy levels are then calculated from measuring the Rydberg master laser frequency (ν_2) before the doubling cavity on the same wavemeter, resulting in $\nu_{Ryd} = 2(\nu_2 + \delta\nu)$, with the absolute energy above the ground state given by

$$E_{Ryd} = \Delta^{6s^2}_{F=11} + \nu_{MOT} + \nu_{Ryd}, \tag{C.2}$$

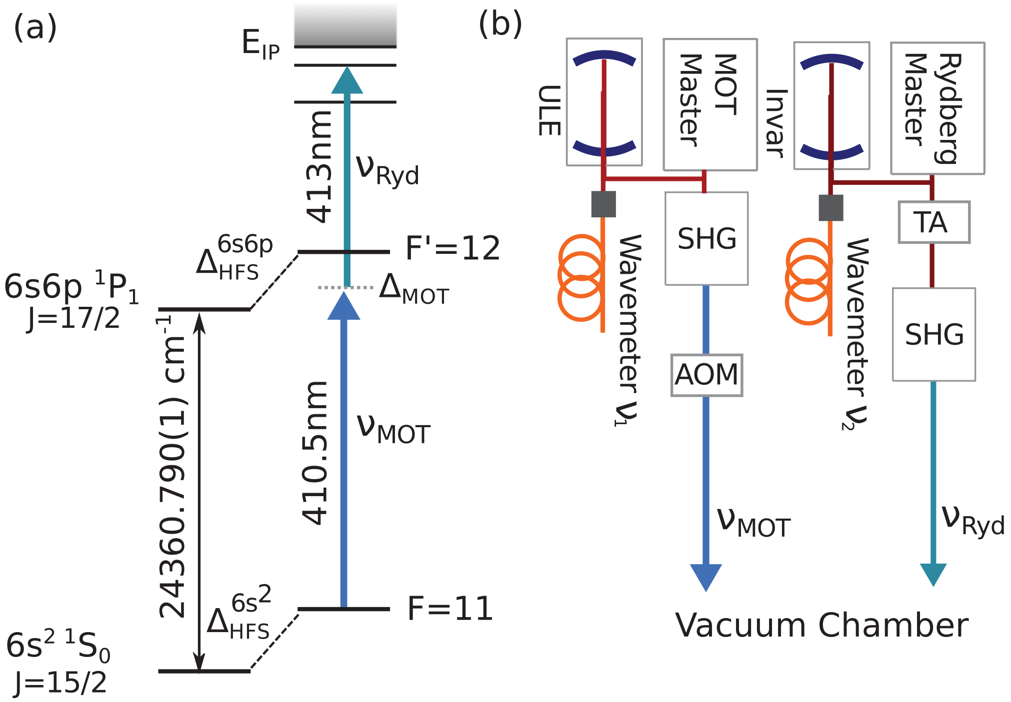

Figure C.1 Holmium energy levels. (a) MOT and Rydberg laser transitions with respect to the ground-state energy level and hyperfine splitting. (b) Laser setup showing cavity locks, wavelength measurement, and additional frequency shift from acousto-optic modulators (AOMs) on the cooling laser. A wavemeter is used to measure the laser frequencies $\nu_{1,2}$ before they are doubled and sent to the atoms.

resulting in a total uncertainty of 200 MHz on the final energy reading.

Appendix D: Ground State Transitions of Holmium

D.1 Ground State Transitions

In this section we list all of the ground state transitions used in our calculation of α in chapter 5. All of this information is gathered from reference [1].

Excited State	λ	J'	$\log g_f$ (GHz)	$2\pi\gamma$ ($10^6 \frac{1}{\mathrm{s}}$)
??	391	6.5	-1.77	0.529
$4f^{10}5d6s^2$	396	7.5	-0.63	6.23
$4f^{10}(^5\mathrm{I})5d^2(^3\mathrm{F})(^7\mathrm{G})6s$	404	6.5	-1.39	1.19
$4f^{10}5d6s^2$	404	6.5	0.19	45.2
$4f^{11}(^4\mathrm{I}^{\mathrm{o}}_{15/2})6s6p(^1\mathrm{P}^{\mathrm{o}}_1)$	405	7.5	0.9	202.
$4f^{10}(^5\mathrm{I})5d^2(^3\mathrm{F})(^7\mathrm{H})6s$	410	7.5	-0.63	5.81
$4f^{11}(^4\mathrm{I}^{\mathrm{o}}_{15/2})6s6p(^1\mathrm{P}^{\mathrm{o}}_1)$	410	8.5	0.97	206.
$4f^{10}(^5\mathrm{I})5d^2(^3\mathrm{P})(^7\mathrm{H})6s$	412	8.5	-0.19	14.1
$4f^{11}(4\,\mathrm{I}^{\mathrm{o}}_{15/2})6s6p(^1\mathrm{P}^{\mathrm{o}}_1)$	416	6.5	0.59	107.
$4f^{11}(^4I^o_{13/2})6s6p(^3P^o_2)$	417	6.5	0.06	31.5
$4f^{11}(^4I^o_{13/2})6s6p(^3P^o_2)$	419	7.5	-0.79	3.85
$4f^{11}(^4I^o_{13/2})6s6p(^3P^o_2)$	424	8.5	-0.31	10.1
$4f^{10}(^5\mathrm{I}_5)5d_{5/2}6s^2$	425	7.5	-0.79	3.74
$4f^{10}(^5\mathrm{I}_5)5d_{5/2}6s^2$	435	6.5	-0.43	9.35
$4f^{10}(^5\mathrm{I})5d^2(^3\mathrm{F})(^7\mathrm{F})6s$	493	6.5	-1.76	0.341
$4f^{10}(^5\mathrm{I}_6)5d_{5/2}6s^2$	494	6.5	-0.96	2.14
$4f^{10}(^5\mathrm{I}_6)5d_{5/2}6s^2$	498	7.5	-1.18	1.11
$4f^{11}(^4\mathrm{I}^{\mathrm{o}}_{15/2})6s6p(^3\mathrm{P}^{\mathrm{o}}_2)$	530	6.5	-1.8	0.269
$4f^{10}(^5\mathrm{I}_6)5d_{3/2}6s^2$	533	7.5	-1.83	0.217
$4f^{11}(^4\mathrm{I}^{\mathrm{o}}_{15/2})6s6p(^3\mathrm{P}^{\mathrm{o}}_2)$	536	7.5	-1.69	0.296
$4f^{11}(^4\mathrm{I}^{\mathrm{o}}_{15/2})6s6p(^3\mathrm{P}^{\mathrm{o}}_1)$	586	6.5	-1.33	0.649
$4f^{11}(^4\mathrm{I}^{\mathrm{o}}_{15/2})6s6p(^3\mathrm{P}^{\mathrm{o}}_1)$	592	7.5	-1.52	0.359
$4f^{11}(^4\mathrm{I}^{\mathrm{o}}_{15/2})6s6p(^3\mathrm{P}^{\mathrm{o}}_1)$	598	8.5	-1.05	0.924

Table D.1 The known ground state transitions of holmium. These states were used in our calculation of the polarizability.